

# Predicting Eddy Detachment from Thin Jets

by

Elise Ann Ralph

B.A., University of Chicago (1988)

Submitted in partial fulfillment of the  
requirements for the degree of degree of

Master of Science

at the

MASSACHUSETTS INSTITUTE OF TECHNOLOGY

and the

WOODS HOLE OCEANOGRAPHIC INSTITUTION

August 1991

©Elise Ann Ralph, 1991.

The author hereby grants to MIT and to WHOI permission to  
reproduce and to distribute copies of this thesis document in whole  
or in part.

Author .....

Joint Program in Physical Oceanography  
Massachusetts Institute of Technology  
Woods Hole Oceanographic Institution

August 6, 1991

Certified by .....

Lawrence J. Pratt  
Associate Scientist  
Thesis Supervisor

Accepted by .....

Lawrence J. Pratt

Chairman, Joint Committee for Physical Oceanography

MASSACHUSETTS INSTITUTE  
OF TECHNOLOGY

OCT 15 1991

LIBRARIES

# Report Documentation Page

*Form Approved  
OMB No. 0704-0188*

Public reporting burden for the collection of information is estimated to average 1 hour per response, including the time for reviewing instructions, searching existing data sources, gathering and maintaining the data needed, and completing and reviewing the collection of information. Send comments regarding this burden estimate or any other aspect of this collection of information, including suggestions for reducing this burden, to Washington Headquarters Services, Directorate for Information Operations and Reports, 1215 Jefferson Davis Highway, Suite 1204, Arlington VA 22202-4302. Respondents should be aware that notwithstanding any other provision of law, no person shall be subject to a penalty for failing to comply with a collection of information if it does not display a currently valid OMB control number.

1. REPORT DATE <b>AUG 1991</b>	2. REPORT TYPE	3. DATES COVERED <b>00-00-1991 to 00-00-1991</b>			
4. TITLE AND SUBTITLE <b>Predicting Eddy Detachment from Thin Jets</b>		5a. CONTRACT NUMBER			
		5b. GRANT NUMBER			
		5c. PROGRAM ELEMENT NUMBER			
6. AUTHOR(S)		5d. PROJECT NUMBER			
		5e. TASK NUMBER			
		5f. WORK UNIT NUMBER			
7. PERFORMING ORGANIZATION NAME(S) AND ADDRESS(ES) <b>Massachusetts Institute of Technology, 77 Massachusetts Avenue, Cambridge, MA, 02139-4307</b>		8. PERFORMING ORGANIZATION REPORT NUMBER			
9. SPONSORING/MONITORING AGENCY NAME(S) AND ADDRESS(ES)		10. SPONSOR/MONITOR'S ACRONYM(S)			
		11. SPONSOR/MONITOR'S REPORT NUMBER(S)			
12. DISTRIBUTION/AVAILABILITY STATEMENT <b>Approved for public release; distribution unlimited</b>					
13. SUPPLEMENTARY NOTES					
14. ABSTRACT <b>Using a semi-geostrophic, reduced gravity thin jet model, we analytically study the evolution of initial meanders into pinched-off rings. The model used is similar to the path equation developed by Flierl and Robinson (1984) for vertically coherent meanders. However, in the present model, the meanders are baroclinic, and a stretching term arises due to the motion of the interface. It can be shown that the equation governing the time-dependent meander of this jet (Pratt, 1988) can be transformed into the Modified Korteweg- de Vries (MKdV) equation in intrinsic coordinates. The MKdV equation admits two types of solitary wave solutions, loop solitons and breathers. The breathers are permanent meanders which propagate on the path, and some are able to form rings. Using the inverse scattering transform, we can predict breather and ring formation for simple initial meanders. The inverse scattering transform is applied to S and Q shaped meanders with piecewise constant and continuous curvature. S shaped meanders, or steps, must be multi-valued to form breathers, and must have very steep angles in order to form rings. Due to integral constraints, Q shaped meanders, or lobes, are unable to pinch together to form rings unless they are wide enough so that the two side flanks of the lobe act as two independent steps. The numerical solutions indicate that the breathers predicted by the inverse scattering is a very good approximation to the full solution.</b>					
15. SUBJECT TERMS					
16. SECURITY CLASSIFICATION OF:			17. LIMITATION OF ABSTRACT <b>Same as Report (SAR)</b>	18. NUMBER OF PAGES <b>105</b>	19a. NAME OF RESPONSIBLE PERSON
a. REPORT <b>unclassified</b>	b. ABSTRACT <b>unclassified</b>	c. THIS PAGE <b>unclassified</b>			



# Predicting Eddy Detachment from Thin Jets

by

Elise Ann Ralph

Submitted to the Joint Program in Physical Oceanography  
Massachusetts Institute of Technology  
Woods Hole Oceanographic Institution  
on August 6, 1991, in partial fulfillment of the  
requirements for the degree of  
Master of Science

## Abstract

Using a semi-geostrophic, reduced gravity thin jet model, we analytically study the evolution of initial meanders into pinched-off rings. The model used is similar to the path equation developed by Flierl and Robinson (1984) for vertically coherent meanders. However, in the present model, the meanders are baroclinic, and a stretching term arises due to the motion of the interface.

It can be shown that the equation governing the time-dependent meander of this jet (Pratt, 1988) can be transformed into the Modified Korteweg- deVries (MKdV) equation in intrinsic coordinates. The MKdV equation admits two types of solitary wave solutions, loop solitons and breathers. The breathers are permanent meanders which propagate on the path, and some are able to form rings.

Using the inverse scattering transform, we can predict breather and ring formation for simple initial meanders. The inverse scattering transform is applied to S and  $\Omega$  shaped meanders with piecewise constant and continuous curvature. S shaped meanders, or steps, must be multi-valued to form breathers, and must have very steep angles in order to form rings. Due to integral constraints,  $\Omega$  shaped meanders, or lobes, are unable to pinch together to form rings unless they are wide enough so that the two side flanks of the lobe act as two independent steps. The numerical solutions indicate that the breathers predicted by the inverse scattering is a very good approximation to the full solution.

Thesis Supervisor: Lawrence J. Pratt  
Title: Associate Scientist

## Acknowledgments

I would like to thank my advisor, Larry Pratt, for his encouragement and support while I worked on this project. I would also like to thank the other members of my committee: Glenn Flierl, Nelson Hogg, Joe Pedlosky and Paola Rizzoli for their helpful advice and enthusiasm. In particular, Paola Rizzoli always encouraged me with her excitement, and many ideas.

I have been fortunate to have made many close friends since entering the Joint Program. I would like to thank all of them for their help and friendship, especially in this past year. I appreciate all of the G&G students of room 145, who didn't seem to mind that I was always there using the Athena terminal. I miss LuAnne Thomspson as an office-mate and friend a great deal; she was very positive when I needed her support, and always willing to hear about my work, even during the hectic last months of her thesis. Special thanks go to Cecilie Mauritzen for her warmth, encouragement and hospitality. She has patiently listened to me many times while I tried to work through some idea or another. I am deeply indebted to Chris Bradley for his constant cheerfulness and optimism. His friendship and moral support has helped me a great deal. Finally, I would like to thank my parents: my father for his sense of joy and endless enthusiasm and my mother for her quiet understanding of what is important.

This work has been supported by NSF contract number OCE 89-16446 and ONR contract number N00014-89-J-1182.



# Contents

<b>1</b>	<b>Introduction</b>	<b>7</b>
1.1	Previous Work on Thin Jets . . . . .	9
1.2	Relation Between The Path Equation and The RLF Model . . . . .	11
1.3	Model Parameters . . . . .	17
<b>2</b>	<b>Step Meanders</b>	<b>23</b>
2.1	Introduction . . . . .	23
2.2	Inverse Scattering Transform . . . . .	24
2.3	Piecewise Constant Curvature . . . . .	28
2.4	Smooth Steps . . . . .	35
2.4.1	Full Numerical Solutions . . . . .	37
2.5	Conclusions . . . . .	39
<b>3</b>	<b>Lobes</b>	<b>59</b>
3.1	Introduction . . . . .	59
3.2	Integral Constraints on the Infinite Domain . . . . .	59
3.3	Thin Lobes . . . . .	61
3.4	Wide Lobes . . . . .	66
3.5	Modifications of Single Lobes . . . . .	69
3.6	Conclusions . . . . .	70
<b>4</b>	<b>Conclusions</b>	<b>89</b>
<b>A</b>	<b>The Inverse Scattering Transform</b>	<b>95</b>

A.1	The Scattering Problem . . . . .	95
A.2	Spectral Evolution . . . . .	97
A.3	Inverse Scattering . . . . .	99
A.4	Summary . . . . .	100

# Chapter 1

## Introduction

One of the most prominent features of the Gulf Stream east of Cape Hatteras is its meandering; the stream fluctuates north and south as a coherent structure in a wavelike pattern. Meanders are also present in other strong currents such as the Kuroshio and the Agulhas. Large meanders may pinch off and form rings, transporting heat and momentum across the stream in the process.

The variability in the location of the Gulf Stream has long been known. Hydrographic work in the 1930's (Iselin, 1936; Church 1937) was able to demonstrate that the position of the Gulf Stream changes rapidly. In the early 1950's, Fuglister and Worthington (1951) were able to show that the Stream moves in a wavelike pattern. More recently, Hansen (1970) found that the meanders have a propagation speed of 5 to 20  $cm\ s^{-1}$ , and slowly grow as they propagate downstream.

Since the advent of remote sensing techniques, the meandering pattern is clearly visible in infrared satellite images, and data from other remote sensing instruments. With a time sequence of IES images, the propagation, and pinch off, of these meanders can be observed. Vasquez and Watts (1985) and Tracey and Watts (1986) calculated dispersion relations for long wavelength meanders, finding a propagation speed of  $c_{ph} = 11\ km\ day^{-1}$  for a wavelength of 630  $km$ . Kontoyiannis and Watts (1990) were able to calculate dispersion relations for the meanders. They found that short meanders propagate faster than long meanders, with phase speeds rang-

ing from  $c_{ph} = 6 \text{ km day}^{-1}$  for a wavelength of  $700 \text{ km}$ , to  $c_{ph} = 50 \text{ km day}^{-1}$  for a  $150 \text{ km}$  meander. Their dispersion relation indicates that the long wave meanders are slowly propagating with a time scale proportional to the third power of the wavelength. While these meanders are waves on a current, they do not seem to change the basic velocity profile. East of Cape Hatteras, the Gulf Stream is highly variable, with eddy kinetic energies of  $1500 \text{ cm}^2 \text{ s}^{-2}$  at  $73^\circ \text{W}$  (Halkin and Rossby 1985). However, Halkin and Rossby also showed that two-thirds of this eddy kinetic energy is due to meandering, and not the mesoscale eddy field. In fact, in a streamwise reference frame, the eddy kinetic energy due to changes in the structure of the front is only three times as large as mid-ocean values found by Richardson (1983). They conclude that the Gulf Stream is a well-defined structure, even though its position may widely vary.

By assuming that the Gulf Stream moves coherently as a “frozen jet,” the meandering can be modeled as the motion of the jet axis due to potential vorticity constraints. When the deformation radius and the width of the Gulf Stream are small compared to the length scale of the meanders, the Stream is approximated as a thin jet. In thin jet models it is possible to solve for the cross-stream structure of the flow at the outset, a simplification which often allows consideration and tractability of strongly non-linear processes.

This thesis uses the thin jet approach to model the meander evolution of a reduced gravity jet. The rest of this chapter contains a discussion of previous thin jet models, and their relation to the model used here. In the rest of the thesis, the evolution of various isolated meanders will be studied using numerical solutions, and the inverse scattering transform, with the object of finding criteria for ring-formation based on the shape of the initial condition. The inverse scattering transform is outlined in Chapter 2, and applied to several simple initial conditions in Chapters 2 and 3.

## 1.1 Previous Work on Thin Jets

The thin-jet approach was suggested by Warren (1963) who modeled steady state meanders as a balance among planetary vorticity, the curvature of the stream, and topographic effects. Robinson and Niiler (1967) found a similar vorticity balance, and expressed it in streamwise coordinates. However, Robinson (1967) found that these models, and the first time-dependent models based on them, could not fit the meander and mean-path data. He concluded that stretching can not be left out of a time-dependent thin jet model.

A later model including time-dependent meandering was the Robinson, Luyten and Flierl model (1975). The motion of the axis of a quasi-geostrophic, stratified jet is governed by a vorticity balance due to the curvature of the axis, the beta effect, interactions between the downstream flow and the meander field, and stretching. The path equation is obtained by integrating the vorticity equation across the jet horizontally, and in the vertical. This model contains a mechanism that allows the jet to form a closed loop, analogous to ring-formation in the Gulf Stream.

Flierl and Robinson (1984) later corrected inconsistencies in the non-dimensional parameters, so that cross-stream widths are much smaller than along stream scales, making the cross-stream momentum equation ageostrophic. The cross-stream integration of the vorticity equation forces the meanders to be matched with the barotropic eddies on either side of the jet. They were also able to show that the dispersion relation for small-amplitude meanders was identical to the dispersion relation found for long wave perturbations to a quasi-geostrophic jet using standard instability theory.

Using contour dynamics, Pratt and Stern (1986), modeled the evolution of a single front of potential vorticity in a quasi-geostrophic,  $1\frac{1}{2}$  layer model. They found that short waves are advected eastward by the mean flow, while longer waves are slowed by vortex induction effects. Using contour dynamics, they modeled initial meanders shaped like steps, and lobes. All steps dispersed, while tall, thin lobes were able to form rings. Ring-formation was enhanced by the presence of short

waves to the west, or the presence of a second lobe of the opposite sign.

This paper also included a long wave approximation to the contour dynamics equations of motion, which was explored in Pratt (1988). The meander wavelengths are assumed to be long compared to a deformation radius so that

$$\begin{aligned} L(x, t) &= \epsilon^{-1}n(X, t) \\ X &= \epsilon x \end{aligned}$$

They found that by making a long wave assumption the meandering motion of the front could be determined by a local equation. The time scale, which was determined by the dynamics, is proportional to the cube of the wavelength. In this limit the velocity  $\frac{\partial n}{\partial t}$  of the front normal to itself is proportional to the rate of change of frontal curvature  $\kappa$  with respect to distance  $s$  along the front.

$$\frac{\partial n}{\partial t} = -\frac{1}{2} \frac{\partial \kappa}{\partial s} \tag{1.1}$$

Although equation 1.1 appears very simple, its solutions contain a rich variety of physical behavior. Numerical solutions to isolated initial meanders show that initial conditions with large amplitudes or wavenumbers form slow, coherent meanders that fluctuate from the north to the south. After several fluctuations, these meanders begin to pinch together, forming a closed loop. Pratt found that the amplitude of these meanders grew with time after they became multi-valued, implying a form of finite amplitude instability.

More recently, Cushman-Roisin et al. (1991), hereafter referred to as CPR, have generalized Equation 1.1, forming a semi-geostrophic, reduced gravity path equation on the beta plane, governing the motion of the axis of a thin jet. In this model, the advection of planetary vorticity is the same size as the advection of the curvature term. The path equation is then

$$\frac{\partial n}{\partial t} = a \frac{\partial \kappa}{\partial s} + b \sin \Theta \tag{1.2}$$

The meandering motion of the jet,  $\frac{\partial n}{\partial t}$  is governed by vortex induction ( $a \frac{\partial \kappa}{\partial s}$ ), and the advection of planetary vorticity. ( $b \sin \Theta$ ), where  $\Theta$  is the angle the jet makes with East (Figure 1.1). The relative sizes of these two effects are determined by  $a$  and  $b$ , which depend on the velocity structure of the jet.

$$\begin{aligned} a &= \frac{1}{h_{-\infty} - h_{\infty}} \int_{-\infty}^{\infty} h h_n^2 dn, \\ b &= \frac{h_{-\infty} + h_{\infty}}{2} \end{aligned} \tag{1.3}$$

$h$  is the interface depth, where  $h_{\infty}$  and  $h_{-\infty}$  are the depths of the interface on either side of the jet.

Since the model is semi-geostrophic,  $-h_n$  is just the pathwise velocity of the jet itself, so the parameters  $a$  and  $b$  are related to moments of the velocity profile.

This equation is the thin jet model used in this thesis, and the next section shows how this equation arises from the Robinson, Luyten and Flierl model (1975), if  $1\frac{1}{2}$  layer stratification is assumed. Section 1.3 presents estimates of the parameters  $a$  and  $b$ , based on the shape of isopycnals at  $68^\circ W$ .

## 1.2 Relation Between The Path Equation and The RLF Model

In this section we show that the path equation 1.2 is a  $1\frac{1}{2}$  layer version of the Robinson, Luyten and Flierl (1974) (hereafter referred to as RLF) path equation for full stratification. Following Robinson, Luyten and Flierl (1974), and Flierl and Robinson (1984) (FR), we rederive their vorticity equation in the intrinsic coordinate system defined in Figure 1.1. This vorticity in the upper layer is then integrated in the vertical and across the stream to get the path equation. The model is a rotating, inviscid, Boussinesq, hydrostatic fluid on the beta plane. For generality, we will assume full stratification as long as possible.

As in RLF, the structure of the jet is assumed known, and the jet velocity and axis velocity are assumed to be horizontally non-divergent. For full stratification, the

meandering is assumed independent of depth, so the whole jet meanders coherently.

The coordinate system is the right-handed intrinsic coordinate system shown in Figure 1. Distances are measured along the axis of the jet with  $s$ . The coordinate  $n$  is defined by constructing a positive normal at every point along the jet. The transformation to this coordinate system associates every point  $(x, y)$  near the jet, with the coordinates  $(s, n)$

$$\begin{aligned} x &= X - n \frac{\partial Y}{\partial s} \\ y &= Y + n \frac{\partial X}{\partial s} \end{aligned} \tag{1.4}$$

$X(s, t), Y(s, t)$  are the coordinates of the point on the axis of the jet, whose exact position is determined by the meandering motion. The axis of the jet will be chosen to be the position of the front. The Jacobian of the transformation is given by

$$\tilde{J} = \left| \frac{\partial(n, s)}{\partial(x, y)} \right| = \frac{1}{1 - n\kappa}$$

where  $\kappa = \frac{\partial\Theta}{\partial s}$  is the local curvature of the jet. The path angle  $\Theta$  is the angle the jet makes with the East.

$$\Theta = \tan^{-1}\left(\frac{\partial Y}{\partial X}\right)$$

In order for the coordinate transformation to remain valid, the scale of the cross-stream structure  $n$  must be small compared to  $\kappa^{-1}$ ; at a distance  $n = 1/\kappa$ , the coordinate transformation becomes singular. This coordinate system is slightly different from the coordinate system used by RLF because the tangential variable  $s$  is used as an independent variable instead of  $X$ . We have chosen to define  $n$  to be positive to the left of positive  $s$ , making the coordinate system  $(s, n)$  is right-handed.

The total velocities within this coordinate system are defined as  $U$ , the velocity along the jet, and  $V$  the velocity across the jet. We can find them by rotating the

eastward ( $u$ ) and northward ( $v$ ) velocities into the local coordinate system.

$$\begin{aligned} U &= u \sin\Theta - v \cos\Theta \\ V &= u \cos\Theta + v \sin\Theta \end{aligned} \tag{1.5}$$

As in RLF, the velocity field  $(U, V)$  is decomposed into the jet velocity  $(U_0, 0)$ , the axis velocities  $(A, C)$ , which are the velocities at which the reference frame meanders, and the residual velocity-field induced by the meanders,  $(U_m, V_m)$ . For simplicity we will assume that  $(X_0, Y_0)$ , the inlet point, is fixed.

In order to formulate the model we introduce the following scales:

$$\begin{aligned} s &\sim \mathcal{L} &= &\text{down-stream scale} \\ n &\sim \ell &= &\text{cross-stream scale} \\ z &\sim H &= &\text{characteristic depth of the ocean} \\ t &\sim T &= &\text{meandering time scale} \\ f &\sim f_0 &= &\text{Coriolis parameter} = f_0 \left(1 + \frac{\beta}{f_0} y\right) \\ U &\sim V_0 &= &\text{jet velocity scale} \\ C, A &\sim V_A &= &\text{axis velocity scale} \\ p &\sim f_0 \ell U_0 &= &\text{geostrophic pressure scale} \end{aligned}$$

Henceforth, all variables in the model have been non-dimensionalized by these scales. In order to characterize the equations of motion, RLF then introduced the non-dimensional parameters.

$$\begin{aligned} \epsilon &= \frac{\ell}{\mathcal{L}} &= &\text{ratio of cross-stream scales to along-stream scales} \\ \epsilon &= \frac{V_0}{f_0 \mathcal{L}} &= &\text{downstream Rossby number} \\ \tilde{\beta} &= \frac{\beta \mathcal{L}^2}{V_0} &= &\text{ratio of planetary vorticity gradient to relative vorticity gradient} \\ \tilde{a} &= \frac{V_A}{V_0} &= &\text{relative velocity of the axis} \\ N^2 &= \frac{N_{dim}^2 H^2}{f_0^2 \ell^2} &= &\text{non-dimensional Brunt-Vaisala frequency squared} \\ m &= \frac{V_m}{V_0} &= &\text{relative velocity of the meanders} \end{aligned}$$

The full non-dimensional equations of motion (from RLF 3.6 -3.8) are

$$\epsilon \left[ \frac{DU}{Dt} - V \frac{D\Theta}{Dt} \right] - fV + \frac{\ell}{\mathcal{L}} J \frac{\partial p}{\partial s} = 0 \quad (1.6)$$

$$\epsilon \left[ \frac{DV}{Dt} + U \frac{D\Theta}{Dt} \right] + fU + \frac{\partial p}{\partial n} = 0 \quad (1.7)$$

$$\frac{\partial V}{\partial n} - \frac{\ell}{\mathcal{L}} J \kappa V + \frac{\ell}{\mathcal{L}} J \frac{\partial U}{\partial s} + \epsilon \frac{\partial w}{\partial z} = 0 \quad (1.8)$$

where

$$U = U_0 + aA + mU_m + \dots \quad (1.9)$$

$$V = aC + \frac{\ell}{\mathcal{L}} mV_m + \dots \quad (1.10)$$

$$w = \epsilon w_m + \dots \quad (1.11)$$

and  $J = 1 - \frac{\ell}{\mathcal{L}} n \kappa$ . The total derivative  $\frac{D}{Dt}$  is defined by

$$\frac{D}{Dt} = a \frac{\partial}{\partial t} + J(U - aA + a \frac{\ell}{\mathcal{L}} n \Theta_t) \frac{\partial}{\partial s} + \frac{\ell}{\mathcal{L}} (V - aC) \frac{\partial}{\partial n} \quad (1.12)$$

In the intrinsic coordinate system, there is an apparent force due to the curvature of the path. This apparent force appears as the  $\frac{D\Theta}{Dt}$  terms in Equations 1.6 and 1.7.

We are interested in long-wavelength meanders of a semi-geostrophic jet. Small changes in the jet velocity field are induced by the meandering field, as  $(U_m, V_m)$ . Cross-stream variations in the isopycnals are large, so the cross-stream width of the jet is of the order of the deformation radius. This assumption was not made by RLF, but was included in the FR model. The beta effect and curvature play an equal role in the dynamics. These assumptions imply :

$$\begin{aligned} \epsilon &<< 1 \\ m &= 0(\epsilon) \\ \frac{\ell}{\mathcal{L}} &= O(\epsilon) \\ N^2 &\sim 1 \\ \tilde{\beta} &\sim 1 \end{aligned}$$

With this choice of parameters, we may carry out an expansion in  $\epsilon$ ,

$$\text{e.g. } h = h_0 + \epsilon h_1 + \mathcal{O}(\epsilon^2)$$

The cross-stream momentum equation (Equation 1.7) is geostrophic:

$$fU_0 = -\frac{\partial p}{\partial n} \quad (1.13)$$

while the along-stream momentum equation is ageostrophic. The vorticity equation (equation 4 in FR) can be derived by cross-differentiating the momentum equations, and using continuity.

$$F_0(s, t) + U_0(n, z)F_1(s, t) + U_0^2(n, z)F_2(s, t) - \frac{\partial w_m}{\partial z} = I \quad (1.14)$$

where the functionals  $F_i$  are given in Table 1.  $I$ , also given in Table 1, is an interaction term, representing the interaction of the jet with the meander field. The size of  $\tilde{a}$  (the ratio of the axis velocities to the jet velocities) is to be determined by the dynamics. For the moment we assume that  $\tilde{a} \leq 1$ .

After vertical and horizontal integrations, (over an area normal to the flow of the jet) Flierl and Robinson are left with their path equation (equation 6 of FR).

$$F_0(s, t) + F_1(s, t) \int dn \int dz U_0 + F_2(s, t) \int dn \int dz U_0^2 = \tilde{a} \frac{\partial}{\partial t} \left[ \int dz U_m \right]_{n=-\frac{d}{2}}^{n=\frac{d}{2}} \quad (1.15)$$

where  $d$  denotes the width of the jet. With the assumptions of a rigid lid, and a flat bottom the vertical integration has eliminated the stretching term. By vertically integrating the vorticity equation across the jet, the right side of Equation 1.14 (the interaction term) vanishes for all of the modes except for the barotropic mode. The horizontal integration of the interaction term imposes a matching condition on the barotropic component of the meander field.

In  $1\frac{1}{2}$  layers the area integration across the jet leads to a slightly different path equation. We expect that the baroclinic meanders will travel much slower than the

barotropic meanders, and so in the  $1\frac{1}{2}$  layer model  $\tilde{a} = O(\epsilon)$ . This greatly simplifies Equation 1.15:

$$U_0 Y_s + U_0^2 \kappa_s - \frac{\partial w}{\partial z} = \frac{\partial}{\partial n} \left[ \frac{D'_1}{Dt} U_0 + \frac{D'_0}{Dt} U_m \right] \quad (1.16)$$

where

$$\frac{D_0}{Dt} = U_0 \frac{\partial}{\partial s} \text{ is the advection due to the jet}$$

and

$$\frac{D'_1}{Dt} = U_m \frac{\partial}{\partial s} + V_m \frac{\partial}{\partial n} \text{ is the advection due to the residual fields}$$

In  $1\frac{1}{2}$  layers, the vertical integration is carried out over the active upper layer, from the surface to the interface between the two layers. At this interface, the vertical velocity does not vanish :

$$w_{interface} = U_0 \frac{\partial h_1}{\partial s} + (V_m) \frac{\partial h_0}{\partial n} \quad (1.17)$$

The vertically integrated vorticity equation becomes

$$\left( \int U_0 dz \right) Y_s + \left( \int U_0^2 dz \right) \kappa_s - [U_0 h_{1s} + V_m h_{0n}] = h_0 \frac{\partial}{\partial n} \left[ \frac{D'_1}{Dt} U_0 + \frac{D'_0}{Dt} U_1 \right] \quad (1.18)$$

Using cross-stream geostrophy (Equation 1.13) and the ageostrophic along-stream momentum equation (from Equation 1.6, with  $\tilde{a} = O(\epsilon)$ ):

$$\frac{D'_1}{Dt} U_0 + \frac{D'_0}{Dt} U_m = -\frac{\partial h_1}{\partial s} + (V_m + C_1) \quad (1.19)$$

leads to

$$Y_s \int U_0 dz + \kappa_s \int U_0^2 dz + C_1 h_{0n} = \frac{\partial}{\partial n} \left[ h_0 \left( \frac{D'_1}{Dt} U_0 + \frac{D'_0}{Dt} U_m \right) \right] \quad (1.20)$$

We then integrate this equation across the jet from  $n = -\infty$  to  $n = +\infty$  (i.e. to where the jet has decayed away, so  $h_{0n} \rightarrow 0$ , or to where the lower layer outcrops,

so  $h_0 = 0$ ). The right side vanishes, leaving

$$Y_s \int \int U_0 dz dn + \kappa_s \int \int U_0^2 dz dn - C_1 \int U_0 dn = 0 \quad (1.21)$$

Because  $U = -\frac{\partial h}{\partial n}$ , this is the path equation 1.2 (recalling the definition of the parameters  $a$  and  $b$  from Equation 1.3, and that  $C$  is the velocity of the meandering motion as the jet moves normal to itself, i.e.  $\frac{\partial n}{\partial t}$ ). The absence of a barotropic mode allows the jet to meander in isolation. Because the baroclinic deformation radius is much smaller than the barotropic radius, the path is not affected by the far field in the reduced gravity.

The  $1\frac{1}{2}$  layer path equation 1.2 can not be found from the final path equation in Flierl and Robinson (1984) for full stratification by simply modifying the coefficients of the path equation (the moments of  $U_0$ ) so that the velocity obeys a  $1\frac{1}{2}$  layer structure. Because of the absence of the barotropic mode, the vertical integration of the vorticity equation leaves a stretching term that comes from the meandering front.

### 1.3 Model Parameters

The model derivation is independent of the current structure, leaving the parameters  $a$  and  $b$  free to be specified. These parameters can be estimated by approximating the shape of the interface between the two layers by the shape of an isopycnal in a jet. Estimates of the model parameters  $a$  and  $b$  were made using a Gulf Stream density cross-section taken at  $68^\circ W$ , by Hall. Five estimates were made with the isopycnals indicated in Figure 1.2 (from Hall and Fofonoff, 1991). Two of the isopycnals,  $\sigma_\theta = 26.5$ , and  $\sigma_\theta = 26.6$  outcrop, and the surface was defined as the northern edge of the Stream. If the profile did not outcrop, the edges of the stream were chosen to be where  $\frac{\partial h}{\partial n} \rightarrow 0$ .

In order to calculate the parameters, the shape of the isopycnal must be expressed non-dimensionally. The depth of the isopycnal is scaled by  $H$ , the depth of that

isopycnal on the southern edge of the Gulf Stream. Values of  $H$  range from 550 m for the 26.5 contour, to 1330 m for the 27.7 contour.

Cross-stream distances were non-dimensionalized using the deformation radius  $R_d = \sqrt{(g'H)/f_0}$ . At  $68^\circ W$ , the Gulf Stream has a latitude of approximately  $40^\circ N$ , so the Coriolis parameter is  $f_0 = 9.4 \times 10^{-5} \text{ sec}^{-1}$ . The reduced gravity was calculated according to the formula for a two layer system  $g' = g(\frac{\rho_0 - \rho_1}{\rho_0})$ , where  $\rho_0$  is the density of the lower layer, and  $\rho_1$  is the density of the upper layer. The densities for each isopycnal were estimated by averaging the density of the water above and below the isopycnal. Because the deep ocean is much more homogeneous than the water at and above the thermocline, the density of the lower layer will be the same for all five of the isopycnals, approximately  $1028 \text{ kg/m}^3$ . The deformation radius for all five of the isopycnals was found to be approximately 40 kilometers.

Once the isopycnal profiles were non-dimensionalized,  $a$  and  $b$  were calculated using equation 1.3. For the calculation of  $a$ ,  $\frac{\partial h}{\partial n}$  was calculated by discretizing the depth, and then using center differencing to find the derivative in between the grid points. Using Simpson's Rule, the integral was then carried out across the Stream. The calculation of  $b$  is a simple average of the depth of the isopycnal at the two edges of the Stream.

Table 2 contains the values of  $a$  and  $b$  for each of the five isopycnals. The parameter  $b$  depends on whether the isopycnal outcrops or not. For outcropping isopycnals,  $b = 0.5$ . As the isopycnals get deeper,  $b$  increases to approximately 0.7. The upper two outcropping isopycnals, and the two middle isopycnals have  $a \approx 0.15$ . The 27.7 isopycnal has a much lower value of  $a$  ( $a = 0.09$ ). This isopycnal is slightly deeper than the core of the current, so its slope  $\frac{\partial h}{\partial n}$  is smaller than the other isopycnals, leading to a smaller estimate of  $a$ . Because this isopycnal misses the current core, it is not a good choice for the shape of the interface.

Table 1. Functionals from the Vorticity Equation

$$\begin{aligned}
 F_0(s, t) &= \kappa \tilde{a}^2 \frac{\partial A}{\partial t} \\
 &\quad + \tilde{a}^2 \frac{\partial}{\partial s} \frac{\partial}{\partial t} C \\
 &\quad + \tilde{a}^2 A \frac{\partial}{\partial t} \kappa \\
 &\quad + \tilde{a} \tilde{\beta} (A \sin \Theta + C \cos \Theta) \\
 F_1(s, t) &= \kappa^2 \tilde{a} C + \tilde{a} \frac{\partial}{\partial s} C \\
 &\quad + \tilde{a} A \kappa_s + \tilde{a} \frac{\partial}{\partial t} \kappa + \tilde{\beta} \sin \Theta \\
 F_2(s, t) &= \kappa_s \\
 I &= \frac{\partial}{\partial n} \left[ \frac{D'_1}{Dt} (U_0 + aA) + \frac{D'_0}{Dt} U_m + aC \frac{D'_1}{Dt} \Theta \right]
 \end{aligned}$$

where

$$\begin{aligned}
 \frac{D'_0}{Dt} &= a \frac{\partial}{\partial t} + U_0 \frac{\partial}{\partial s} \\
 \frac{D'_1}{Dt} &= U_m \frac{\partial}{\partial s} + V_m \frac{\partial}{\partial n} + \epsilon w_m \frac{\partial}{\partial z}
 \end{aligned}$$

Table 2. Estimates of a and b

$\sigma_\theta$	$R_d$	$a$	$b$
26.5	40.7	0.149	0.50
26.6	42.0	0.150	0.50
27.4	42.6	0.144	0.64
27.6	39.8	0.150	0.70
27.7	36.8	0.099	0.75

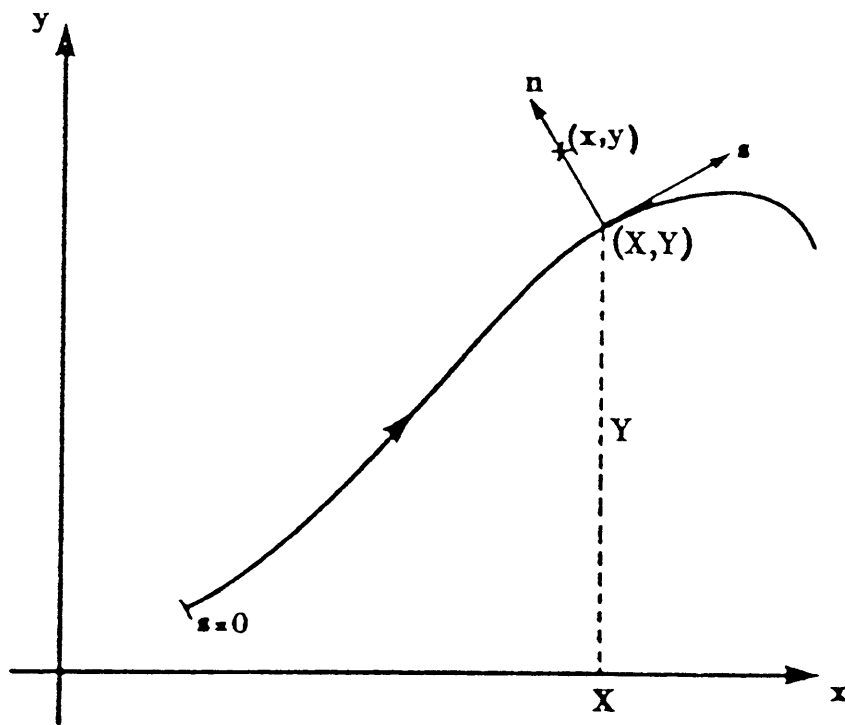


Figure 1-1: Model Geometry for the  $1\frac{1}{2}$  layer Path Equation.

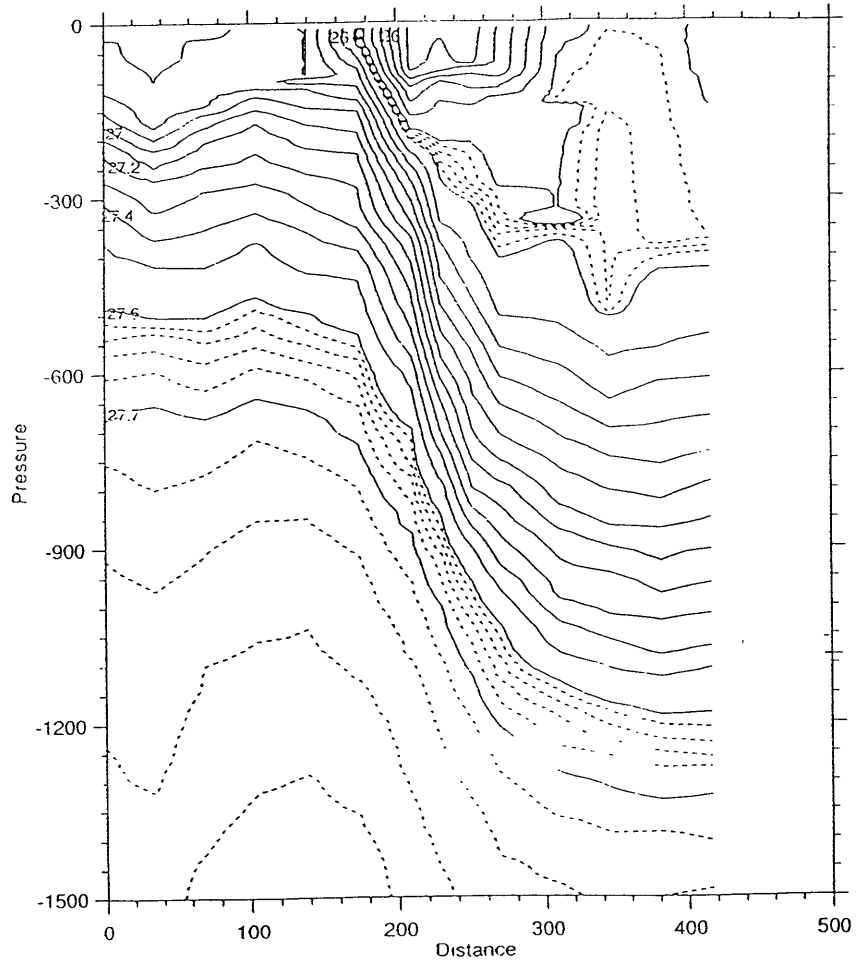


Figure 1-2:  $\sigma_\theta$  section across the Gulf Stream at  $68^\circ W$ , from Hall and Fofonoff 1991.



# Chapter 2

## Step Meanders

### 2.1 Introduction

We would like to be able to use the path equation to characterize the types of initial conditions that will form rings. Pratt (1988) approached this question by numerically integrating Equation 1.1, the f-plane path equation, for initial conditions of the form,  $\ell(x, 0) = e^{-\left(\frac{x}{w}\right)^2} \cos k_0 x$ . He found that the all the initial meanders shed a train of short waves to the east. If the initial meander was steep enough then a large amplitude, slowly-propagating, oscillatory meander emerged. After further integration, the meander eventually pinched off, (Figure 2.1 (from Pratt 1988)). This approach illustrates the changes a path goes through in forming a ring, but the range in initial parameter space explored is limited by the slow and expensive numerical integration of the path equation. More recently, CPR has shown that the path equation can be solved by the inverse scattering transform, an elegant method that identifies the large-amplitude, slowly-propagating meander, without fully integrating the path equation.

This chapter outlines this solution method and applies it to steps, or “S”-shaped paths which are the simplest types of meanders in a zonal jet. The large-amplitude meanders evolving from piecewise constant curvature steps can be identified algebraically. A class of smooth steps is also considered and criteria for ring-formation

are established based on the angle of the initial step.

## 2.2 Inverse Scattering Transform

Following CPR, we may show that equation 1.2 may be written only in terms of  $\Theta$ , the path angle. Differentiating equation 1.2 twice with respect to  $s$ , and using the relation

$$n_t = Y_t \cos \Theta - X_t \sin \Theta \quad (2.1)$$

leads to

$$(-\sin \Theta X_t + \cos \Theta Y_t = \frac{1}{\Theta_s} \left[ \frac{1}{\Theta_s} (\Theta_t - a \Theta_{sss} - b \Theta_s \cos \Theta) \right]_s \quad (2.2)$$

Adding 2.2 and 1.2 together, multiplying the result by  $\Theta_s$ , and integrating with respect to  $s$ , leads to

$$\Theta_t = \frac{1}{2} a \Theta_s^3 + a \Theta_{sss} + c \Theta_s \quad (2.3)$$

$$\text{where } c = b \cos \Theta_0 - \frac{1}{2} a \kappa_0^2$$

The subscript zero denotes the value at the fixed inlet point,  $s = 0$ . If the initial meander is isolated, so that  $\Theta \rightarrow 0$  as  $x \rightarrow \pm\infty$ , then the path equation (Equation 2.3 ) can be rewritten as

$$\Theta_t - b \Theta_s = a \Theta_s^3 + a \Theta_{sss} \quad (2.4)$$

Transferring to the coordinate frame moving with the Rossby long wave speed, so  $\tilde{s} = (s + bt)$ , and taking the derivative with respect to  $\tilde{s}$ , leads to an equation for the curvature,  $\kappa = \Theta_{\tilde{s}}$

$$\kappa_t - \frac{3a}{2} \kappa^2 \kappa_{\tilde{s}} - a \kappa_{\tilde{s}\tilde{s}\tilde{s}} = 0 \quad (2.5)$$

If we let  $u = \frac{a^{\frac{1}{2}}}{2} \kappa$ ,  $x = -a^{\frac{-1}{2}} \tilde{s}$ , and rescaling the time by  $a^{\frac{1}{2}}$ , then we obtain

$$u_t + 6u^2 u_x + u_{xxx} = 0 \quad (2.6)$$

This is the Modified Korteweg-deVries (MKdV) equation, one of a class of nonlinear evolution equations that may be solved using the inverse scattering transform (Ablowitz et al. 1974). This solution method, which can be thought of as a nonlinear extension of the Fourier transform method, allows us to easily find the large-amplitude meander that evolves from an initial condition. Appendix A gives a detailed discussion of the inverse scattering transform; a brief description is given here.

The initial condition is mapped into a spectral space by associating the initial condition with a linear eigenvalue problem. For the MKdV equation, the eigenvalue problem is

$$\psi_{xx} + [\xi^2 + (u^2(x, 0) + iu_x(x, 0))]\psi = 0 \tag{2.7}$$

$$\begin{aligned} \psi(x) &\sim e^{-i\xi x}, & x \rightarrow -\infty \\ \psi(x) &\sim B(\xi)e^{i\xi x} + A(\xi)e^{-i\xi x}, & x \rightarrow +\infty \end{aligned}$$

This is the time-independent Schrodinger equation with  $u^2 + i u_x$  acting as a potential, for the eigenfunction  $\psi$ , and eigenvalue  $\xi$ . An incident wave, with wavenumber  $\xi$ , and amplitude  $A(\xi)$  reaches the potential from  $+\infty$ . A wave of unit amplitude is transmitted, and one of amplitude  $B(\xi)$  is reflected. The eigenvalues of Equation 2.8 lie in a continuous spectrum along the real axis. There may be a finite number of discrete eigenvalues which lie in the upper complex plane, either on the imaginary axis,  $\xi = i\eta$ , or in pairs located symmetrically about the imaginary axis,  $\xi = \pm\alpha(1 + i\lambda)$ . These discrete eigenvalues may be thought of as bound states to the scattering problem, and occur at the poles of the transmission coefficient, the zeros of  $A(\xi)$ .

As  $u(x, t)$  evolves according to the MKdV equation, then the amplitudes  $A(\xi)$  and  $B(\xi)$  evolve linearly. (Ablowitz, et al. 1974). Once we know these amplitudes at a later time, the transform may be inverted to find the solution of the MKdV equation at that time. This is the most complicated step of the inverse scattering

method, involving a set of integral equations that must be solved numerically. However, the transformation may be simplified by approximating  $u(x, t)$  as a potential with the same discrete spectrum, but no continuous spectrum. This approximation is valid at large times, because the continuous spectrum of the scattering problem corresponds to the short dispersive waves that quickly propagate away (Segur 1981) as the initial condition evolves into the final large-amplitude meander. Numerical results of Pratt (1988) suggest that these dispersive waves are too small to pinch off as rings, so we will disregard this part of the solution.

By disregarding the continuous spectrum, we are left with the solution associated with the discrete spectrum, a set of solitons. A single imaginary eigenvalue,  $\xi = i\eta$ , corresponds to a loop soliton.

$$u(x, t) = \pm 2\eta \operatorname{sech}(2\eta x - 8\eta^3 t + \Delta) \quad (2.8)$$

where  $\Delta$ , the phase of the loop, is determined by  $B(\xi)$ . Because the curvature, ( $\kappa = 2a^{+\frac{1}{2}}u$ ) is of one sign, an initially uncrossed path can not evolve into a single loop soliton.

For each pair of complex eigenvalues  $\xi = \alpha(\pm 1 + i\lambda)$ , the solitary wave is known as a breather. Expressing the breather solution in terms of the path angle,  $\Theta$ ,

$$\Theta = -4 \tan^{-1}[\lambda \sin(2a^{-\frac{1}{2}}\alpha(s - c_p t) - \theta_p) \operatorname{sech}(2a^{-\frac{1}{2}}\alpha\lambda(s - c_e t) + \theta_e)] \quad (2.9)$$

Figure 2.2 shows several breathers with different  $\lambda$ . The breather is an oscillatory pattern, with wavenumber  $2a^{-\frac{1}{2}}\alpha$ , confined within an envelope of wavenumber  $2a^{-\frac{1}{2}}\lambda\alpha$ .  $\theta_p$  and  $\theta_e$  are phases of the breather and are determined by  $B(\xi)$  (Appendix A).  $\theta_p$  determines the orientation of the oscillation with respect to the envelope, and  $\theta_e$  determines the position of the envelope.

The envelope speed  $c_e = 12\alpha^2(1 - \frac{1}{3}\lambda^2)$  is the speed at which the envelope propagates along the path. Breathers with small  $\lambda$ , i.e. small steepness, have an envelope speed close to the group speed for linear waves with the same wavelength

$2a^{\frac{1}{2}}\alpha$ , so they are hard to distinguish from the background dispersive wavetrain. The phase speed,  $c_p = 4\alpha^2(1 - 3\lambda^2)$ , determines the speed at which the oscillations propagate. Because the envelope and oscillations move at different speeds, the pattern fluctuates as successive maxima of the sinusoid pass through the peak of the envelope. The period for these fluctuations is

$$T = \frac{2\pi}{2a^{\frac{1}{2}}\alpha} \div (c_p - c_e) = \frac{\pi a^{\frac{-1}{2}}}{8\alpha^3(1 + \lambda^2)} \quad (2.10)$$

The steepness of the breather is determined by  $\lambda$ . If  $\lambda > \tan(\frac{\pi}{8})$ , then  $|\Theta|_{max} > \frac{\pi}{2}$ , and the path becomes multi-valued (Figure 2.2b). Pratt (1988) showed that when a meander becomes multi-valued (so that  $dx$  becomes negative) its amplitude increases, because the area  $\int l dx$  remains constant with time. He concluded that multi-valuedness is a possible indication of a finite amplitude instability mechanism.

Multi-valued breathers have a “neck” which is defined as the smallest separation in longitude between two points on the path. As  $\lambda$  increases, the breather steepens, forming a narrower neck. When the neck width vanishes, points separated along the path come into grazing contact, and the coordinate transformation of section 1.2 is no longer valid. Because the path is pinched together, other physical processes are dominant which we assume aid the detachment of the closed meander. The actual neck width of a breather must be calculated numerically, and it vanishes at some time when  $\lambda \geq 1$ . Figure 2.3 shows the  $\lambda = 1$  breather at several times in its oscillation cycle. Although it is pinched together when the path is symmetric ( $t = 0, \frac{T}{2}, T$ ), at other times the path is unclosed. We can determine which initial conditions form rings, by finding the initial conditions for which the scattering problem, Equation 2.8 yields eigenvalues for which  $\lambda \geq 1$ .

The MKdV equation arises in plasma physics (Torve, 1981) and electric circuit theory (Scott, 1970). Redekopp (1977) found that certain finite amplitude Rossby waves in a stratified fluid are described by the MKdV equation and Redekopp and Weidman (1978) briefly discuss the breather solutions. However, because these examples of the MKdV equation arise in very specific physical settings, there has

been little work on actually applying the inverse scattering transform to specific initial value problems of the MKdV equation. In this thesis the evolution of several different kinds of initial meanders will be predicted using the inverse scattering transform. We are specifically interested in determining how an initial meander must be shaped in order to evolve into a pinched off ring.

## 2.3 Piecewise Constant Curvature

In quantum mechanics, a piecewise constant potential is often used as the simplest potential which is capable of having bound states. This scattering problem may be solved algebraically and although it is highly idealized, it illustrates how the size and shape of a potential determine the discrete eigenvalue spectrum. Following this approach, we will first consider piecewise constant curvature meanders in order to determine which shapes will evolve into breathers.

When the meander has piecewise constant curvature, it is easier to solve the scattering equation (Equation 2.8) as the equivalent set of coupled first order equations (Lamb, 1980),

$$\frac{d\phi_1}{dx} + i\xi\phi_1 = u(x)\phi_2 \tag{2.11}$$

$$\frac{d\phi_2}{dx} - i\xi\phi_2 = -u(x)\phi_1$$

with boundary conditions

$$\begin{bmatrix} \phi_1 \\ \phi_2 \end{bmatrix} \sim \begin{bmatrix} e^{-i\xi x} \\ 0 \end{bmatrix}, \quad x \rightarrow -\infty \tag{2.12}$$

$$\begin{bmatrix} \phi_1 \\ \phi_2 \end{bmatrix} \sim \begin{bmatrix} Ae^{-i\xi x} \\ Be^{i\xi x} \end{bmatrix}, \quad x \rightarrow +\infty$$

For a single “square well” of curvature, the potential can be written,

$$u = \begin{cases} u_1 & \text{if } l_0 < x < l_0 + l_1 \\ 0 & \text{otherwise} \end{cases} \quad (2.13)$$

According to Equation 2.11, the solution to the left of the well is

$$\begin{aligned} \phi_1 &= e^{-i\xi x} \\ \phi_2 &= 0 \end{aligned} \quad (2.14)$$

Inside the well, the solutions are the standing waves,

$$\begin{aligned} \phi_1 &= C \cos\Delta_1 x + D \sin\Delta_1 x \\ \phi_2 &= C(i\frac{\xi}{u_1}\cos\Delta_1 x - \frac{\Delta_1}{u_1}\sin\Delta_1 x) + D(\frac{\Delta_1}{u_1}\cos\Delta_1 x + i\frac{\xi}{u_1}\sin\Delta_1 x) \end{aligned} \quad (2.15)$$

where  $\Delta_1 = \sqrt{u_1^2 + \xi^2}$ . To the right of the well, the solution is

$$\begin{aligned} \phi_1 &= A_1 e^{-i\xi x} \\ \phi_2 &= B_1 e^{i\xi x} \end{aligned} \quad (2.16)$$

where  $\{A_1, B_1\}$  are the amplitudes we want to find. The constants  $\{C, D, A_1, B_1\}$  are determined by matching  $\phi_1$  and  $\phi_2$  at  $l_0$  and  $l_0 + l_1$ . We find  $\{A_1, B_1\}$  to be

$$A_1 = (\cos\Delta_1 l_1 - \frac{i\xi}{\Delta_1} \sin\Delta_1 l_1) e^{i\xi l_1} \quad (2.17)$$

$$B_1 = (-\frac{u_1}{l_1} \sin\Delta_1 l_1) e^{i\xi l_1} \quad (2.18)$$

By finding the zeros of  $A_1(\xi)$ , we can determine the solitons that will evolve from this initial path, with a single well of curvature. Because the initial path has only one sign of curvature, it does not represent a meander in a zonal jet (and is therefore not realistic for the model), but rather a “bent” path, like a hairpin. By examination, we see that the only  $\xi$ 's that are zeros of  $A_1$  are purely imaginary, corresponding to the loop soliton which also has one sign of curvature. We can determine the minimum

size of the square well which forms a loop soliton, by determining the value of  $u_1 l_1$  that satisfies  $A_1 = 0$ , when  $\xi = 0$ . By examination we find  $u_1 l_1 = \frac{\pi}{2}$ , which corresponds to a path that is curved completely back on itself ( $\Theta = 2u_1 l_1 = \pi$ ).

This idea can be extended to find  $\{A_n, B_n\}$ , the amplitude coefficients for an n-square well potential. Figure 2.4 shows a 3-square well potential and its associated path.

Knowing  $\{A_{i-1}, B_{i-1}\}$ , the right edge amplitudes in the absence of the  $i^{th}$  square well, which has length  $l_i$ , and amplitude  $u_i$ , we can find  $\{A_i, B_i\}$ , the amplitude coefficients at the right edge, (at  $x = \sum_{n=1}^i l_n = L_i$ ) with the following iterative formula

$$A_i = (\cos \Delta_i l_i - \frac{i\xi}{\Delta_i} \sin \Delta_i l_i) e^{i\xi l_i} A_{i-1} + (\frac{u_i}{\Delta_i} \sin \Delta_i l_i) e^{i\xi(L_i+L_{i-1})} B_{i-1} \quad (2.19)$$

$$B_i = (-\frac{u_i}{\Delta_i} \sin \Delta_i l_i) e^{-i\xi(L_i+L_{i-1})} A_{i-1} + (\cos \Delta_i l_i + \frac{i\xi}{\Delta_i} \sin \Delta_i l_i) e^{-i\xi l_i} B_{i-1} \quad (2.20)$$

where  $A_0 = 1$ ,  $B_0 = 0$ . The breathers associated with a specific n-square well path may then be found by locating the zeros of  $A_n$  using Newton's method in the complex plane. Because we have an algebraic expression for  $A_n$ , we can fully explore the parameter space made up of the  $u_i$ 's, and the  $l_i$ 's, testing how variations in path angles and arc lengths change the location of the eigenvalues,  $\alpha(\pm 1 + i\lambda)$ .

The scattering problem is linear, so all of the wavenumbers and length scales are linearly related. Therefore, for each scattering problem, we choose one of the  $l_i$ 's as a fixed scale, ( $l_i = 1$ ), and measure all of the other lengths relative to this scale. Because we are mainly concerned with when breathers just begin to form ( $\lambda = 0$ ), where they can be multi-valued, ( $\lambda = \tan(\frac{\pi}{8})$ ), and ring forming ( $\lambda = 1$ ), we will in practice specify the eigenvalue, and determine which parameters satisfy Equation 2.20.

In this chapter, the iterative formula will be used to find the breathers associated with several piecewise constant curvature steps. A step has two regions of length  $l_1$ , and  $l_3$ , with constant curvature  $u_1$ , and  $u_3$ . The path must be zonal

on either side of the step, so the two curvature regions must form the same angle  $2u_1l_1 = -2u_3l_3 = \Theta_0$ . These two uniform curvature segments may be adjacent or separated by a straight line segment of length  $l_2$ .

The scattering coefficients associated with this type of meander are

$$A = \left[ \left( \cos \Delta_1 l_1 - i \frac{\xi}{\Delta_1} \sin \Delta_1 l_1 \right) \left( \cos \Delta_3 l_3 - i \frac{\xi}{\Delta_3} \sin \Delta_3 l_3 \right) e^{i\xi(l_1+l_3)} - \frac{u_1 u_3}{\Delta_1 \Delta_3} \sin \Delta_1 l_1 \sin \Delta_3 l_3 e^{2i\xi l_2} e^{i\xi(l_1+l_3)} \right] \quad (2.21)$$

$$B = \left[ -\frac{u_3}{\Delta_3} \sin \Delta_3 l_3 \left( \cos \Delta_1 l_1 - i \frac{\xi}{\Delta_1} \sin \Delta_1 l_1 \right) e^{-i\xi l_2} e^{-i\xi(l_3+l_1)} e^{-2i\xi l_2} - \left( \cos \Delta_3 l_3 + i \frac{\xi}{\Delta_3} \sin \Delta_3 l_3 \right) \frac{u_1}{\Delta_1} \sin \Delta_1 l_1 e^{-i\xi(l_3+l_1)} \right] \quad (2.22)$$

Figure 2.5 shows how the zeros of Equation 2.21 vary with the step angle, when the step is symmetric and has no center curvature region. When the step has a small angle, the only zeros to Equation 2.21 are in the lower complex plane, region I, so there are no breathers formed. As the angle increases, the zeros move across the real axis, into the upper complex plane where the pair  $\alpha(\pm 1 + i\lambda)$  is associated with a breather. When  $\lambda < \tan(\frac{\pi}{8})$ , the breathers are single-valued. As the step angle increases further, the zeros move into region III, where they are associated with steps that form multi-valued breathers. For steps with  $\lambda > 1$ , the zeros are in region IV, and can form rings.

We can determine the critical angle at which breathers form, by determining the step angle at which the zeros cross the real axis. For a symmetric ( $l_1 = l_3$ ) step, which also has  $l_2 = 0$ , this angle can be found analytically. Setting  $\lambda = 0$ , in Equation 2.21,

$$A = \left( 1 - 2i \frac{\alpha}{\Delta_1} \sin \Delta_1 l_1 \cos \Delta_1 l_1 - 2 \frac{\alpha^2}{\Delta_1^2} \sin^2 \Delta_1 l_1 \right) e^{-2i\xi l_1} \quad (2.23)$$

Setting the real and imaginary part of A to 0, leads to

$$\begin{aligned} \sin\Delta_1 l_1 \cos\Delta_1 l_1 &= 0 \\ \sin^2\Delta_1 l_1 &= \frac{\Delta_1}{2\alpha^2} \end{aligned}$$

This implies that  $\Delta_1 l_1 = \frac{\pi}{2}$ , and  $\Delta_1^2 = 2\alpha^2 = 2u_1^2$ . Combining these we can find the minimum angle for breather formation,  $\Theta_0 = \frac{\pi}{\sqrt{2}}$ .

An asymmetric step is formed when  $l_1 \neq l_3$ , so the radius of curvature for the two folds are different. In order to isolate the effect of the symmetry,  $l_2$ , the length of the straight center piece (indicated by the dashed line in Figure 2.3), will be set to 0. According to Equation 2.22,  $B(\xi)$  depends on the relative position of the small and large folds, so the phases of the breather,  $\theta_p$  and  $\theta_e$ , will depend on the positioning. However, the zeros of Equation 2.21 do not depend on the positioning, only the relative radii of the two folds. Two steps with the same size small fold, but opposite positions of this fold will form identical breathers, but they will have different positions and orientations. Equation 2.21 indicates that there is a similarity in the solutions. If the lengths  $l_i$  are replaced with  $\frac{l_i}{l_1}$ , then the eigenvalues become  $l\xi$ .

Figure 2.6 shows how the shape of the breather depends on  $\Theta_0$  and the symmetry, which is defined as the ratio of the small radius of curvature to large. For simplicity, we will assume that  $l_1 = 1$ , so that the symmetry is just  $l_3$ , which is less than 1. A step which lies to the right of the dashed line intersects itself, and is thus unphysical. For small values of  $\Theta_0$ , region I, the step disperses into a train of short waves. As  $\Theta_0$  increases beyond  $\frac{\pi}{\sqrt{2}}$ , the step falls in region II, breathers are possible and the step evolves into a broad, single-valued packet of waves, because  $\lambda < \tan(\frac{\pi}{8})$ . As the symmetry of the step decreases, the angle at which breathers form slowly increases until the symmetry is very small, where it rises sharply to  $\pi$ . As the symmetry decreases below 0.05 several very short single-valued breathers begin to arise. Because they arise at such small symmetries, they stay crowded into the region of the parameter plane to the right of the critical angle for breather

formation, and lie below  $l_3 = 0.05$ . In addition, these secondary breathers are short, fast and indistinguishable from the dispersive wavetrain, and they will not be apparent in the solution.

The steeper steps of region III form multi-valued breathers, with  $\lambda > \tan(\frac{\pi}{8})$ . The symmetric step begins to form multi-valued breathers when  $\Theta_0 \approx \pi$ . As the symmetry decreases, the angle at which multi-valued breathers form gently increases until the smaller radius of curvature is less than  $\frac{1}{10}$  of the larger. Then this angle abruptly decays back to  $\pi$ .

Steps within region IV have angles steep enough so that the breather forms a closed loop. For a symmetric step, when  $\Theta_0 = 4.16$  a ring can form. This critical angle is insensitive to changes in symmetry until the symmetry is  $\approx \frac{1}{10}$ , where the critical angle goes to  $\pi$ .

The size of the breather also decreases most rapidly with decreasing symmetry, at small symmetries. Figure 2.7 shows  $\alpha$ , the oscillation wavenumber, for breathers with  $\lambda = \tan(\frac{\pi}{8})$ . These breathers lie on the lines dividing regions II and III in Figure 2.6. The symmetry decreases to 0.2 before the wavenumber has doubled. As the symmetry decreases further to 0.1, the wavenumber rapidly increases to ten times its value for the symmetric step. Not only does this indicate that a much smaller breather is formed, but also a thousand-fold decrease in the time scale.

We can interpret the small symmetry limit by turning back to the single square well discussed at the beginning of this section. As the step becomes more asymmetric, one of the two curvature wells becomes infinitely long, but has no curvature associated with it. while the other well becomes a delta function of curvature. Loop solitons are possible then, and the solution passes from a dispersive wavetrain, directly to loop solitons as the path angle passes through  $\pi$  (recall that this is the path angle associated with loop solitons found for the single square well).

A stretched symmetric step is one for which  $l_1 = l_3$ , and  $l_2 \neq 0$ . In this case the length scale  $l_1$  is set equal to 1. Figure 2.8 shows how  $\Theta_0$  and  $l_2$  determine the properties of the breather that evolves out of a wide, symmetric step. Region I again denotes the dispersive steps, and region II the breather-forming steps. As  $l_2$

increases from 0, the step angle at which breathers form quickly decreases, and then slowly asymptotes to  $\frac{\pi}{2}$ . The angles at which multi-valued and closed breathers (the lines denoting regions III and IV) also quickly decrease to asymptotic values.

At large values of  $l_2$ , multiple single-valued breathers can form, as they did for the step with small symmetry. A second multi-valued breather is possible for extremely wide ( $l_2$ ), and steep ( $\Theta_0 \approx \pi$ ) steps (Figure 2.8).

The asymptotic values and the secondary breathers can be found by turning back to the scattering problem. As the separation between the wells gets large, the wavelength of the breather increases, so the width of the wells (fixed by the scaling  $l_1 = 1$ ) becomes small relative to this wavelength. The scattering problem begins to resemble the elementary physics problem of reflections in a thin film. From this type of problem we know (see e.g. Feynmann, 1965) that as  $l_2 \rightarrow \infty$ ,

$$\alpha l_2 \rightarrow \frac{(2n'-1)\pi}{2} \quad \text{where } n' = 1, 2 \dots \quad (2.24)$$

The number of breathers, or trapped waves in the scattering problem, is determined by  $n'$ . Using this relation in equation 2.16, we find

$$\cos^2 \frac{\Theta_0}{2} + \sin^2 \frac{\Theta_0}{2} (-e^{-\lambda(2n'-1)\pi}) = 0 \quad (2.25)$$

which reduces to

$$\cos \Theta_0 = -\tanh \lambda \frac{(2n' - 1)\pi}{2} \quad (2.26)$$

The angles for multi-valued breather and ring formation at large  $l_2$  can be determined from this equation, with  $n' = 1$ , and are indicated in Figure 2.8. The minimum angle for ring formation is  $\Theta_0 = 2.73$ . The shorter secondary breathers ( $n' = 2, 3, \dots$ ) of Figure 2.8 are harmonics of the scattering problem. The step must be essentially closed ( $\Theta_0 = 3.12$ , at large  $l_2$ ) for a closed breather with  $n' = 2$  to form, so only one ring can form from a piecewise constant curvature step. When  $\lambda = 0$ , we see that the minimum angle for breather formation is always  $\frac{\pi}{2}$ . Thus, the step must be multi-valued to form breathers.

With the iterative formula developed in this section, we can determine the solitons that will emerge from a path with an arbitrary number of constant curvature sections. As a simple first example, a path with two curvature regions is considered. This curvature distribution forms a step which disperses unless its maximum angle is greater than some critical value. If the step is symmetric, and the regions of constant curvature are adjacent to each other, then the step must have a maximum angle greater than  $\frac{\pi}{\sqrt{2}}$ , in order for breathers to form. If the step is made steeper, so that  $\Theta_0 > \pi$ , then a multi-valued breather may emerge. As the maximum angle increases beyond  $\Theta_0 \approx 4.1$ , then a pinched off ring will form. If the step is made asymmetric, so that the two curvature regions are asymmetric, the critical angles for breather, multi-valued breather, and ring formation all asymptote to  $\pi$ , as the symmetry of the step approaches 0. At small symmetries, below 0.05, regions with small curvature get long, and multiple single-valued breathers may form. As the symmetry decreases further, the step is passing through the single square well limit, where only a loop soliton is possible, This occurs when  $\Theta_0 = \pi$ , where the step collapses on itself, and is unphysical.

The presence of a flat center section stretches the step, causing the angles at which breathers and rings form to decrease. For wide steps, such that  $l_2 \gg l_1$ , we can show that the minimum angle for breather formation is  $\frac{\pi}{2}$ ; piecewise constant curvature steps must be multi-valued to form breathers. The minimum angle for ring formation is found to be  $\Theta_0 \approx 2.7$ .

## 2.4 Smooth Steps

We now compare the criteria found for the simple piecewise constant steps with criteria for more realistic smooth steps. The scattering problem (equation 2.4) must be solved numerically for the smooth steps. Eigenvalue problems of this sort are often solved using shooting methods (e.g. Press, 1986). However, this method relies on a good initial guess of  $\xi$ , and proved to be to difficult to use. Instead the scattering problem was broken up into a matrix eigenvalue problem by center

differencing the differential equation.

$$\begin{bmatrix} 1 & 0 & 0 & \dots & 0 & 0 & 0 \\ \frac{1}{\Delta x} & p_1 & \frac{1}{\Delta x} & 0 & \dots & 0 & 0 \\ 0 & \frac{1}{\Delta x} & p_2 & \frac{1}{\Delta x} & 0 & 0 & 0 \\ \cdot & \cdot & \cdot & \cdot & \cdot & \cdot & \cdot \\ 0 & 0 & 0 & \dots & \frac{1}{\Delta x} & p_{np-1} & \frac{1}{\Delta x} \\ 0 & 0 & 0 & 0 & 0 & 0 & 1 \end{bmatrix} \begin{bmatrix} \psi_0 \\ \psi_1 \\ \psi_2 \\ | \\ \psi_{np-1} \\ \psi_{np} \end{bmatrix} = \begin{bmatrix} 0 \\ 0 \\ 0 \\ | \\ 0 \\ 0 \end{bmatrix} \quad (2.27)$$

where  $np$  is the number of points used in the center differencing with grid spacing  $\Delta x = 1/(np-1)$ .  $p_i = -\frac{2}{\Delta x^2} + u_i^2 + iu_{x_i} + \xi^2$ . The  $np$  eigenvalues for this asymmetric operator were calculated using the NAG library. Most of the eigenvalues lie on the real axis; these eigenvalues correspond to the continuous spectrum of the eigenvalue problem. A small number of eigenvalues will occur in complex pairs of the form  $\xi = \alpha(\pm 1 + i\lambda)$ . We can not find the eigenvalues with  $\lambda$  near 0 because they are hard to distinguish from the eigenvalues on the real axis.

A smooth symmetric step can be defined as

$$\Theta = \Theta_0 \text{sech}(ks). \quad (2.28)$$

The wavenumber  $k$  will set the scale of the breather, so  $\alpha$  will be scaled by  $k$ . The shape of the breather, which is determined by  $\lambda$ , is only a function of the step angle because of the scaling of solutions.

Only one pair of discrete eigenvalues was identified for the smooth steps, indicating that there is only one breather. Figure 2.9 shows the location of these eigenvalues, for symmetric steps with angles ranging from 3.0 to 4.4. Comparing this curve to Figure 2.4, we see a qualitative similarity in the shape of these curves, although the wavenumber  $\alpha$  for the smooth steps varies less with  $\Theta_0$ . Figure 2.10 compares  $\lambda$ , the steepness parameter for the breather, as a function of the step angle for smooth steps and piecewise constant, symmetric,  $l_2 = 0$ , steps.  $\lambda$  is always larger for the piecewise constant steps, but parallels the smooth step curve. Multi-

valued breathers will form when  $\Theta_0 > 3.35$ , and closed loops form when  $\Theta_0 > 4.31$ . These are  $\approx 5\%$  larger than the critical angles determined for piecewise constant curvature steps, however, the piecewise constant results also indicate that the critical angles decrease as the step was made wider. Smooth steps are not as wide as piecewise constant steps with the same angle and amplitude, so this increase in the critical angles is consistent with the piecewise constant results.

Asymmetry was introduced by varying the scale of the step in the downstream path.

$$\begin{aligned}\Theta &= \Theta_0(\operatorname{sech} ks) & s < 0 \\ \Theta &= \Theta_0(\operatorname{sech} krs) & s > 0\end{aligned}\tag{2.29}$$

The discrete eigenvalues were found for  $r$  ranging from 1 to 10 with  $\Theta_0 = 3.5$ , and  $k = 1$ . As for the piecewise constant curvature asymmetric step, there is only one breather. The wavenumber gently increases as the symmetry decreases, reaching approximately twice of its value when the symmetry ( $r^{-1}$ ) is 0.2 (Figure 2.11). This is consistent with the decrease in size with asymmetry found for the piecewise constant curvature steps.  $\lambda$  also gently increases as the symmetry increases, and then jumps nearly to 1 at small symmetries; this can be seen in Figure 2.12 which shows the location of the eigenvalues in the complex plane as  $r$  varies. We expect that if the wavenumber  $rk$  was associated with  $s < 0$ , the same breathers would be formed.

### 2.4.1 Full Numerical Solutions

The full path equation (Equation 2.3) was solved numerically using center-differencing in space, and using a leapfrog trapezoidal method, for the time stepping. Von Neumann analysis predicts conditional stability when  $\Delta t \leq \sqrt{2} \left[ \frac{|a|}{\Delta s^3} + \frac{|b|}{\Delta s} \right]^{-1}$ . For simplicity,  $b$  will be set to 0. This is equivalent to solving the path equation in a reference frame moving with the Rossby long wave speed. The parameter  $a$  can be set to 1, without loss of generality, because it only scales the space and time variables appropriately. At the west end of the path, the path angle and curvature were fixed

to 0, while at the east end, the angle was brought down to 0 by extrapolation. This suppressed reflection from this boundary.

The numerical evolution allows us to follow the evolution and propagation of the breather, and show that the dispersive wavetrain does not form multi-valued, or closed meanders. Figure 2.13 shows the results for the symmetric step with  $\Theta_0 = 3.93$ ,  $k = 1.0$ . At  $t = 1, 2$ , the short dispersive waves are evident. While they remain for the entire integration, they are always single-valued, and unable to close on themselves and form rings. A multi-valued meander is apparent at  $t = 2.0$ . It fluctuates from the north ( $t = 6, 11, 15, 20$ ) to south ( $t = 8, 13, 18$ ) side of the path, as it slowly propagates downstream. A breather with  $\alpha = 0.38$ ,  $\lambda = 0.72$  was expected based on the Inverse Scattering results. This breather would have an oscillation period of 4.76 and amplitude of  $\approx 3$ , which is consistent with the numerical breather. The integration was carried out for several oscillation periods, and the meander did not pinch off.

Only one of the initial conditions we chose formed a ring in the numerical integration. This step, with  $\Theta_0 = 4.32$ ,  $k = 0.5$  (Figure 2.14) does not get to the fluctuating stage; instead it forms a closed loop during the first stages of breather evolution ( $t = 5.0$ ). The scattering solution predicted a breather with  $\alpha = 0.2$ , and  $\lambda = 0.97$  (Figure 2.15). This breather is not completely closed, although it is nearly so. The numerical integration shows that the dispersive waves are still quite strong just downstream of the step at  $t = 5$ , and it appears they play some kind of role in closing the ring.

We also consider the evolution of two asymmetric steps, with the small radius of curvature in the upstream and downstream path. The symmetric step with the same  $\Theta_0 = 3.5$ , and  $k = 1$  forms a large slowly-propagating meander (Figure 2.16). The breather expected by the scattering has  $\alpha = 0.39$ , and  $\lambda = 0.49$ .

The two asymmetric steps, shown in Figures 2.17, and 2.18 have a smaller radius of curvature in the downstream and upstream paths, respectively, with  $r = 5$ . The piecewise constant curvature section predicted, but did not quantify, a phase difference depending on whether the smaller radius of curvature was upstream or

downstream. These piecewise constant curvature results, and the numerical inverse scattering results, predict that the asymmetric steps will produce a smaller, steeper breather than a symmetric step with the same  $\Theta_0$ , and  $k$ .

Both of the asymmetric steps form a very small breather with  $\alpha = 0.8$ , and  $\lambda = 0.63$ . The breather in Figure 18 lags behind that of Figure 17, as the piecewise constant results predicted.

## 2.5 Conclusions

The numerical solutions to the path equation imply that the dispersive wavetrain is unable to steepen and form rings, and we are able to approximate the solution to the path equation using the inverse scattering transform. Piecewise constant curvature paths can be solved easily using the iterative formula 3.16, and even the predictions from the very simple 3-square well steps agree qualitatively well with the results for similar smooth steps.

Symmetric steps with  $l_2 = 0$  form breathers when  $\Theta_0 = \frac{\pi}{\sqrt{2}}$  and form only one, with a wavelength the same order as the length of the original step. Rings can pinch off from these steps when  $\Theta_0 \approx 4.1$ .

It appears that introducing asymmetry in the step does not have much affect on breather formation until  $l_3$  is less than 0.2. When the symmetry decreases, the angle for breather formation increases, and the angle for ring formation decreases. Both angles approach  $\pi$ , as the symmetry approaches 0. As the step becomes less symmetric, the size of the breather decreases. Asymmetric piecewise constant curvature steps and smooth steps form breathers half the size of the breathers that evolve from symmetric steps when the symmetry ( $l_3$  for the piecewise constant curvature step, and  $r$  for the smooth steps) is 0.2.

Increasing the width of the step by separating the square wells does moderately affect breather formation, causing breathers and rings to form at smaller angles. The minimum angle for breather formation is  $\frac{\pi}{2}$ , implying that only multi-valued steps can form rings. This is consistent with the contour dynamics results of Pratt and

Stern (1986), who limited themselves to single-valued steps, and found that all steps dispersed. Very broad steps, with large  $l_2$  can form closed loops with  $\Theta_0 \approx 2.7$ . The smooth steps, which are narrower than the piecewise constant curvature steps, form rings when  $\Theta > 4.31$ .

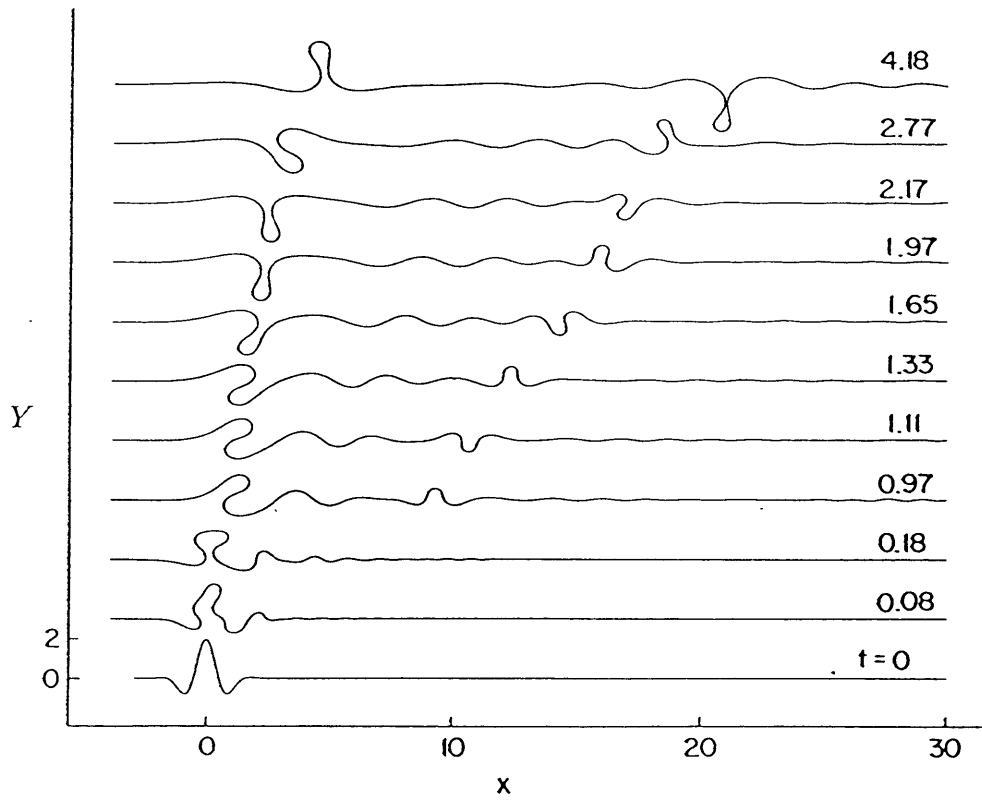


Figure 2-1: Evolution of a meander with  $a_0 = 2, k_0 = 3, w = 1$ , from Pratt 1988.

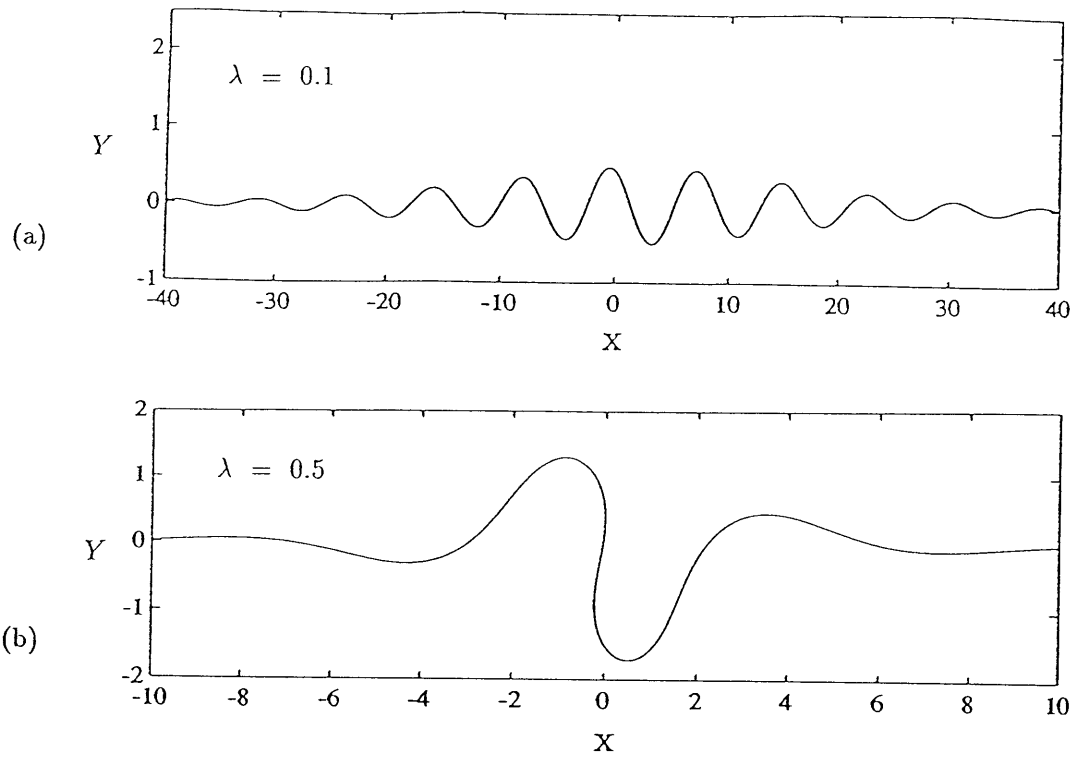


Figure 2-2: Breathers with  $\alpha = 0.4$ ,  $\lambda = 0.1$  (a),  $\alpha = 0.4$ ,  $\lambda = 0.5$  (b).

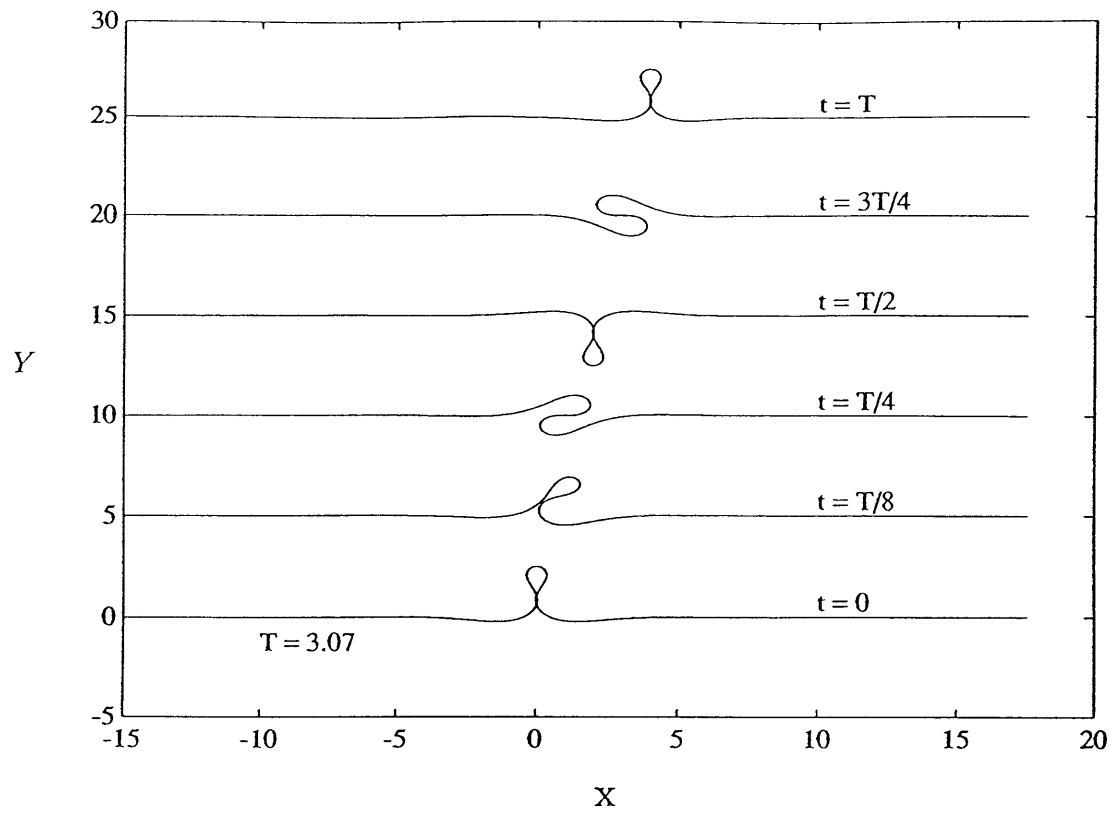


Figure 2-3: One oscillation period for breather with  $\alpha = 0.4$ ,  $\lambda = 1$

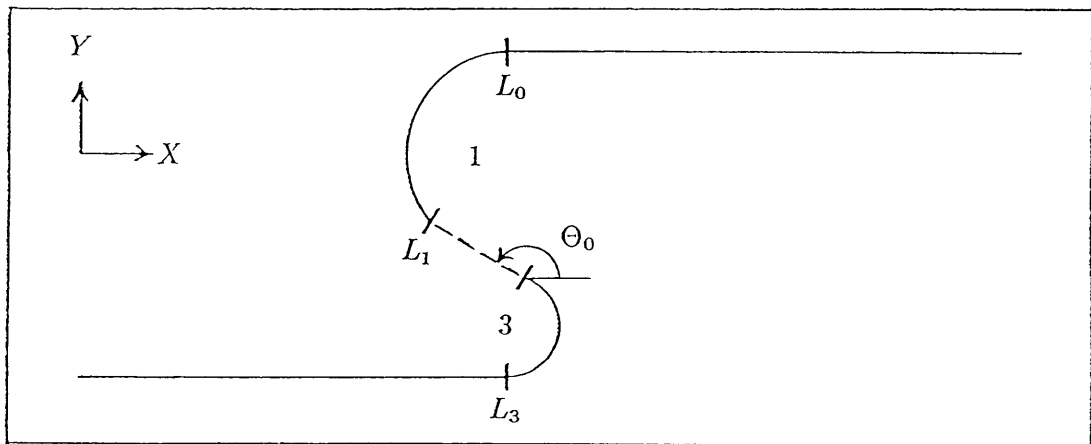
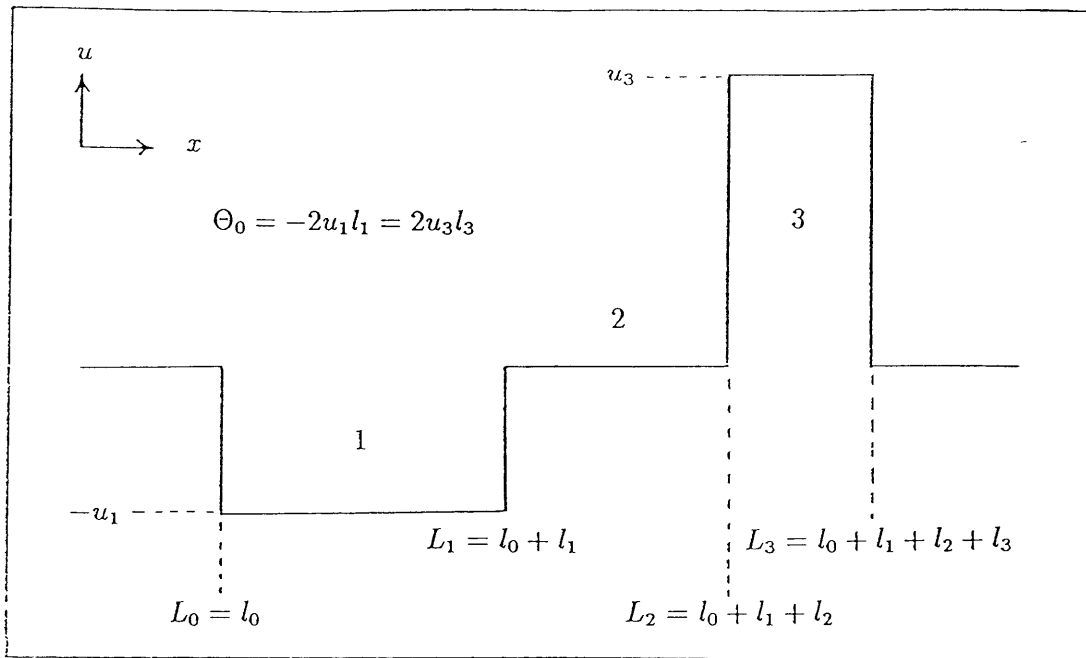


Figure 2-4: (a) Three square well scattering problem, and (b) the associated step meander (b)

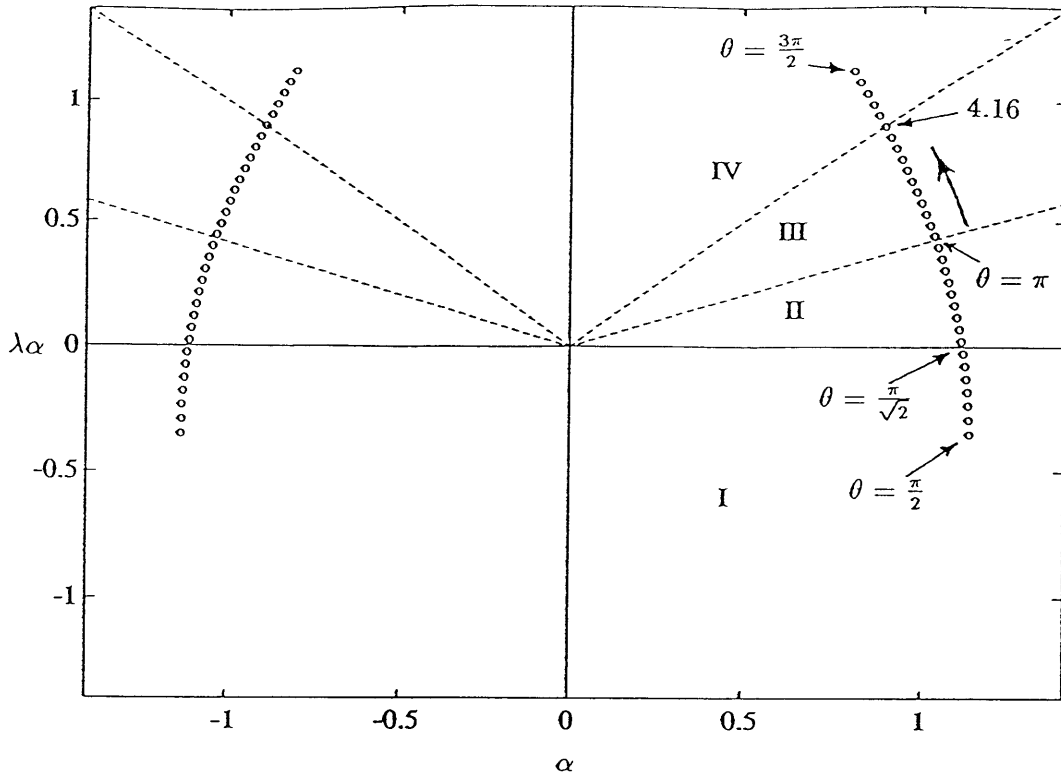


Figure 2-5: Location of the zeros of Equation 2.21 when  $l_2 = 0$ , and  $l_1 = l_3$ , for various values of  $\Theta_0$ . A breather corresponds to each zero of the form  $\xi = \alpha(\pm 1 + i\lambda)$ .

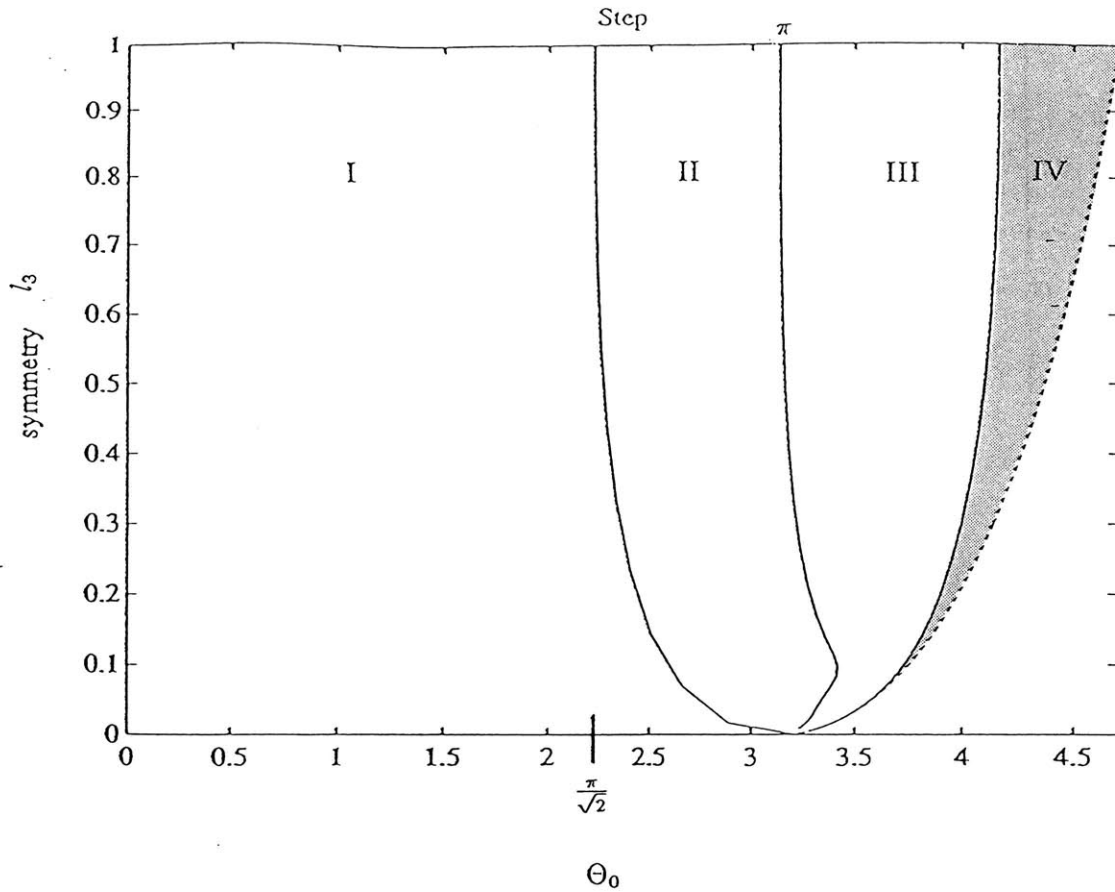


Figure 2-6: Parameter plane for asymmetric steps. Steps within: region I disperse, region II form a single-valued breather, region III form a multi-valued breather, region IV (grey) form a ring. The area to the right of the dashed line is unphysical.

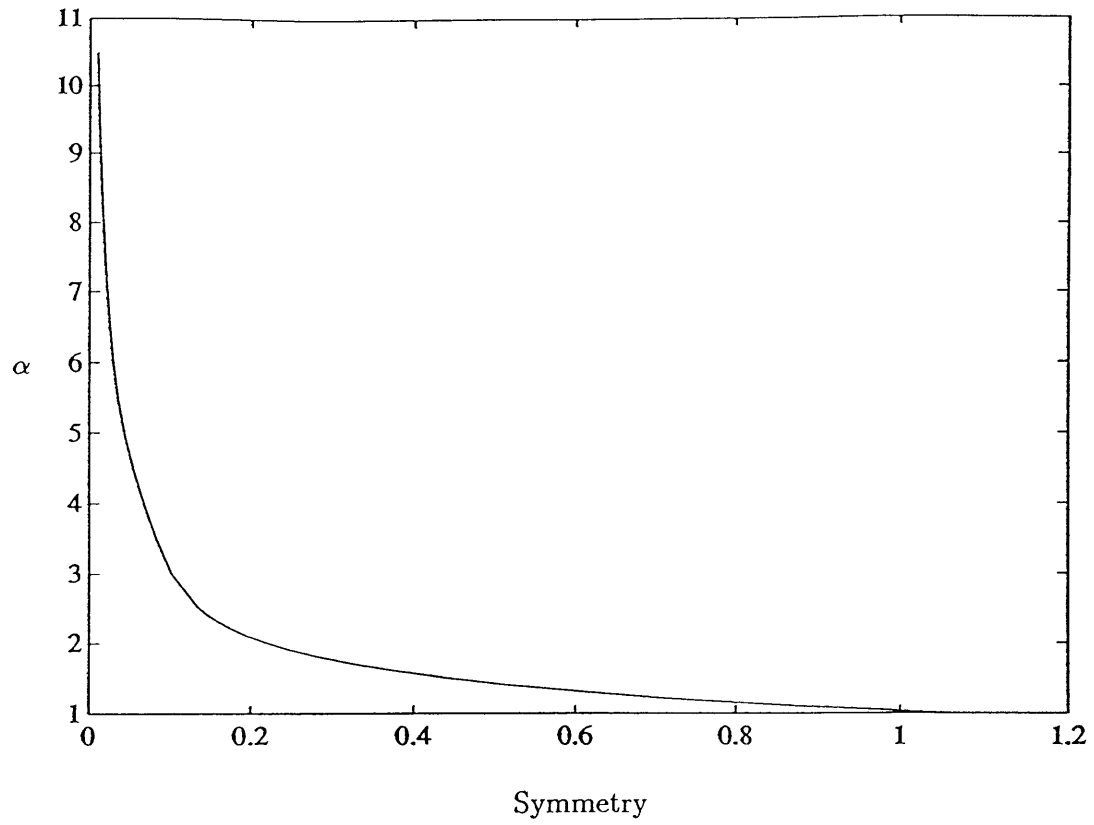


Figure 2-7: Wavenumber  $\alpha$  of the  $\lambda = \tan(\frac{\pi}{8})$  breather as a function of  $l_3$ .

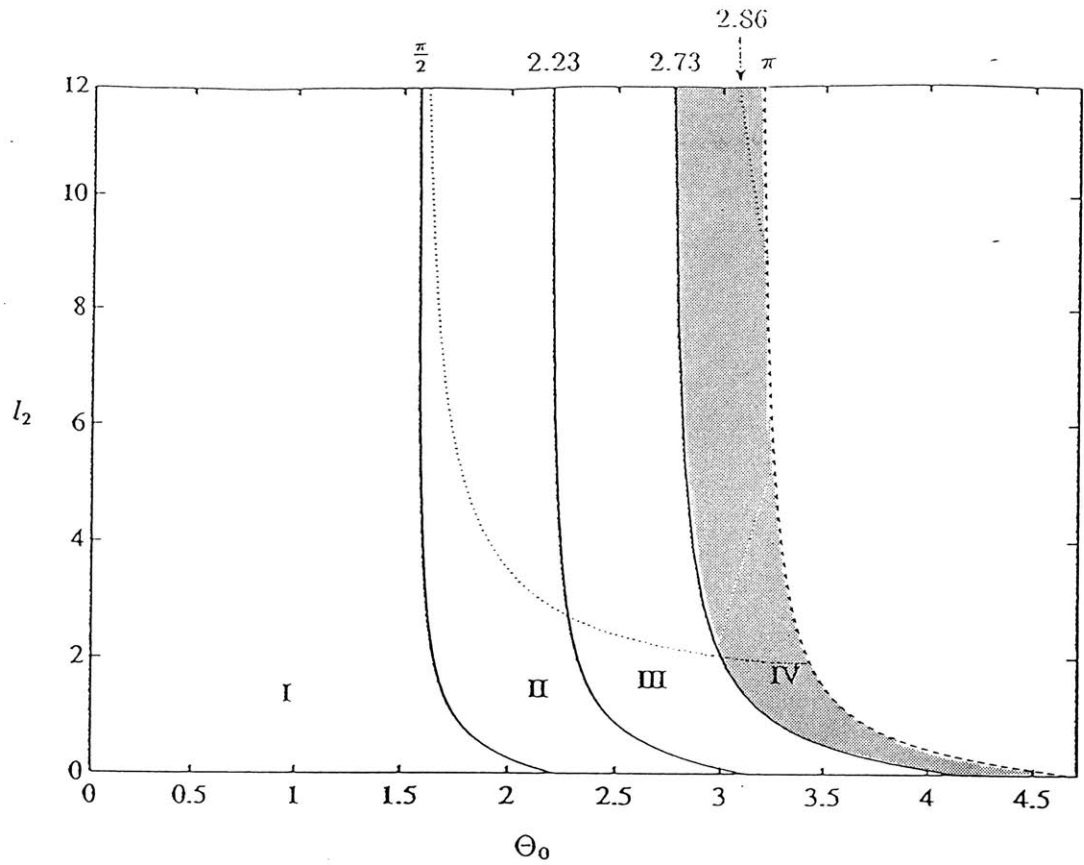


Figure 2-8: Parameter plane for wide steps with  $l_2 \neq 1$ . The numbers along the top indicate the asymptotic angles for multi-valued and ring-forming breathers at large  $l_2$ . Steps to the right of the lower dotted line form a second single-valued breather. Steps to the right of the upper dotted line form a second multi-valued breather.

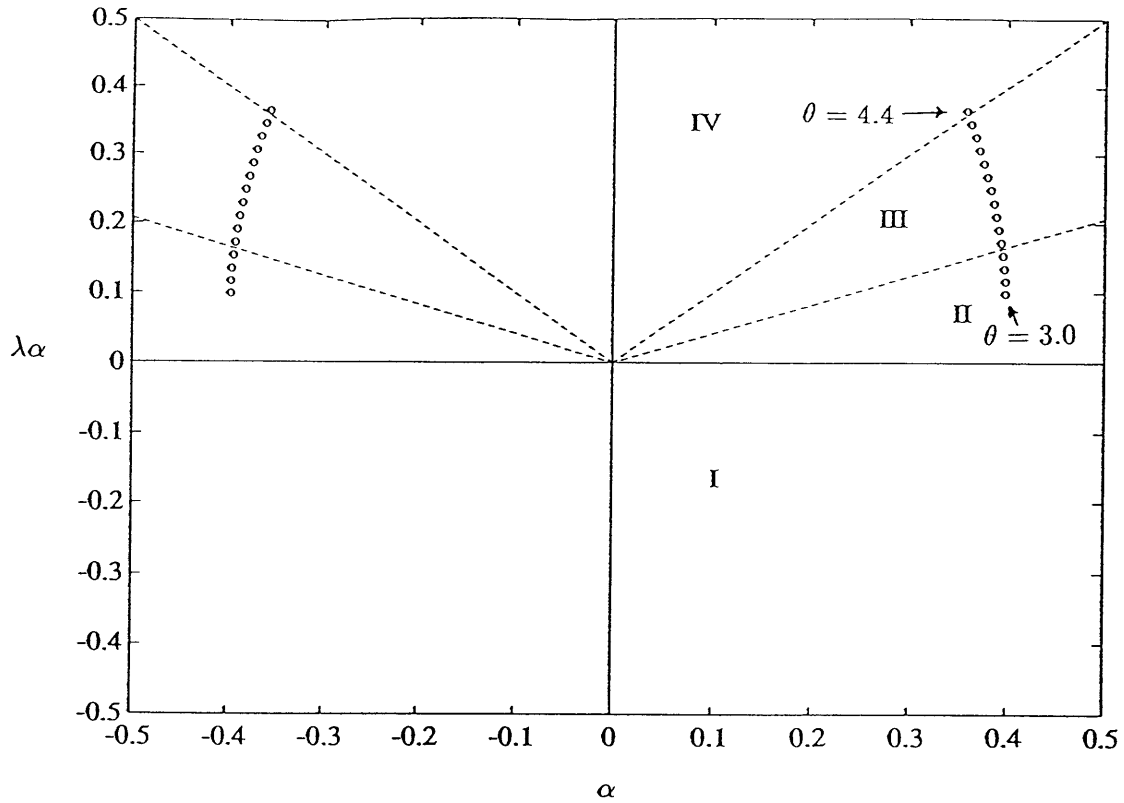


Figure 2-9: Location of the eigenvalues in the upper right complex plane for the smooth symmetric step, for  $\Theta_0$  ranging from 3.0 to 4.4.

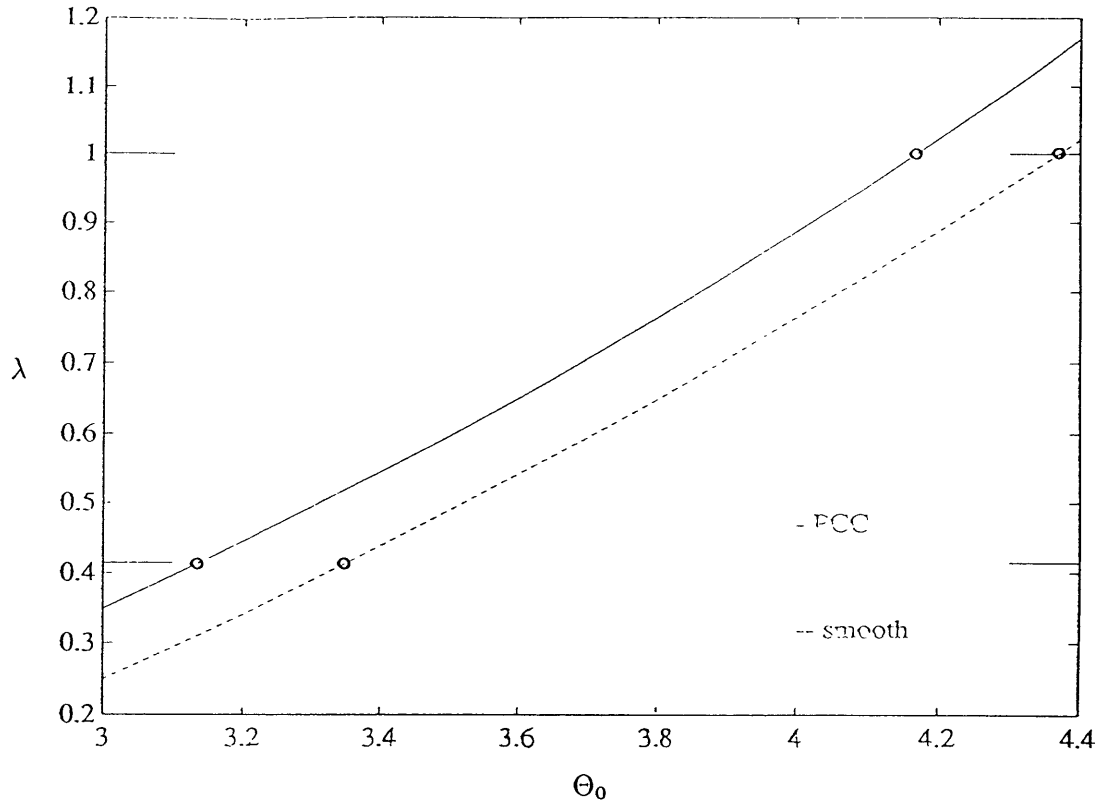


Figure 2-10: Steepness parameter  $\lambda$  as a function of step angle, for smooth (dashed line) and piecewise constant curvature (solid line) steps. Circles indicate the angle at which multi-valued and ring-forming breathers occur.

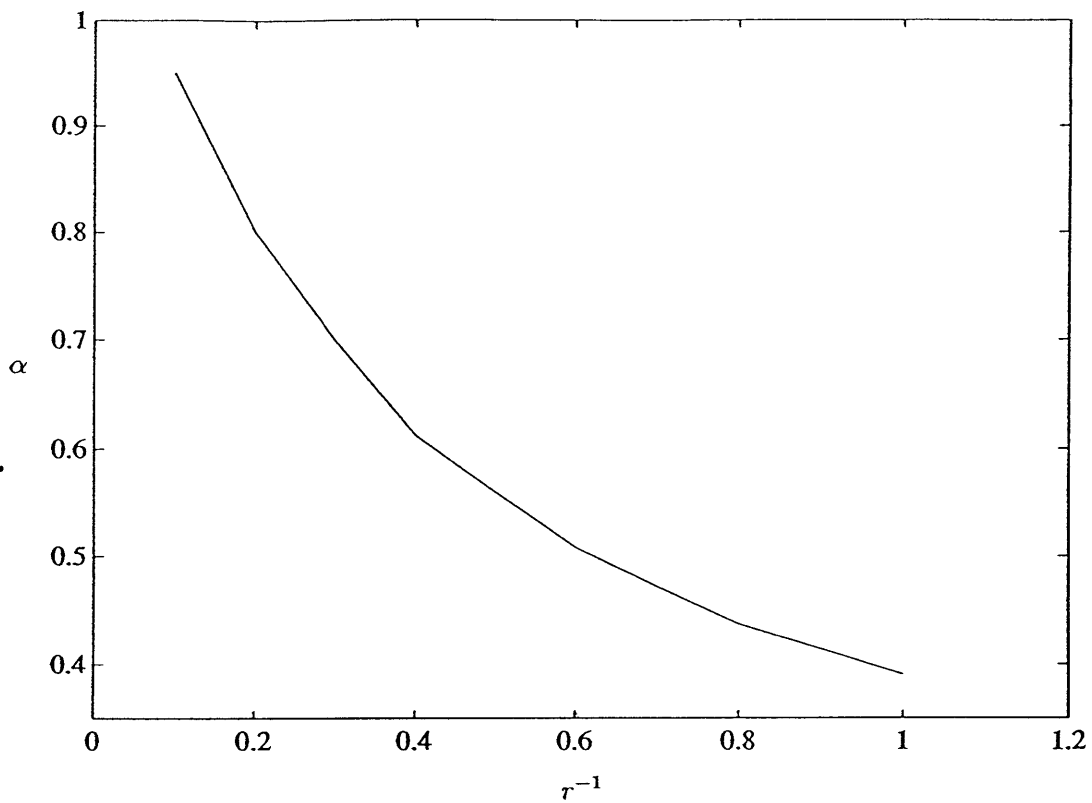


Figure 2-11: Wavenumber of the breather as a function of  $r^{-1}$ , for smooth asymmetric steps with  $\Theta_0 = 3.5$ .

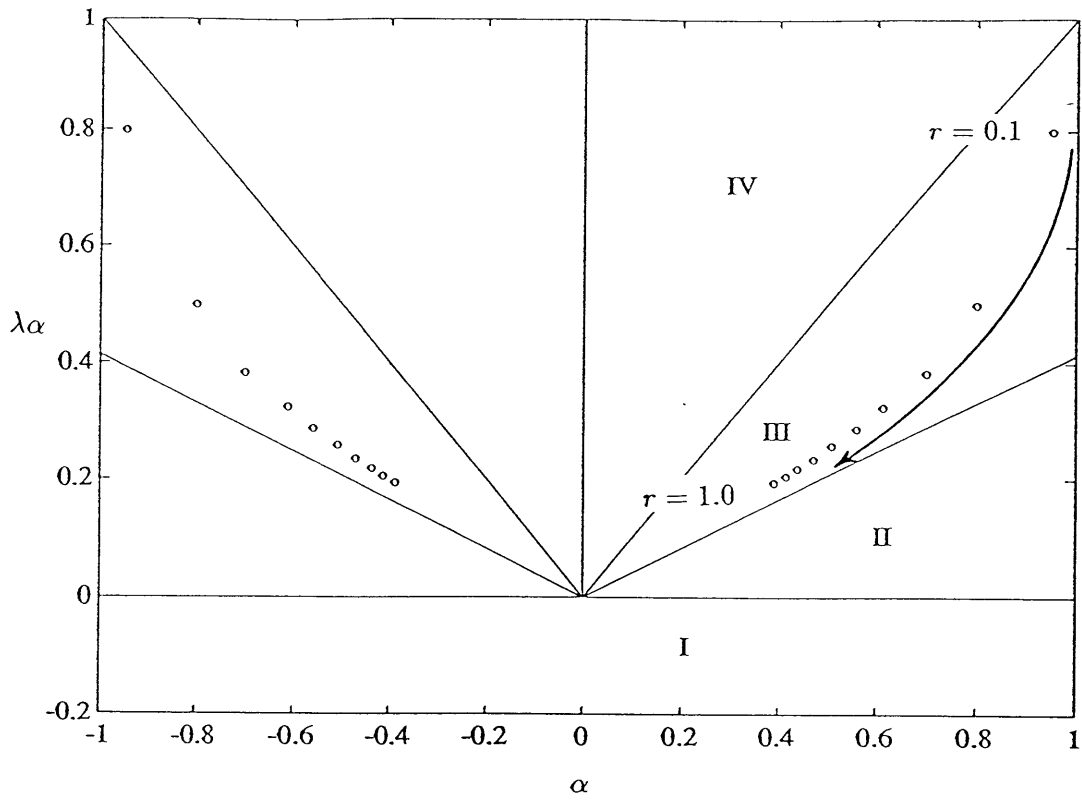


Figure 2-12: Location of the eigenvalues in the complex plane, for smooth asymmetric step with  $\Theta_0 = 3.5$ ,  $r$  ranging from 0.1 to 1.0. Arrow indicates increasing symmetry.

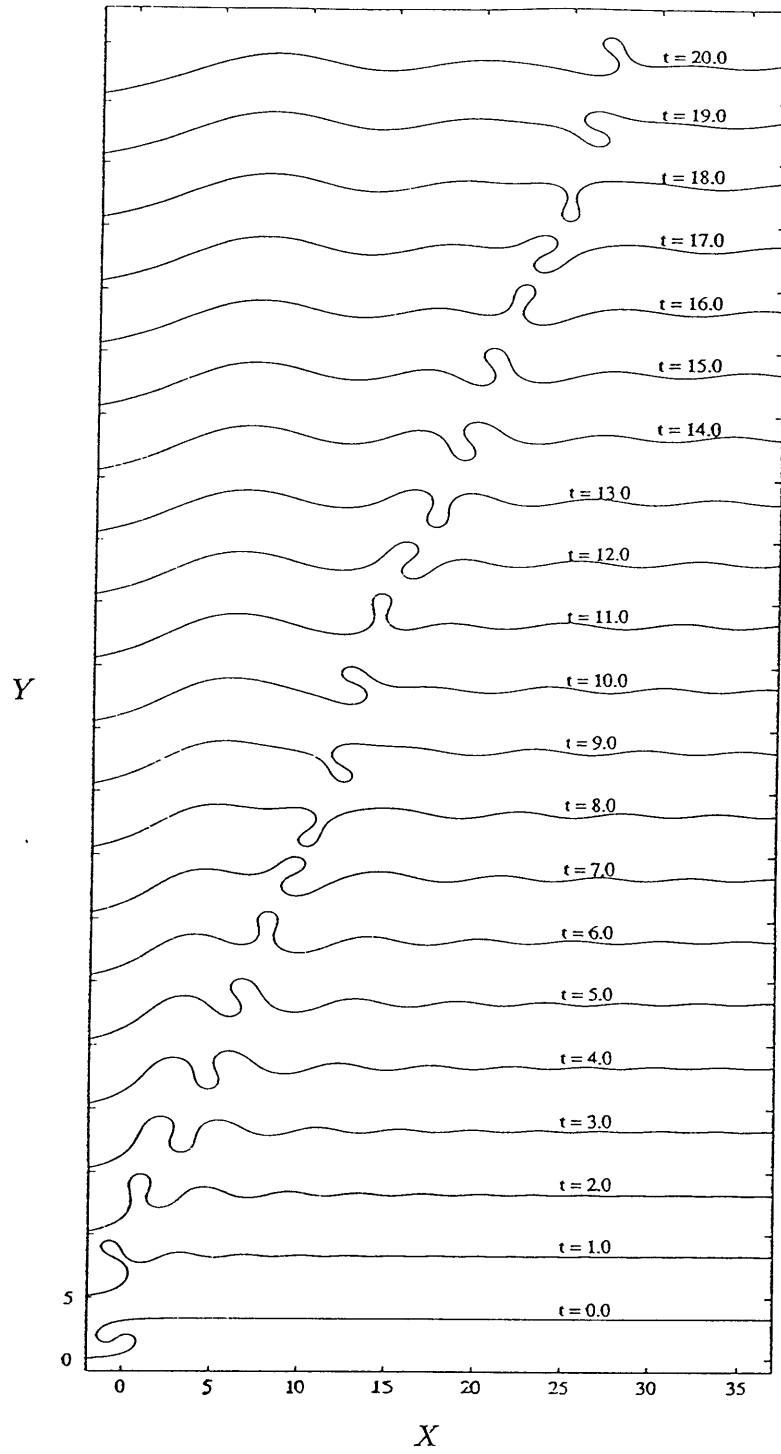


Figure 2-13: Numerical evolution for an initial symmetric step with  $\Theta_0 = 3.93, k = 1$ .

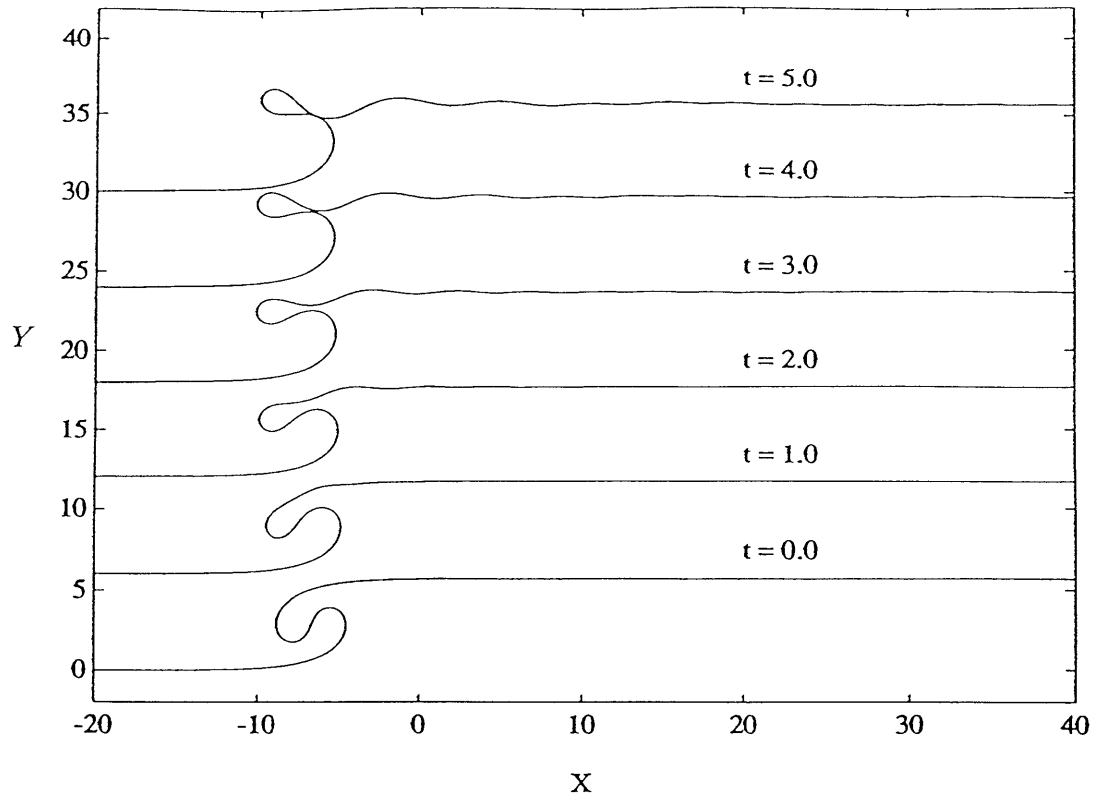


Figure 2-14: Numerical evolution for an initial symmetric step with  $\Theta_0 = 4.32, k = 1$ .

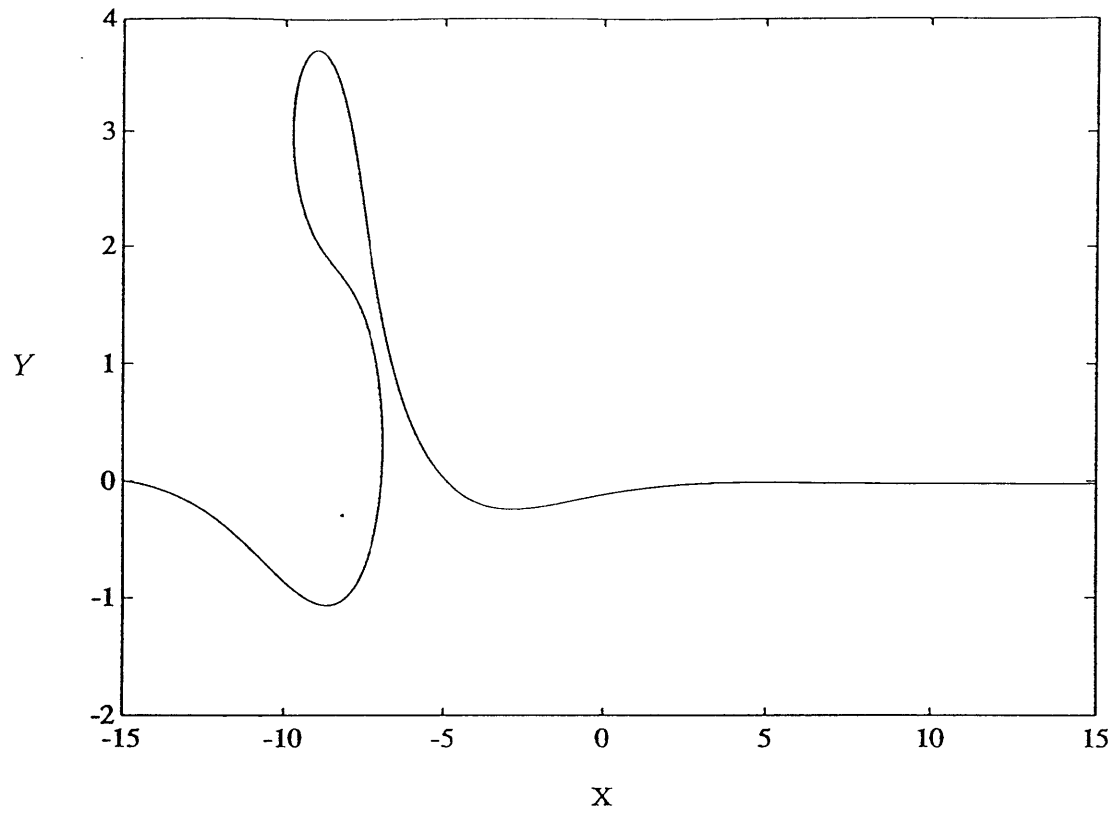


Figure 2-15: Breather with  $\alpha = 0.2, \lambda = 0.97$ .

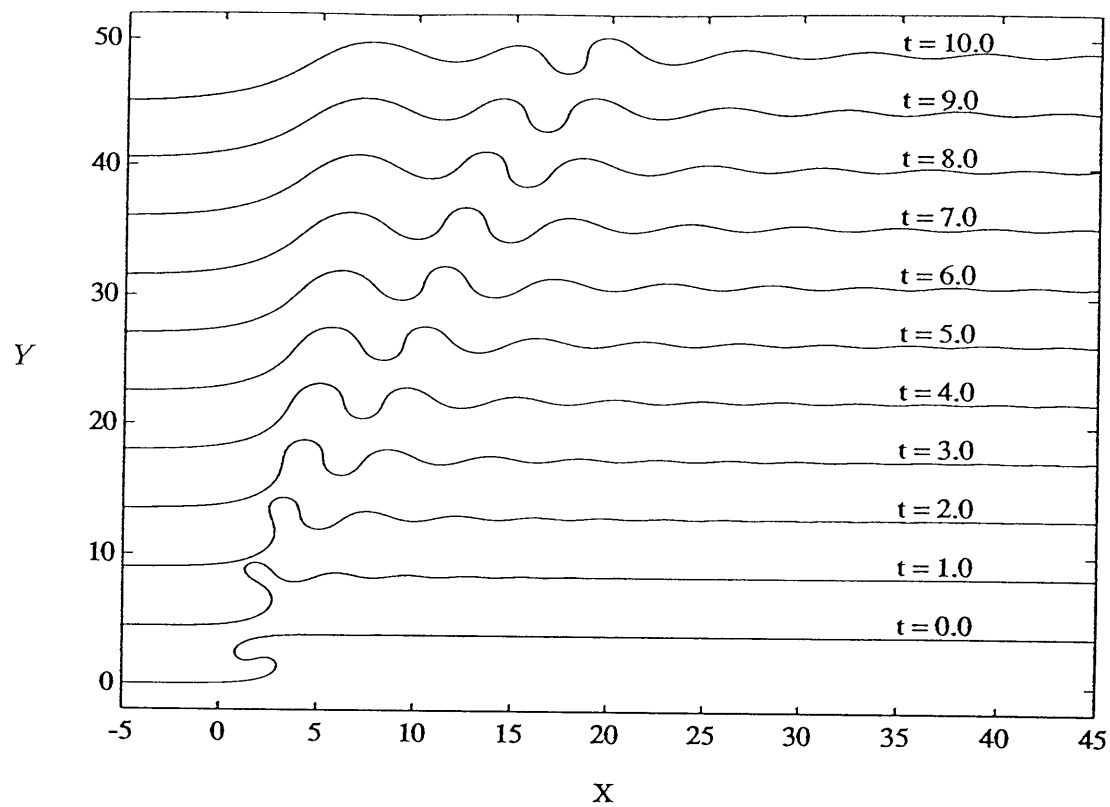


Figure 2-16: Numerical solution for an initial symmetric step with  $\Theta_0 = 3.5, k = 1$ .

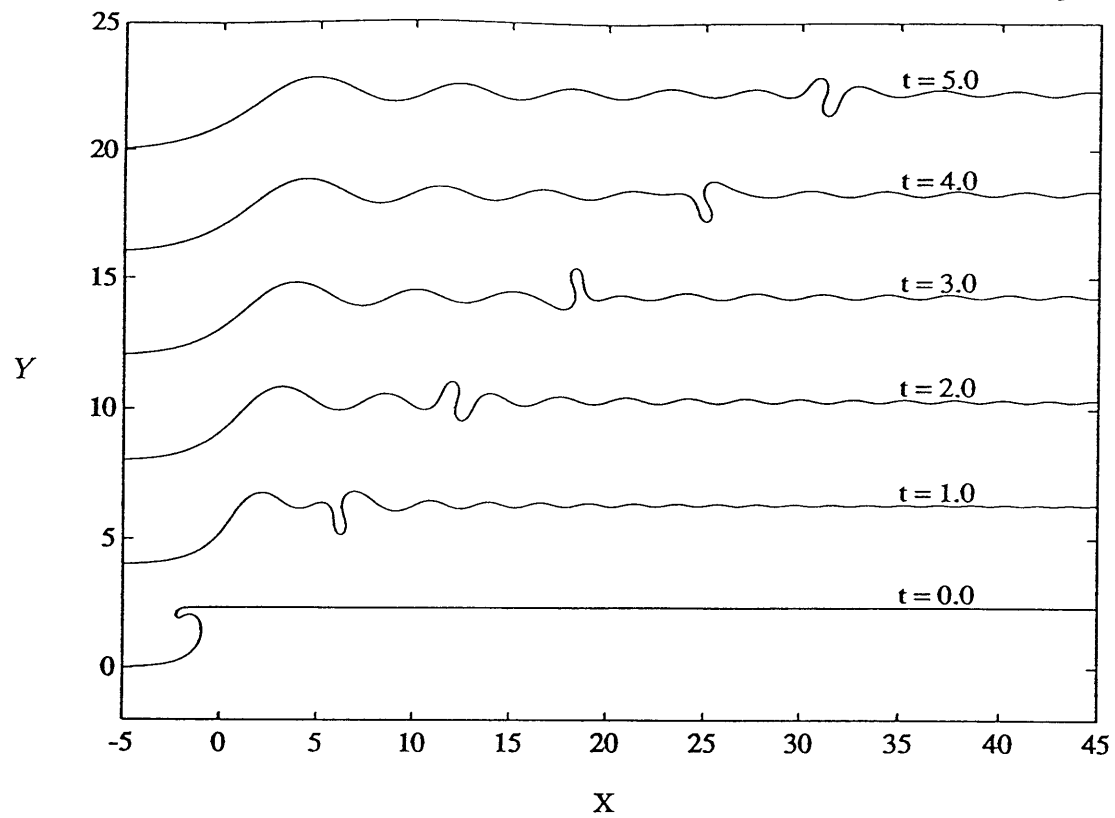


Figure 2-17: Numerical solution for an asymmetric step with  $\Theta_0 = 3.5, k = 1.$   
 $r = 5$  in the upstream path.

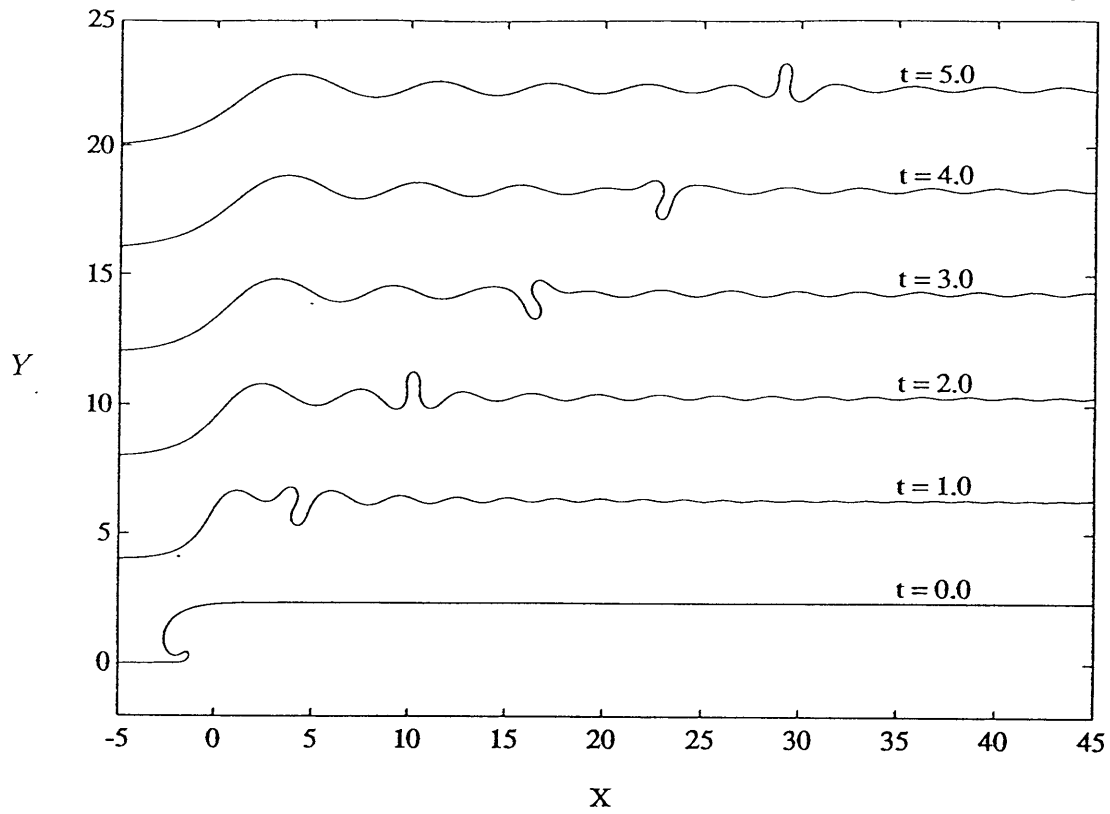


Figure 2-18: Numerical solution for an asymmetric step with  $\Theta_0 = 3.5$ ,  $k = 1$ ,  $r = 5$  in the downstream path.

# Chapter 3

## Lobes

### 3.1 Introduction

In the previous chapter we saw that steep, multi-valued steps were able to evolve into self-intersecting breathers. In this chapter we consider lobes,  $\Omega$ -shaped meanders that return to their initial latitude, to see what parameters determine ring formation. We again consider piecewise constant curvature paths for which the breathers may be found using the iterative formulae 2.19, 2.20. We also consider the evolution of several smooth lobes, and compare the maximum amplitude and curvature of the evolving meander with the breather expected by inverse scattering.

### 3.2 Integral Constraints on the Infinite Domain

Before considering the lobes in detail we first discuss two integral constraints on the curvature distribution that will aid our understanding of these lobes, and other more complicated paths. Both integral constraints apply to all isolated disturbances along an infinite path, including the steps considered in the previous chapter. However, they are included here because they help us understand the single lobe.

Integrating Equation along the entire path leads to

$$\frac{\partial}{\partial t} \int \kappa d\tilde{s} = \left[ \frac{a}{2} \kappa^3 + a \kappa_{\tilde{s}\tilde{s}} \right]_{-\infty}^{+\infty} = 0 \quad (3.1)$$

Thus the total curvature of an initial isolated disturbance will remain a constant, although it may be distributed among the dispersive waves and the solitary waves. If the disturbance is in a zonal jet then

$$\int \kappa d\tilde{s} = \int \Theta_{\tilde{s}} d\tilde{s} = 0 \quad (3.2)$$

Initially the total curvature is 0. Equation 2.8 can be rewritten as

$$\Theta_s = 4 \frac{\partial}{\partial s} \tan^{-1} \left[ \exp(-2ka^2(s + 4k^3t) + \ln \Delta) \right] \quad (3.3)$$

and by integrating this along the path we see that  $[\Theta]_{-\infty}^{\infty} = 2\pi$ . Thus a single loop soliton can not arise as the solution to a non-intersecting initial condition. From Equation 4, we also see that the breather has  $\int \kappa d\tilde{s} = 0$ . Although the dispersive waves have some curvature associated with them, no net curvature leaves the region of the breather.

An integral constraint on the distribution of curvature can be found by multiplying equation 2.2 by  $\kappa$  and then integrating along the path.

$$\frac{\partial}{\partial t} \int \kappa^2 d\tilde{s} = \frac{a}{2} \left[ 3 \frac{\kappa^4}{4} + 2\kappa \kappa_{\tilde{s}\tilde{s}} + \kappa_{\tilde{s}}^2 \right]_{-\infty}^{+\infty} \quad (3.4)$$

Thus,  $\int \kappa^2 d\tilde{s}$  is also conserved. This is one of the infinite number of conservation laws associated with the MKdV equation which constrain the evolution of an initial disturbance. Indeed, one of the early characterizations of equations that have soliton solutions is that they are associated with an infinite number of conservation laws, which account for the stability of the soliton solutions.

An initial condition has some  $\int \kappa^2 d\tilde{s}$  which gets distributed among the dispersive

waves and the breathers. Because  $\int \kappa^2 d\tilde{s}$  is a positive quantity we expect,

$$\left(\int \kappa^2 d\tilde{s}\right)_{initial} \geq \left(\int \kappa^2 d\tilde{s}\right)_{breather} \quad (3.5)$$

where the equality holds only if there are no dispersive waves. Although the breather and the initial condition have the same amount of total curvature (zero), this inequality shows that the distribution of curvature must change. Because the integrand is  $\kappa^2$ , most of the contribution to this integral comes from regions of the path where the curvature is the highest. Because of the dispersion of curvature, we might expect that the initial peaks of large curvature will get spread out over a larger region of the path, as the breather forms, causing  $\int \kappa^2 ds$  to be less for the breather. We will see that this “spreading” of the curvature distribution hinders ring-formation in a single lobe.

### 3.3 Thin Lobes

The simplest lobe is the thin lobe which has a center peak of curvature. We will consider symmetric piecewise constant curvature lobes, for which

$$u = \begin{cases} u_1 & L_0 < x < L_1 \\ u_2 & L_1 < x < L_2 \\ u_1 & L_2 < x < L_3 \end{cases} \quad (3.6)$$

where  $2u_1l_1 = -u_2l_2$ , and  $l_3 = l_1$  (Figure 3.1). The thin lobe may be described in terms of two parameters, its maximum angle,  $\Theta_0 = 2u_1l_1$  and  $l_1$ , the distance along the path to the first inflection point.  $l_2$ , the arclength of the center peak between the two inflection points, will be set to unity for the thin lobe.

As was the case for piecewise constant curvature steps, we solve Equations 2.19, 2.20 numerically, searching for the angles and arclengths at which  $\lambda = 0, \tan(\frac{\pi}{8})$  and 1. Figure 3.2 shows the division of parameter space. Lobes with small angles  $\Theta_0$ , and arclengths  $l_1$  that fall within the Region I will disperse, or gradually decay

with time. At larger angles the lobe that lies within Region II will form at least one single-valued breather solution.

As was the case for the wide step, and the asymmetric step, when at least one of the curvature regions is long, with small curvature, secondary single-valued breathers can form. Figure 3.3 indicates which lobes form more than 1 breather. Each solid line denotes the minimum angle at which a breather begins to form. The line furthest to the left on the parameter plane is the smallest angle for breather formation. It is the boundary between region I and II of Figure 3.2. The numbers in Figure 3.3 denote the number of breathers that will form. While multiple breathers can form, at most one of them is multi-valued.

For the very short, squat lobes, ( $l_1 \rightarrow 0$ ) the largest breather can form when  $\Theta_0 = \frac{\pi}{2}$ , but as the lobe elongates, it can be single-valued ( $\Theta_0 < \frac{\pi}{2}$ ), and still able to form a breather. Figure 3.2 indicates that the minimum angle for breather formation occurs at  $\Theta_0 = 1.15$  and  $l_1 = 2.72$ . At larger values of  $l_2$ , the critical angle increases back to  $\frac{\pi}{2}$ .

A single multi-valued breather forms from the lobes in region III of Figure 3.2. The minimum angle at which lobes form multi-valued breathers rapidly decreases from  $\pi$ , as  $l_1$  increases from 0. When  $l_1 \geq 6$ , the angle for multi-valued breathers increases. These lobes, with large  $l_1$ , have most of their curvature concentrated in the small center region.

Figure 3.4 shows a lobe that lies in this region with its breather. Because the side flanks are long compared to the center of the lobe, there is a strong peak in curvature at the center. This center region makes the largest contribution to  $\int \kappa^2 d\tilde{s}$ , so as the breather forms, and this quantity gets spread out among the breather and the dispersive waves, we might expect the strong center peak of curvature to get spread out. The original lobe has  $l_1 = 3$ , and  $\Theta_o = 1.8$  so  $\int \kappa^2 d\tilde{s} = 15.12$ . The breather has  $\alpha = 0.57$ , and  $\lambda = 0.53$ , with  $\int \kappa^2 d\tilde{s} = 9.67$ . As the lobe evolves, the center region with rapidly changing curvature is dispersed, which widens and shortens the lobe.

The most striking feature of Figure 3.2 is the absence of any significant ring-

forming region, although the line at which  $\lambda = 1$  is indicated on the parameter plot. For squat lobes, with small  $l_1$ , the thin lobe is narrow enough so that it is self-intersecting at angles smaller than the critical angle for ring formation. So squat lobes can not form rings. As  $l_1$  increases the minimum angle for ring formation decreases faster than the self-intersecting line, so when  $l_1 \geq 4.4$  physically possible lobes may form rings. The largest neck width for these lobes that may form closed breathers is 1 % of the lobe's amplitude, so small that the thin lobe is essentially pinched together before the evolution can take place.

We also consider smooth, thin lobes, for which

$$\Theta = -\frac{\Theta_0}{S(r)} \text{sech}(ks) \tanh(rks). \quad (3.7)$$

Increasing  $r$  forces the inflection point closer to the peak of the lobe.  $S(r)$ , is just  $|\text{sech}(s) \tanh(rs)|_{max}$  a shape parameter that normalizes the curve so that it has a maximum angle of  $\Theta_0$ . These lobes are similar to the tall, thin piecewise constant curvature lobes with  $l_2 \geq 7$ , although slightly thinner. Because of the similarity of solutions  $k$  simply sets an overall size, and time scale for the final solutions, but does not affect the shape of the breather that is formed.

The eigenvalues for these lobes were calculated numerically as they were for the smooth steps. A single pair of discrete eigenvalues was found, indicating that one breather may form, as for the piecewise constant curvature thin lobes. As the inflection point gets closer to the peak of the lobe, the critical angle for multi-valued breather formation increases slightly, while the critical angle for ring-formation decreases, consistent with the piecewise constant curvature lobes (Figure 3.5). Paths with  $r = 2$  form rings when  $\Theta_0 = 1.98$ . Paths with  $r = 1$  form rings when  $\Theta_0 = 2.03$ , but since the smooth lobes have smaller neck-widths than piecewise constant curvature lobes with the same amplitude and angle, the initial lobe is self-intersecting at an angle smaller than this critical angle for ring-formation.

A lobe with  $\Theta_0 = 1.8$ ,  $r = 1$  and  $k = 2.0$  is used in the numerical solution to the path equation (Figure 3.6). The scattering predicts a breather with  $\alpha = 1.12$ ,

and  $\lambda = 0.62$ , with an oscillation time of 0.20. This breather will be multi-valued but not ring-forming. At early times, ( $t = 0.0156$ ,  $t = 0.0312$ ), the upstream face of the lobe has flattened, while the downstream face has steepened, pushing a trough to the southwest. At later times ( $t = 0.078$ ,  $t = 0.094$ ), the trough has moved to the east, while the upstream face continues to flatten. This process widens the lobe, forming a breather.

In order to better compare the numerical solution to the expected breather, we compare the time series of the maximum amplitude of the meander  $|Y|_{max}$ , and the maximum curvature for the numerical solution, and its associated breather. Figure 3.7a gives the maximum value of  $|Y|$ , as a function of  $t$ . Within the first oscillation period, the amplitude rapidly decays to 0.58, or 40% of its original value. As the meander fluctuates, the amplitude fluctuates, reaching a secondary maximum at one oscillation period, however this amplitude is less than half of the original amplitude, indicating the lobe decays as it evolves, rather than elongating. As time passes the meander fluctuates with a period of  $T = 0.20$ . Figure 3.7b shows the maximum amplitude of the breather expected from the Inverse Scattering. The breather fluctuates in amplitude every period but always reaches the same maximum amplitude. The numerical solution has approximately the same amplitude as the breather, (the average maximum amplitude for the breather is 0.7, while the average maximum for the numerical solution, after the initial decay, is 0.71). and the amplitude varies at the same period as the breather. However, the numerical solution also appears to have a slow variation in  $|Y|_{max}$ , with a period of  $T = 0.63$ . The breather itself does not have significant energy at this period. The breather and the numerical solution also slowly get out of phase, so that by the end of the time series the phase difference between the two series is shifted approximately  $80^\circ$  from the beginning of the time series.

Figure 3.8a indicates how the maximum curvature of the numerical solution evolves with time. There is an initial decay in curvature during the first oscillation cycle, and then the curvature fluctuates, with a mean value of 5.2, which is the same average maximum curvature of the breather (Figure 3.8b). The curvature for the

numerical solution is also slowly-varying, with maxima in amplitude corresponding to maxima in the curvature.

Figure 3.9 shows the time evolution for the lobe with  $\Theta_0 = 2.0$ ,  $r = 1$ , and  $k = 2.0$ . Inverse Scattering predicts that a breather will form with  $\alpha = 0.98$ , and  $\lambda = 0.93$ . This lobe has a neck-width of 0.001 at  $t = 0.0$ . With such a narrow neck, the path should be considered closed because other physical processes are dominant at this wavelength. However, this evolution demonstrates how the dispersion of curvature hinders ring formation in the simple lobe. As the lobe evolves, the neck steadily widens (see e.g.  $t = 0.06$ ), and we see that the single lobe actually pulls itself apart, rather than closing. After approximately half of an oscillation cycle ( $t = 0.12$ ), the lobe has switched direction, and has a visibly wider neck width. After a full oscillation cycle ( $t = 0.24$ ), the neck width has narrowed again, and is nearly closed, but it is still wider than the original lobe.

The initial curvature decays from its peak value (Figure 3.10), and then oscillates around a mean of 6.58, while the breather has a mean curvature of 6.56. Figure 3.11 shows the time series of the maximum amplitude. Within the first oscillation period, the maximum amplitude decays to a small secondary maximum (at  $t = 0.12$ ), and then reaches another, larger maximum at  $t = 0.23$ , (one oscillation period). The maximum amplitude then fluctuates about a mean of 0.75. The evolution of the maximum amplitude for the breather also fluctuates about this mean of 0.75. As for the previous lobe, the maximum amplitude of the numerical meander is slowly-varying, while the amplitude for the breather is not. The amplitude of the numerical solution can increase beyond that of the breather, but it does not grow indefinitely, and there is no other indication of an instability process. Instead it appears that the initial condition evolves into a structure that is close to the breather, but is still being affected by the surrounding dispersive wavetrain.

### 3.4 Wide Lobes

We next turn to lobes with a wider neck-width, to see if a single symmetric lobe can ever form rings with a physically possible initial condition. It is possible that the short, squat lobes are able to redistribute their two curvature peaks and form a closed loop, if they start out more widely spaced. For piecewise constant curvature, this width will be approximated by adding a line with zero curvature in the center. The lobe then has curvature

$$u = \begin{cases} u_1, L_0 < x < L_1 \\ u_2, L_1 < x < L_2 \\ 0, L_2 < x < L_3 \\ u_2, L_3 < x < L_4 \\ u_1, L_4 < x < L_5 \end{cases} \quad (3.8)$$

The lobe is again symmetric, with  $2u_1l_1 = -2u_2l_2$ , so the lobe can be parameterized in terms of  $l_1$ ,  $\Theta_0$  (or  $2u_2l_2$ ), and  $l_3$ , the length of the center section.  $l_2$  is chosen to be unity. As  $l_3$  increases beyond  $l_1$ , the lobe resembles two separated steps, and we expect that at large separations, breathers may form. Because there are three parameters, we will need a series of parameter space plots to see how they affect the shapes of the breathers. We construct plots of the parameter plane  $(\Theta_0, l_1)$ , with four different values of center width ( $l_3 = 0, 1, 2, 5$ ) in Figure 3.12. Figure 3.12a shows the parameter plane for lobes with  $l_3 = 0$ . This figure is the same as Figure 3.2, except that the ordinate is compressed because  $l_2$  is the length of only one of the negative curvature regions.

The line indicating single-valued breathers is not included, in any of the four parameter planes. Breathers always form with  $\Theta_0 \approx \frac{\pi}{2}$ . As  $l_3$  increases, the straight line region increases, separating the potential wells, and creating a zone where several single-valued breathers form as the resonant harmonics to the scattering problem. Because these breathers are hard to distinguish from the dispersive waves, they are not indicated in the plots, and region I denotes dispersive lobes, and lobes that form

only single-valued breathers.

Tall lobes, with  $l_1 \geq 1$ , are unaffected by the addition of a short center region, and still form one multi-valued meander for lobes with maximum angles of  $\Theta_0 \approx 2$  (region II of Figure 3.12b). This maximum angle increases to 2.7, as the separation  $l_3$  increases beyond 2 (Figure 3.12c,d). The squat lobes, with  $l_1 \leq 1$ , also form one multi-valued breather, in region III, for angles near  $\Theta = \pi$ . Lobes with  $l_1 \ll l_3$  look like two widely separated asymmetric steps. Like the very asymmetric step, they are unable to form multi-valued meanders, except at lobe angles greater than  $\pi$ .

At larger angles, two multi-valued breathers can form (region IV). When  $l_3 = 1$ , the minimum angle for two multi-valued breathers to form is  $\Theta = 2.8$ . As  $l_3$  increases, this angle must increase, and is near  $\pi$ , when  $l_3 = 5$ . As the separation  $l_3$  increases, the size of region IV increases, because  $l_3 > l_1$  for more of parameter space, and the lobe behaves more like two asymmetric steps.

When the lobe is very steep, with maximum angles greater than 4, two different rings can form, in region V. These lobes always have  $l_1 < l_3$ , so the two closed breathers arise because the lobe is evolving as two steps. The minimum angle at which these rings form is the same as the corresponding asymmetric step. For example, when  $l_3 = 1$ , or  $l_3 = 5$ , two breathers form with  $\Theta = 4.1$  and  $l_1 = 0.5$ . These closed breathers both have the same  $\alpha = 1.3$ , which is the same wavenumber as the breather associated with the step with asymmetry 0.5.

The parameter space plots have shown that it is possible for two multi-valued breathers to form, but have shown nothing about the relative sizes of those breathers. The shape and size of the breather is determined by the location of the associated zero in the complex plane. Figure 3.13 shows how the position of the two zeros changes in the complex plane as a lobe gets wider. Recalling that  $\lambda$  determines the steepness of the breather, the plane is divided into dispersive solutions (region I), single-valued breather solutions (region II), multi-valued breather solutions (region III), and ring-forming solutions (region IV), depending on the location of the zero.  $\alpha$  is a scaled wavenumber, so breathers with large  $\alpha$  will be small and fast.

For this figure, the lobes all have angle,  $\Theta_0 = 3.5$ , and fixed side length  $l_1 = 1$ . The center spacing  $l_3$  varies between 0 and 5. When  $l_3 = 0$ , the zeros are located at the edges of the spiral (Figure 3.13). The large, slow breather lies within region IV, while the small fast breather lies within region II. (Recall from Figure 3.2, that this lobe, with no center, would be self-intersecting.) As the center span increases, the zeros spiral towards each other. The small meander gets steeper and larger, and the large meander gets less steep, and smaller; both become multi-valued, but not ring-forming. When the center span is as large as the breathers themselves, the two faces of the lobe are able to act independently. The two zeros are indistinguishable, and located at the same point as a symmetric step with  $\Theta_0 = 3.5$ .

A wide piecewise constant curvature lobe can form a closed loop, but only if the lobe is wide enough so that the two faces of the lobe act as two independent steps, so two rings are formed. At smaller angles, the wide lobe can produce two breathers. When the width is smaller than the sides of the lobe, then one of the breathers is large and steep, and the other is small and single-valued. Because the single-valued one is small, we expect it to propagate faster than the steeper, larger breather. As the width of the lobe increases, the two breathers begin to resemble each other.

These tendencies can be seen in smooth wide lobes, for which

$$\Theta = \Theta_0(\operatorname{sech}(s) - \operatorname{sech}(s + W)) \quad (3.9)$$

With the wide lobes, a larger domain is needed to solve the eigenvalue problem than can be created. Without solving the scattering problem for the smooth wide lobes, we can compare the numerical evolution of initial lobes with the tendencies predicted for the much simpler piecewise constant curvature lobes.

Figure 3.14 shows the numerical solution for  $\Theta_0 = 3.5$ , and  $W = 10$ . The smaller steeper breather forms quickly, while a broad slower meander lags behind. At  $t = 0.1$ , it appears that the smaller breather is about to pinch off, but at  $t = 0.22$ , it is much broader.

Figure 3.15 is the numerical solution for a very wide initial lobe, with  $\Theta = 3.5$ ,

and  $W = 20$ . With such a wide separation between the sides of the lobe, the initial condition looks like two steps, and two breathers with similar shapes, and propagation speeds are formed.

An initial wide lobe can form two distinguishable breathers, even when the separation is less than other length scales of the problem. While these wide lobes can form closed meanders, they only appear to do so when they are wide enough apart so that the lobe behaves as two steps.

### 3.5 Modifications of Single Lobes

We found that the dispersion of curvature made it difficult for a lobe to pinch together and form a single ring. It is possible that modifications of the single symmetric lobe may form closed loops. For example, the numerical solutions indicate that an asymmetric structure, perhaps like the meander in Figure 3.9 at  $t = 0.06$ , will form a closed path, after a short time.

Another possible modification is the presence of a second meander. Figure 3.16 shows a two lobe structure. The upstream lobe has

$$\Theta = -1.5 \operatorname{sech}(2s) \operatorname{tanh}(2s) \quad (3.10)$$

and the downstream lobe has the same shape as the lobe in Figure 3.6, with

$$\Theta = 1.8 \operatorname{sech}(2s) \operatorname{tanh}(2s) \quad (3.11)$$

This shape produces two breathers, the second slower breather is the steeper one, although both are multi-valued. The steep breather does not appear to be significantly steeper than the breather formed in Figure 3.6, implying that the presence of a meander of the opposite sign does not enhance ring formation. The faster breather interacts with the steeper breather in the early stages of evolution ( $t = 0.02, 0.04$ ) but the two do not form a pinched ring.

If the upstream lobe has the same sign as the downstream lobe (Figure 3.17), then the structure still appears to form two breathers but the leading breather is single-valued and the trailing breather is steeper than the breathers in Figure 3.16. The steeper breather does pinch off at  $t = 0.16$ . The second lobe of the same sign as the original lobe does allow the curvature to redistribute to form a closed path.

### 3.6 Conclusions

The inverse scattering method predicts that a breather will emerge from some initial conditions after enough time has passed for the dispersive waves to pass away. In the section on the thin lobes, it appears that the initial conditions quickly evolve into solutions with the same periods, and average amplitudes and curvature maxima as the breather. Although the dominant feature of the numerical solution appears to be the breather, the numerical solutions also indicate that the breather is modified, perhaps by interaction with the dispersive waves. Even with this interaction, the numerical solution does not appear to drift away from the breather. Instead, the breather appears to be a stable, oscillating meander, that the numerical solution appears to resemble.

The tall thin lobes have high curvature in their center region, and smaller curvature to the sides. Most of the contribution to the integral  $\int \kappa^2 d\tilde{s}$  comes from the center region. Because of the integral constraints, the peak of the curvature must be reduced, and even a small reduction in the center curvature causes the tall, thin lobes to spread out, making it difficult for a closed breather to form. It appears that the only symmetric, thin lobes that can form rings are already essentially closed.

Short squat lobes with small  $l_1$ , have two regions of large curvature, separated by a long arc of small curvature. Geometrically, these lobes must intersect themselves before they have enough curvature to form closed rings. If the squat lobe is made wider, with the addition of a flat, center region, then two closed loops may form. These two rings form because the lobe has a center region larger than the size of the two faces of the lobe, so they evolve separately as two identical steps.

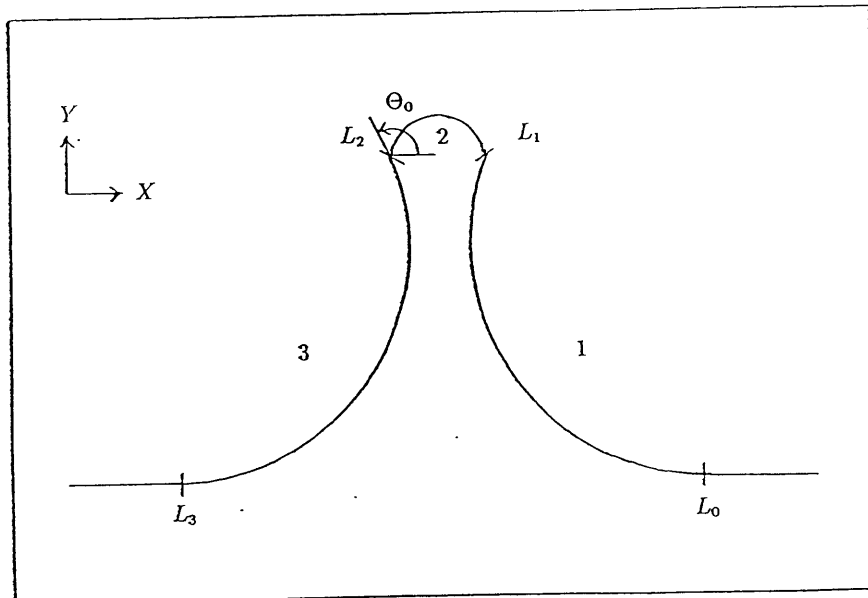
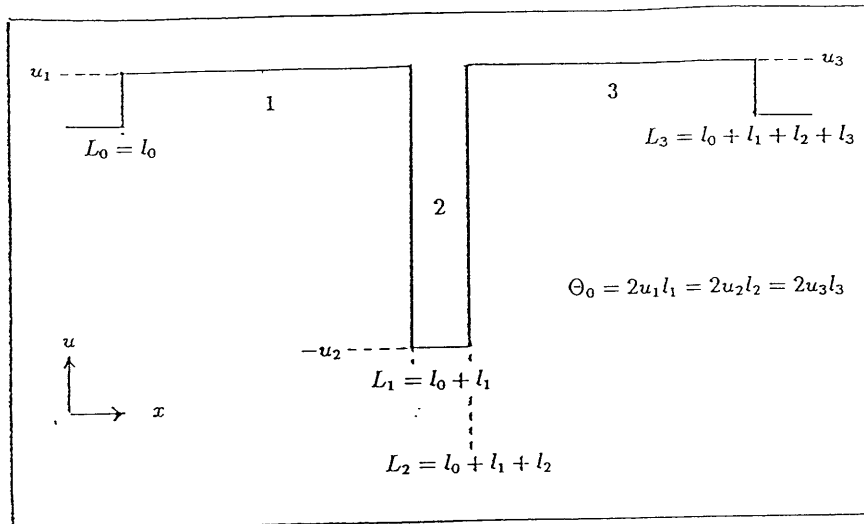


Figure 3-1: Three square well scattering problem for the lobe (a), and the associated path (b).

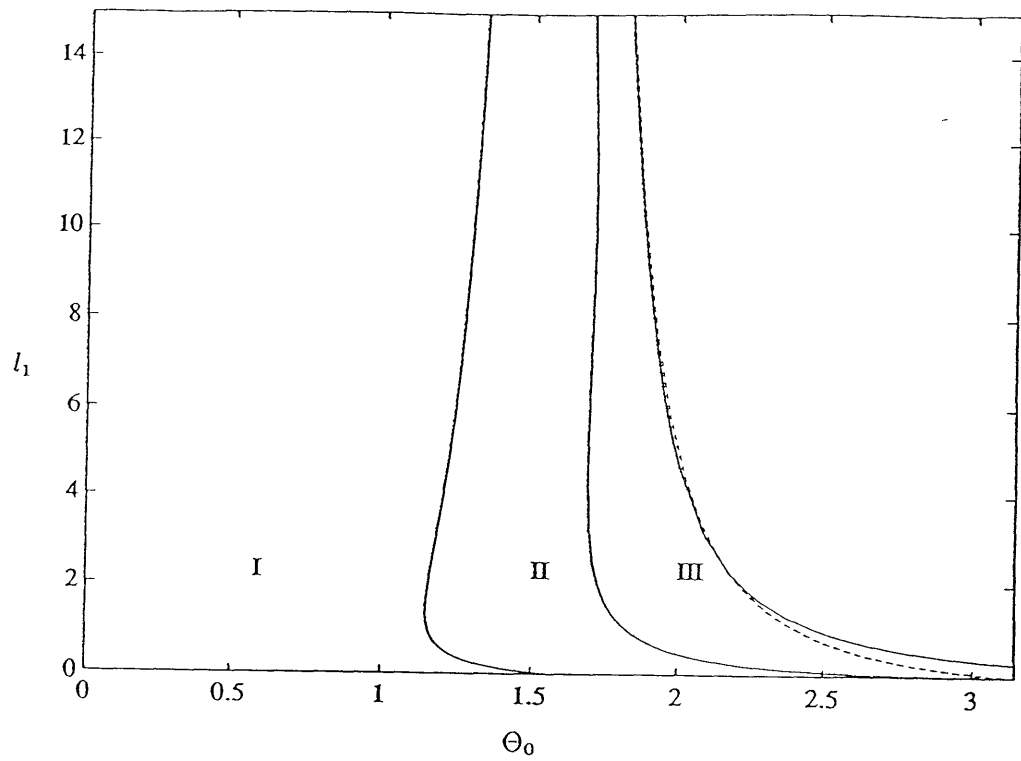


Figure 3-2: Parameter plane for thin lobes. Region I lobes disperse, region II lobes form single-valued breathers and region III lobes form multi-valued breathers. The region to the right of the dashed line indicates self-intersecting lobes.

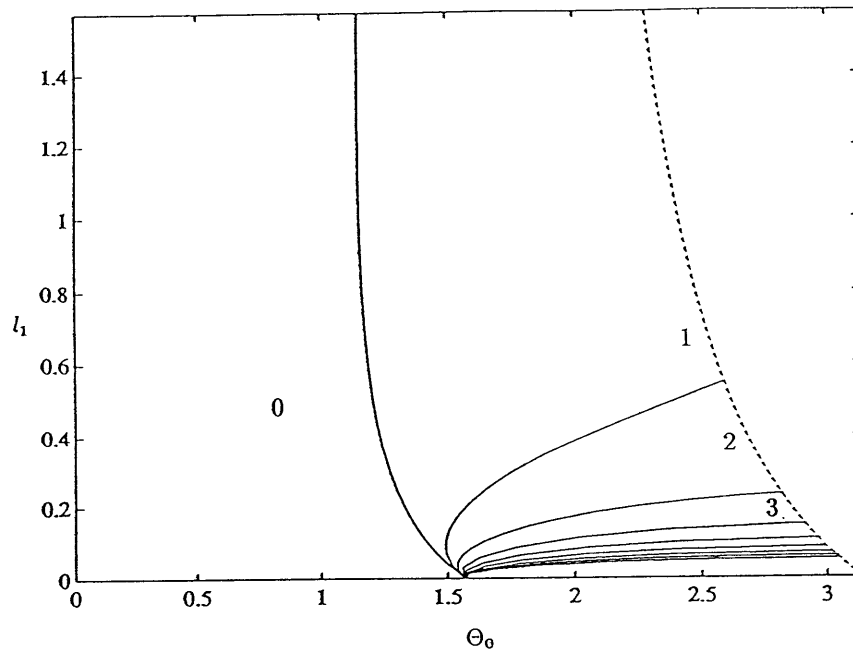
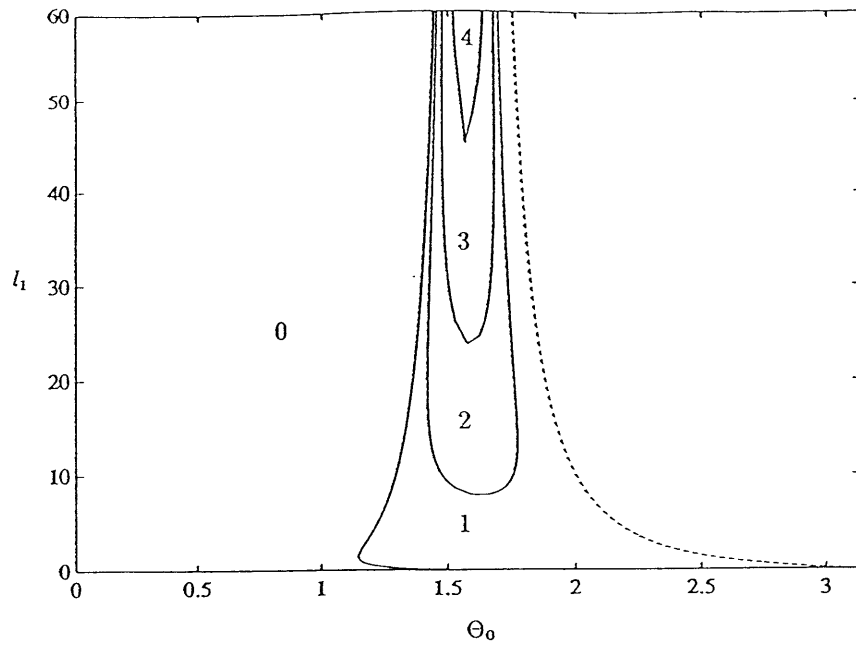


Figure 3-3: Parameter planes showing the multiple breathers for the tall, thin lobes (a), and the short thin lobes (b). The numbers indicate the number of breathers that form within each region. All breathers except the first will be single-valued.

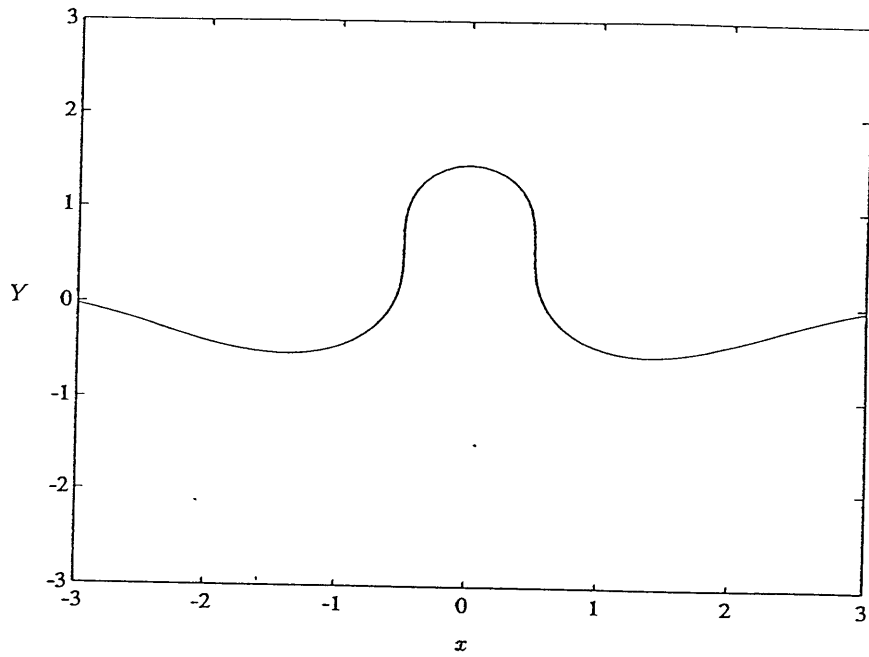
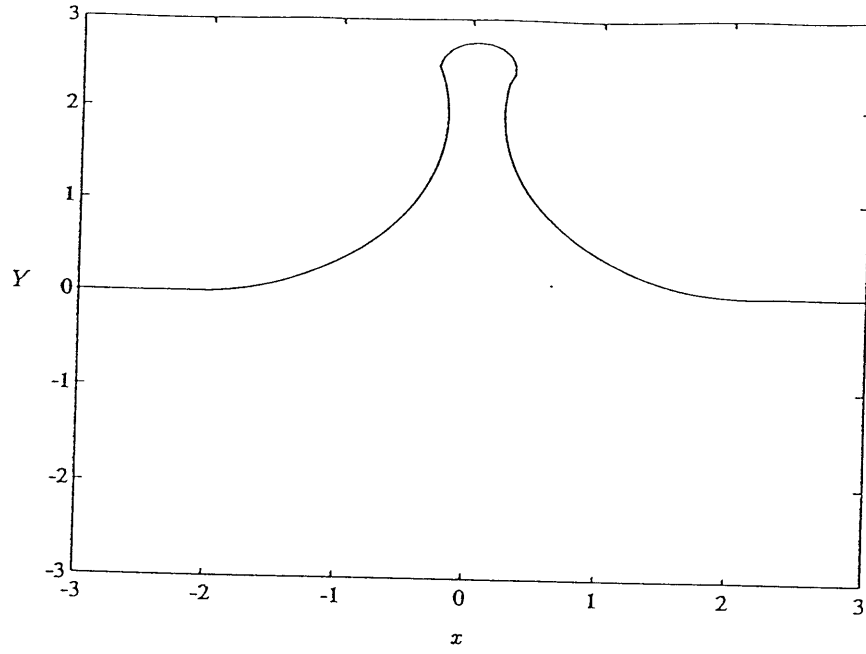


Figure 3-4: (a) Piecewise constant curvature lobe with  $\Theta_0 = 1.8$ ,  $l_1 = 3$ . (b) The breather associated with this lobe, with  $\alpha = 0.57$ , and  $\lambda = 0.53$  (b).

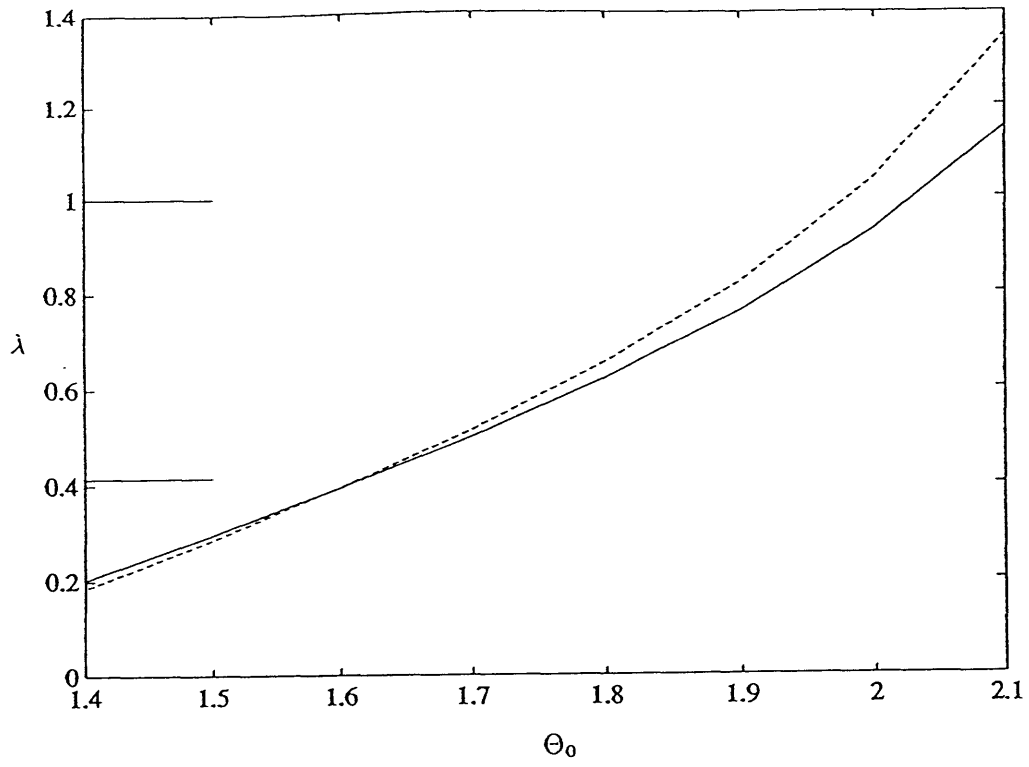


Figure 3-5: Steepness parameter  $\lambda$ , as a function of step angle for  $r = 1$  (solid line), and  $r = 2$  (dashed line).

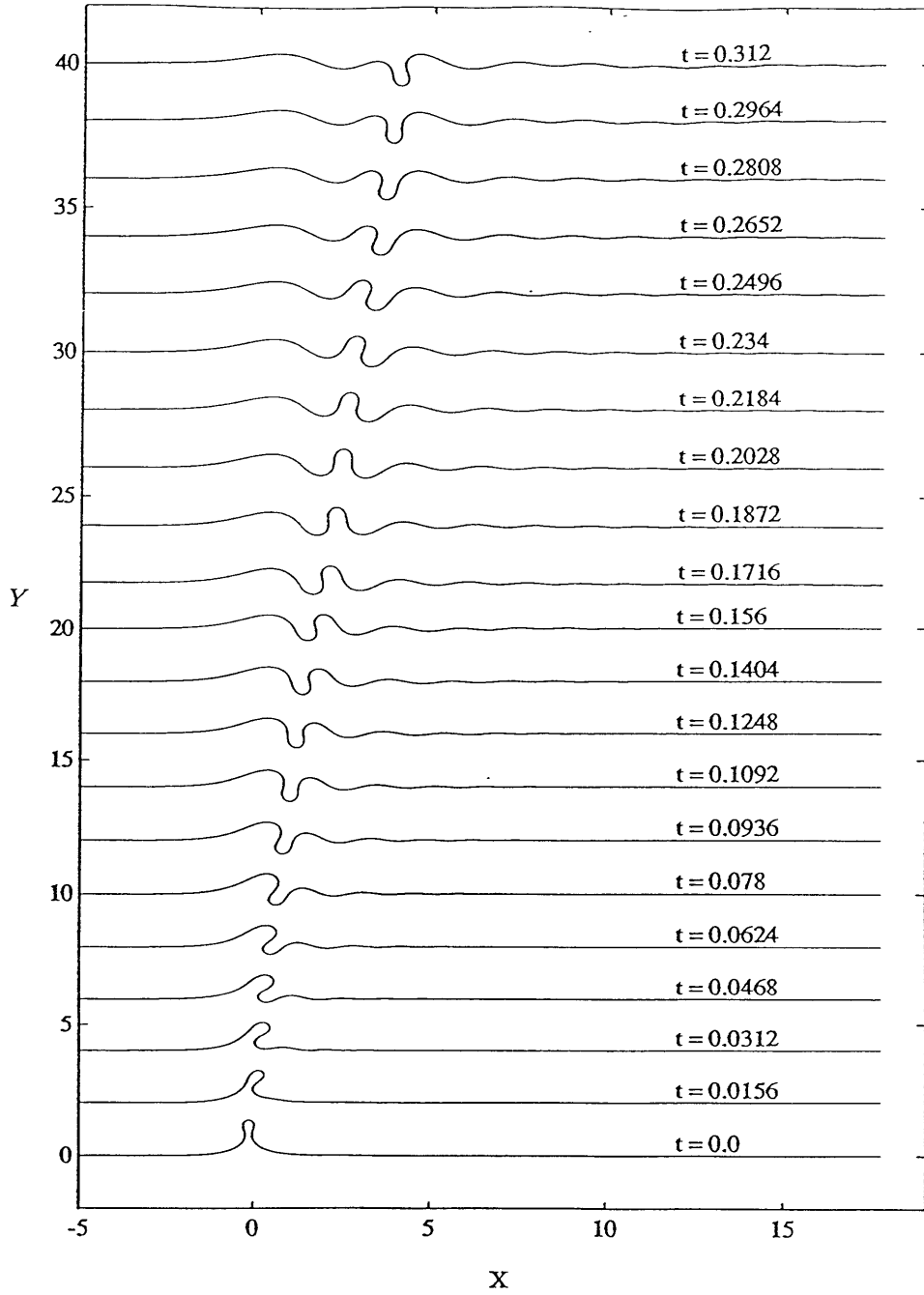


Figure 3-6: Numerical evolution for an initial thin lobe with  $\Theta = 1.8$ ,  $r = 1$ , and  $k = 2$ .

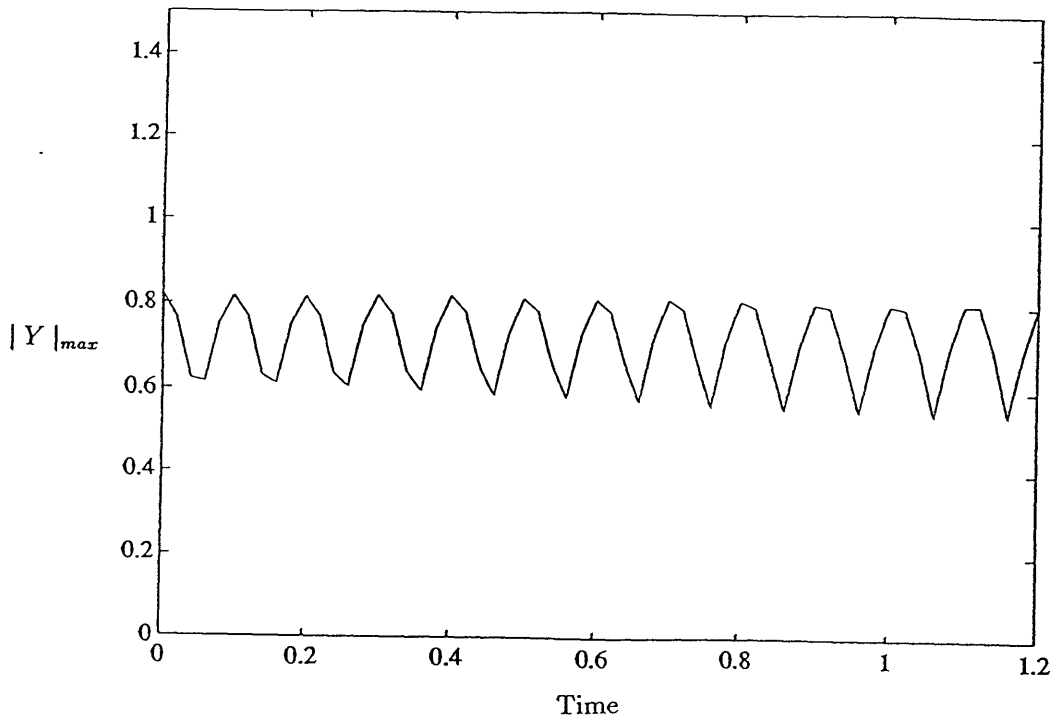
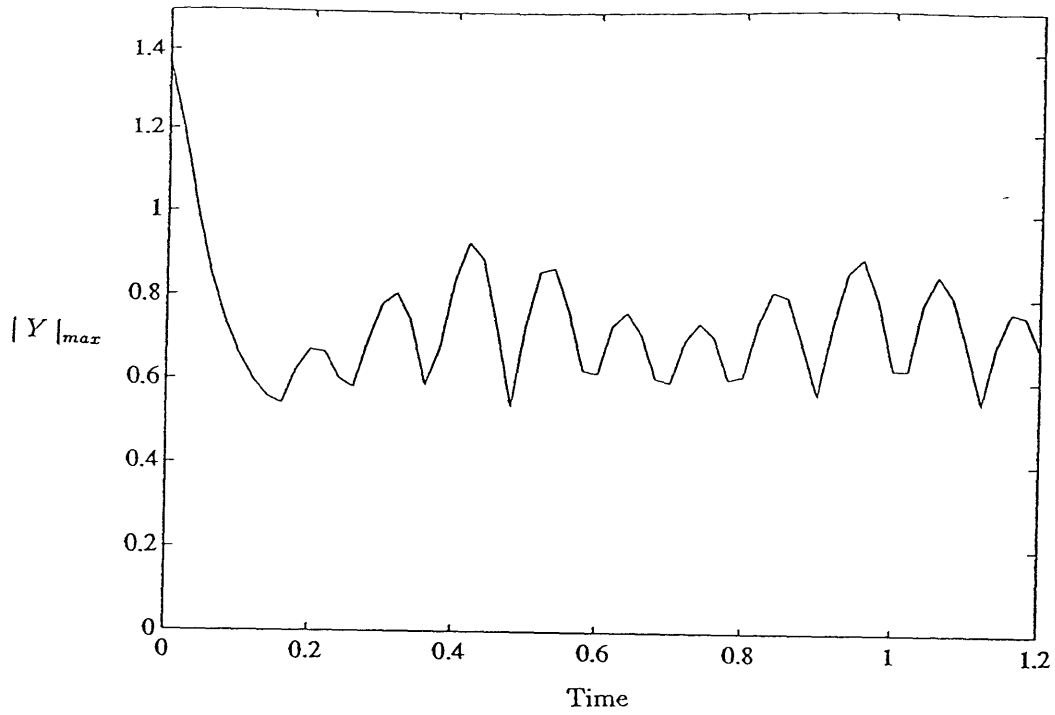


Figure 3-7: Maximum amplitude versus time for the numerical solution of Figure 3.6 (a), and the breather (b).

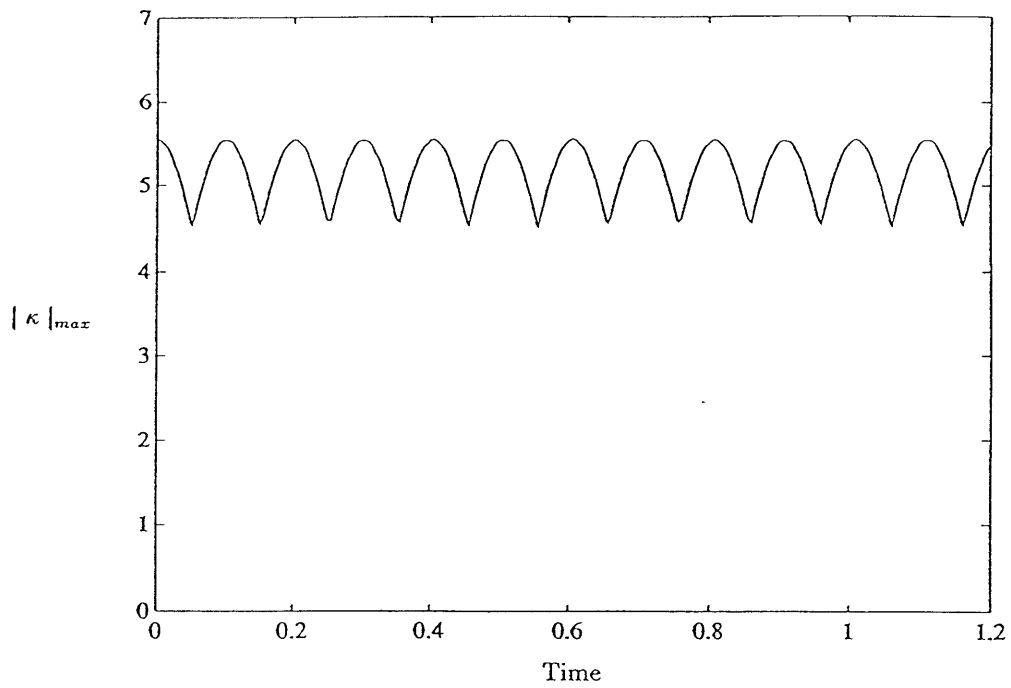
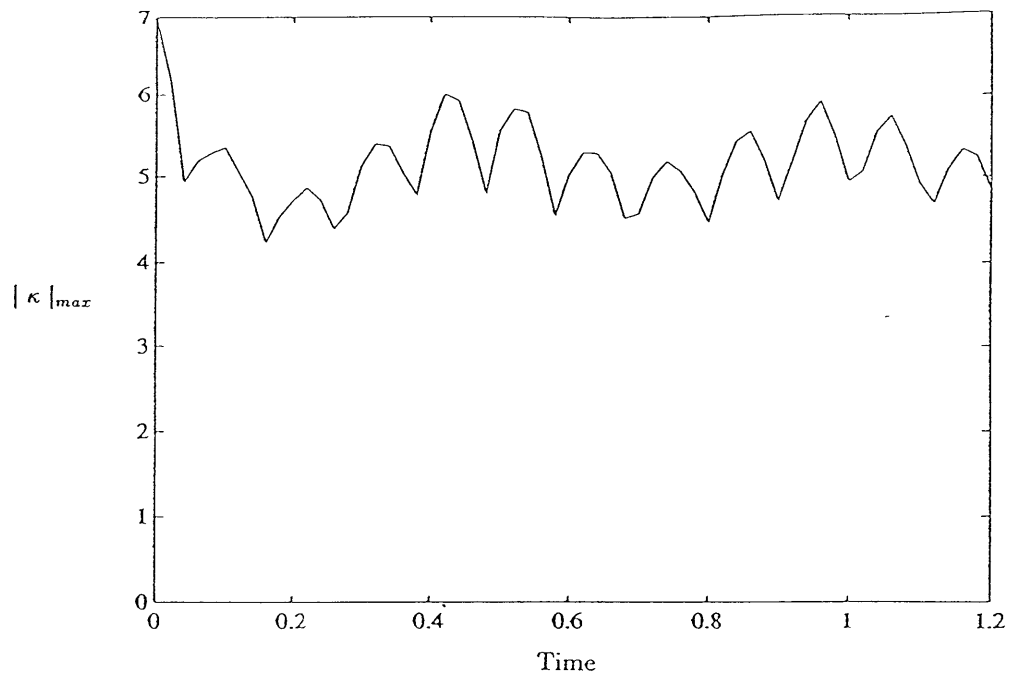


Figure 3-8: Maximum curvature versus time for the numerical solution of Figure 3.6 (a), and the breather (b).

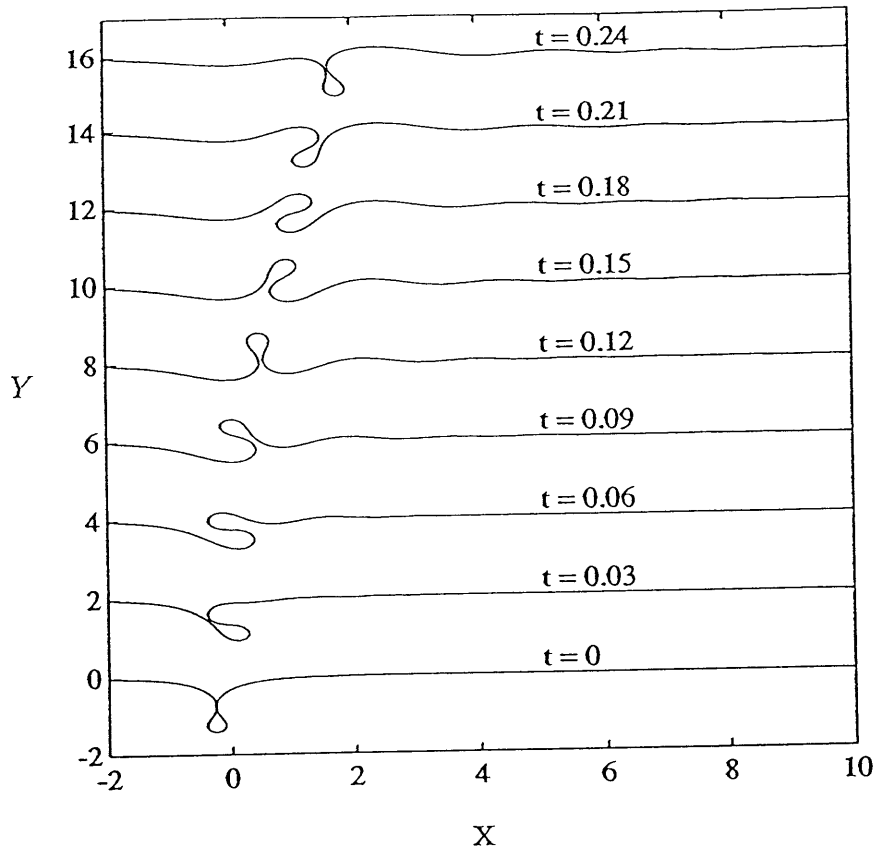


Figure 3-9: Numerical evolution for an initial thin lobe with  $\Theta = 2.0, r = 1, k = 2$ .

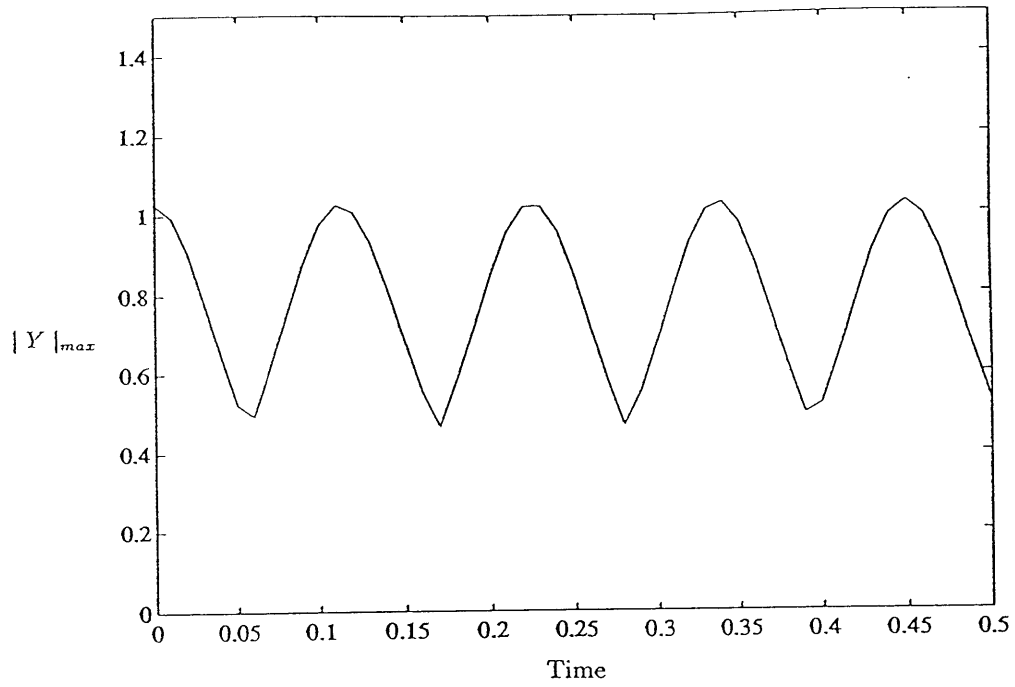
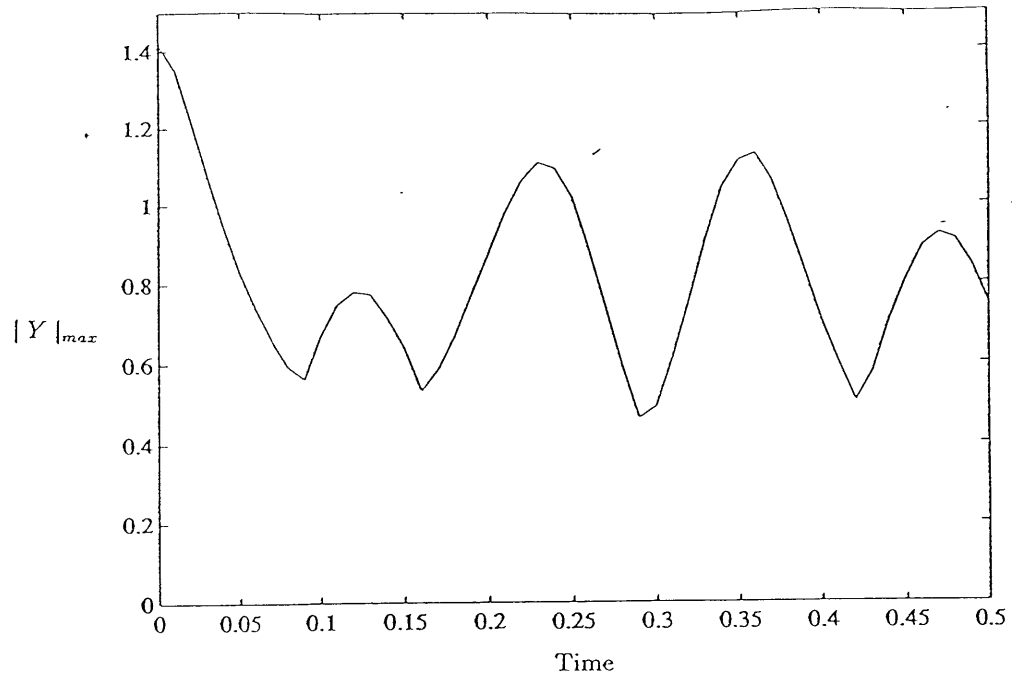


Figure 3-10: Maximum amplitude versus time for the numerical solution of Figure 3.9 (a) and the breather (b).

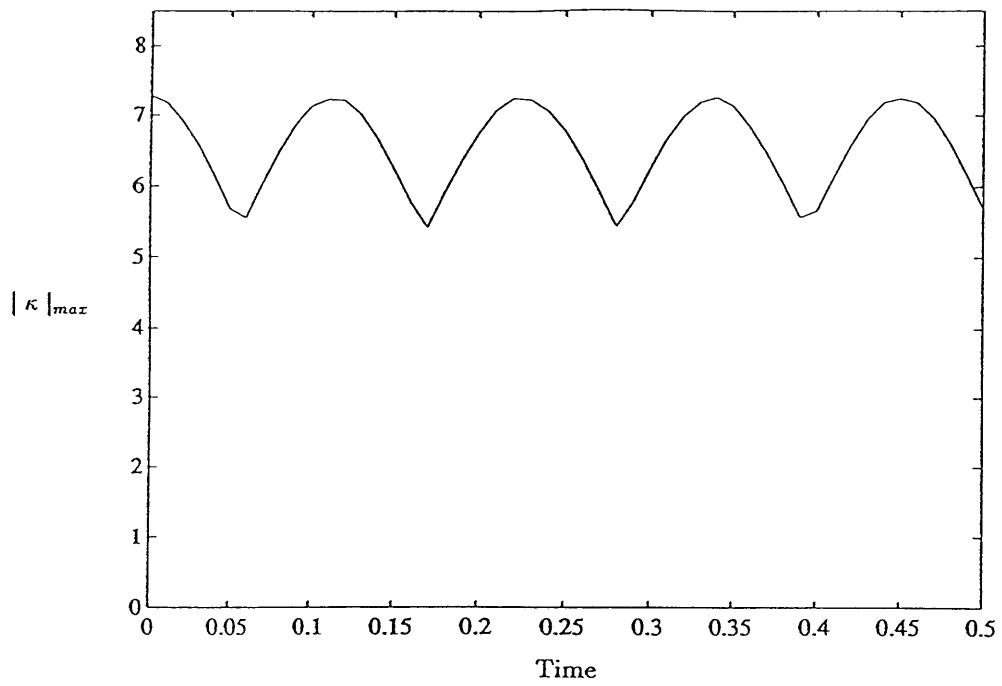
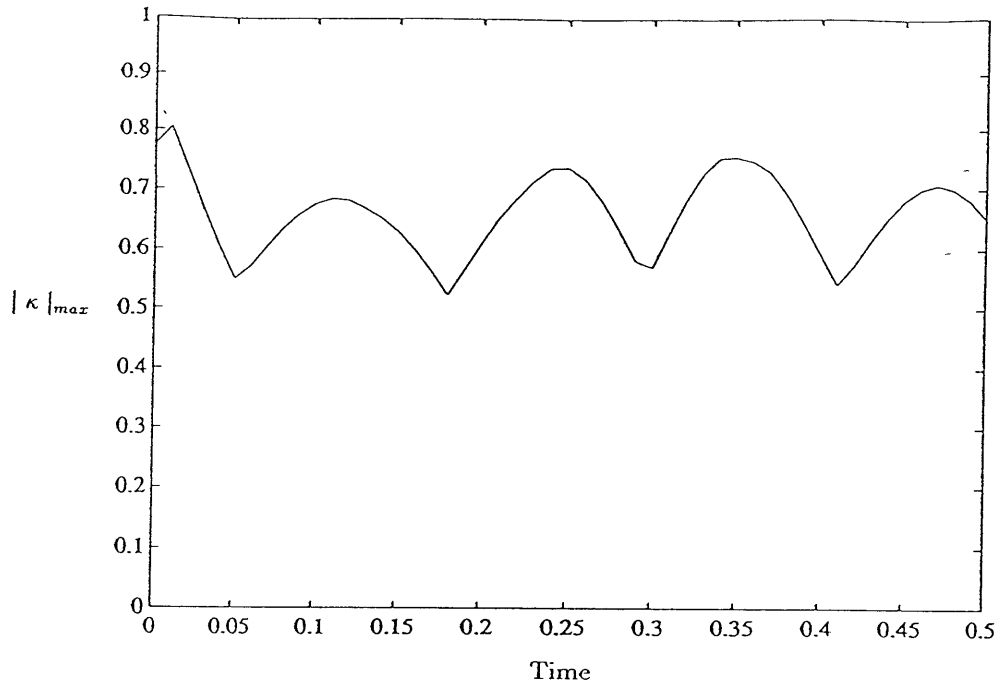


Figure 3-11: Maximum curvature versus time for the numerical solution of Figure 3.9 (a) and the breather (b).

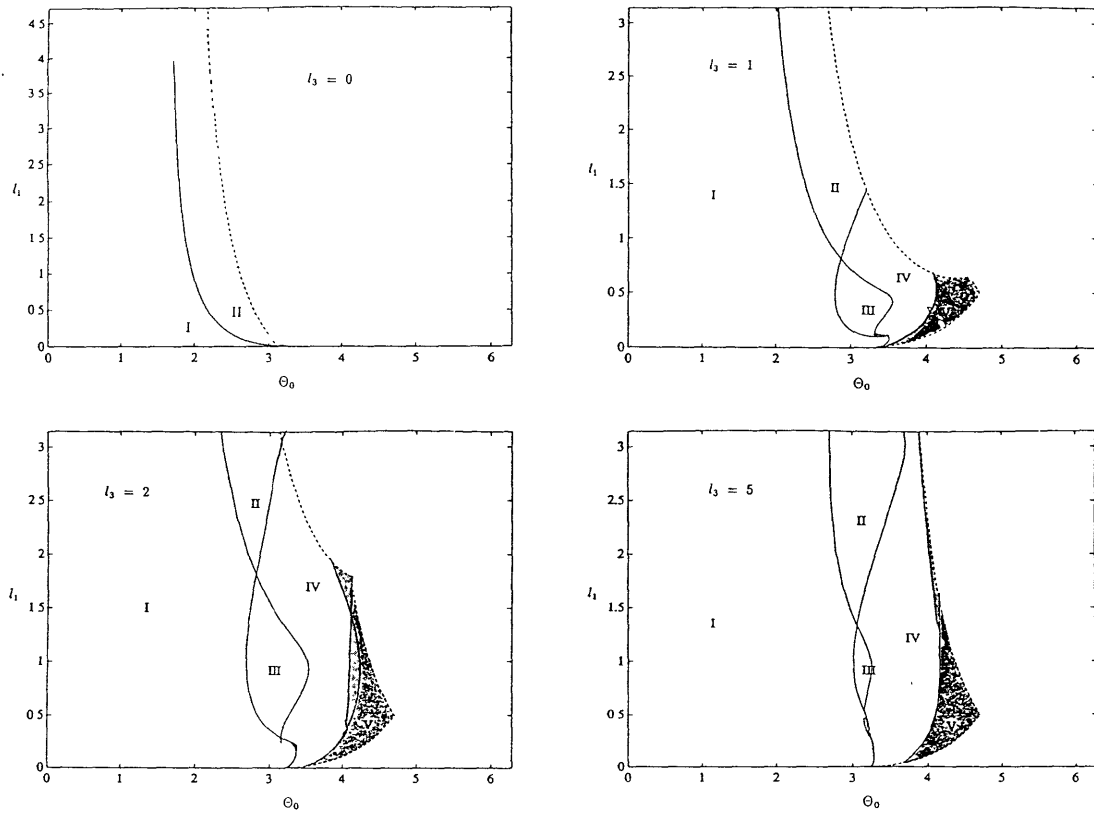


Figure 3-12: Parameter planes for the wide lobes with  $l_3 = 0, 1, 2, 5$ . Region I: dispersive and single-valued breather forming lobes. Regions II and III: lobes that form one multi-valued breather. Region IV (grey): lobes that form two multi-valued meanders. Region V (dark grey): lobes that form two rings.

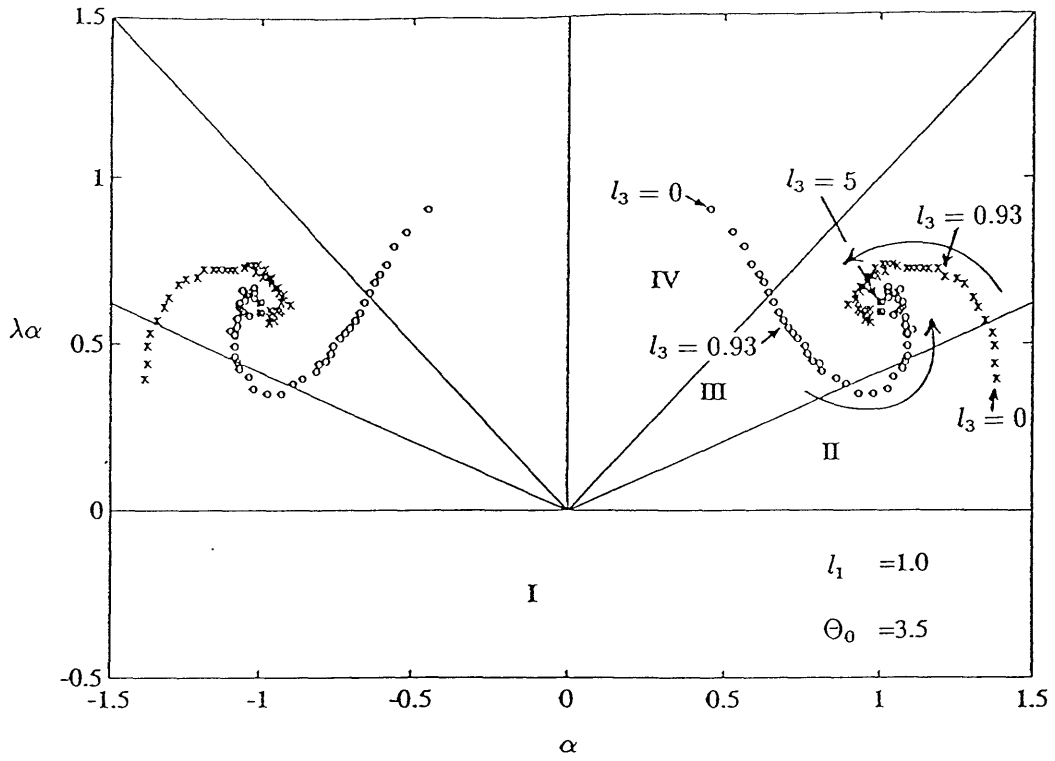


Figure 3-13: Location of the zeros in the complex plane, for the lobe with  $\Theta_0 = 3.5$ ,  $l_1 = l_2 = 1$ , and  $l_3$  ranging from 0 to 5.0. All the lobes with  $l_3 < 0.93$  intersect themselves and are unphysical.

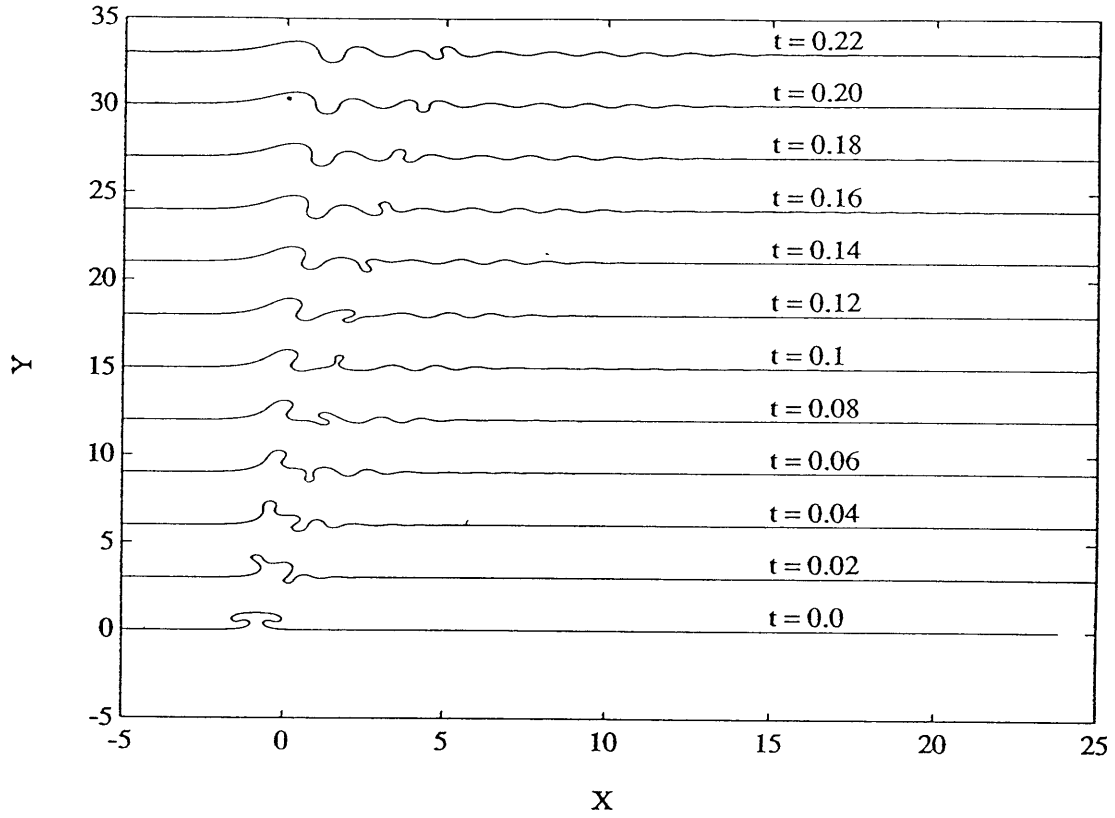


Figure 3-14: Numerical evolution for the wide step with  $\Theta_0 = 3.5$ , and  $W = 10$ . Note that the larger, slower breather lags behind a smaller steeper breather.

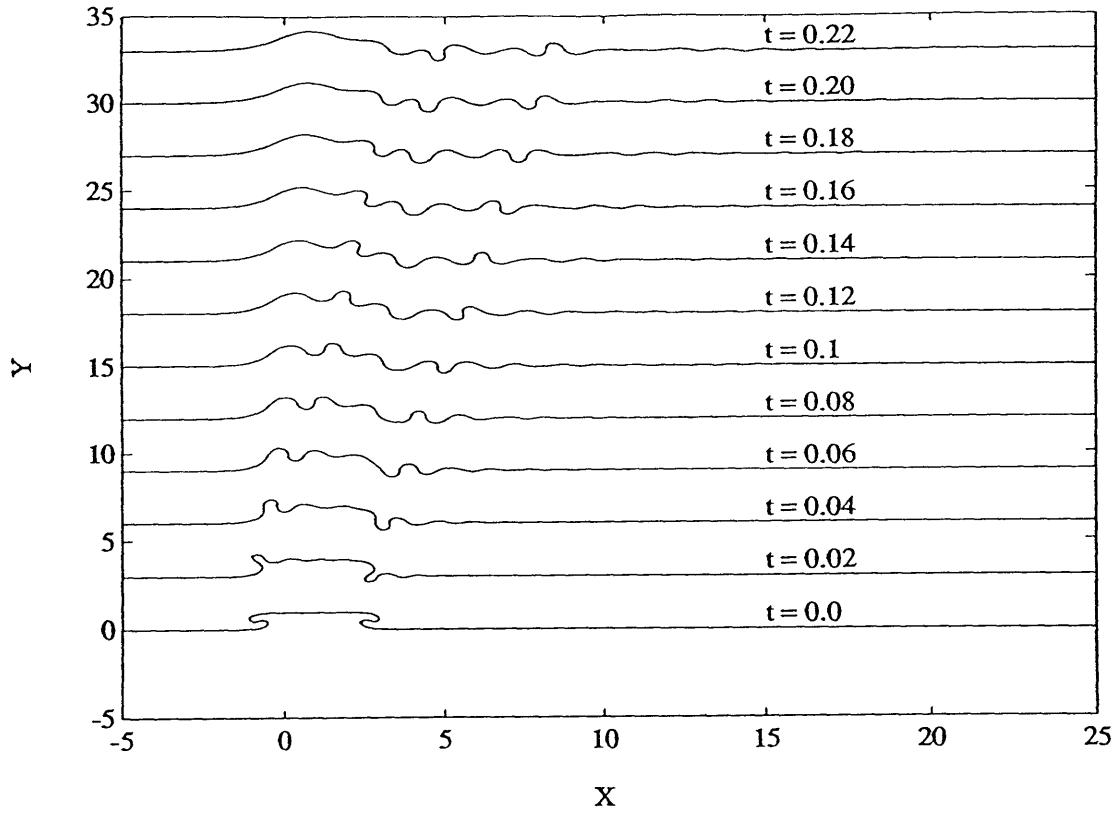


Figure 3-15: Numerical evolution for the wide step with  $\Theta_0 = 3.5$ , and  $W = 20$ . Essentially two identical breathers are formed because the initial condition resembles two steps.

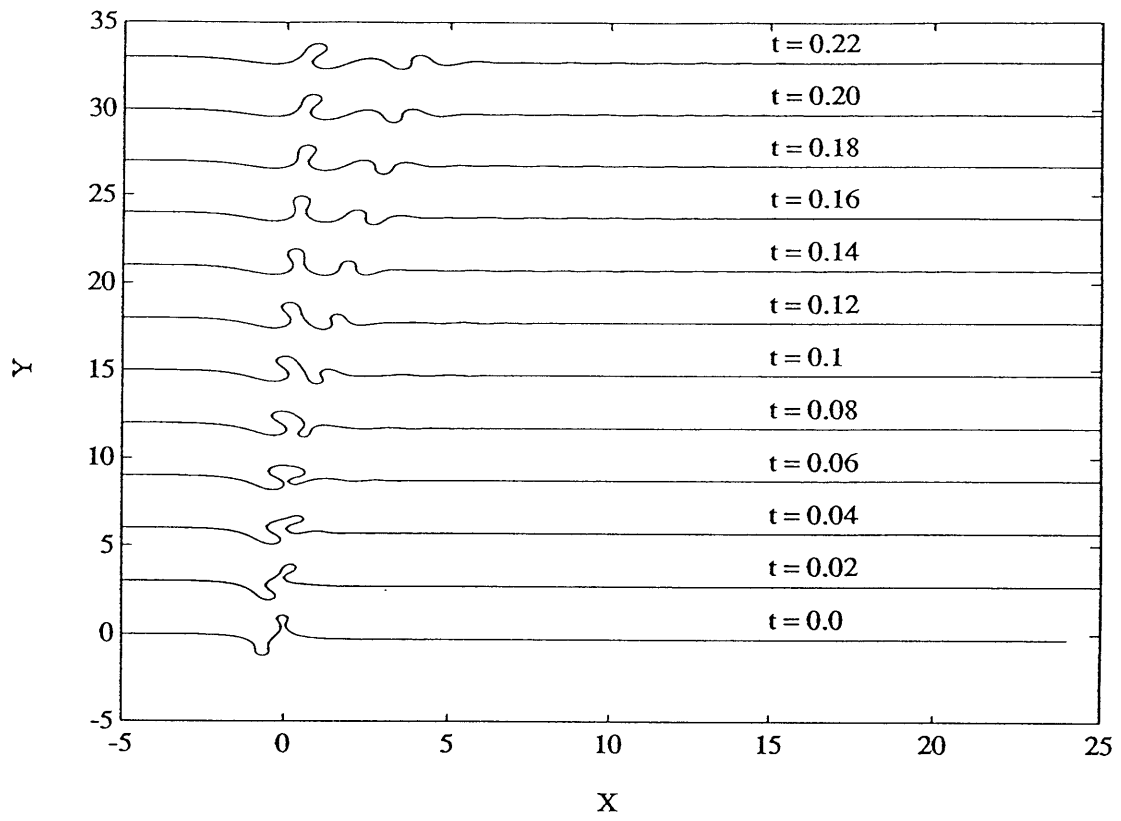


Figure 3-16: Numerical evolution for the two lobe structure, with opposite signs.

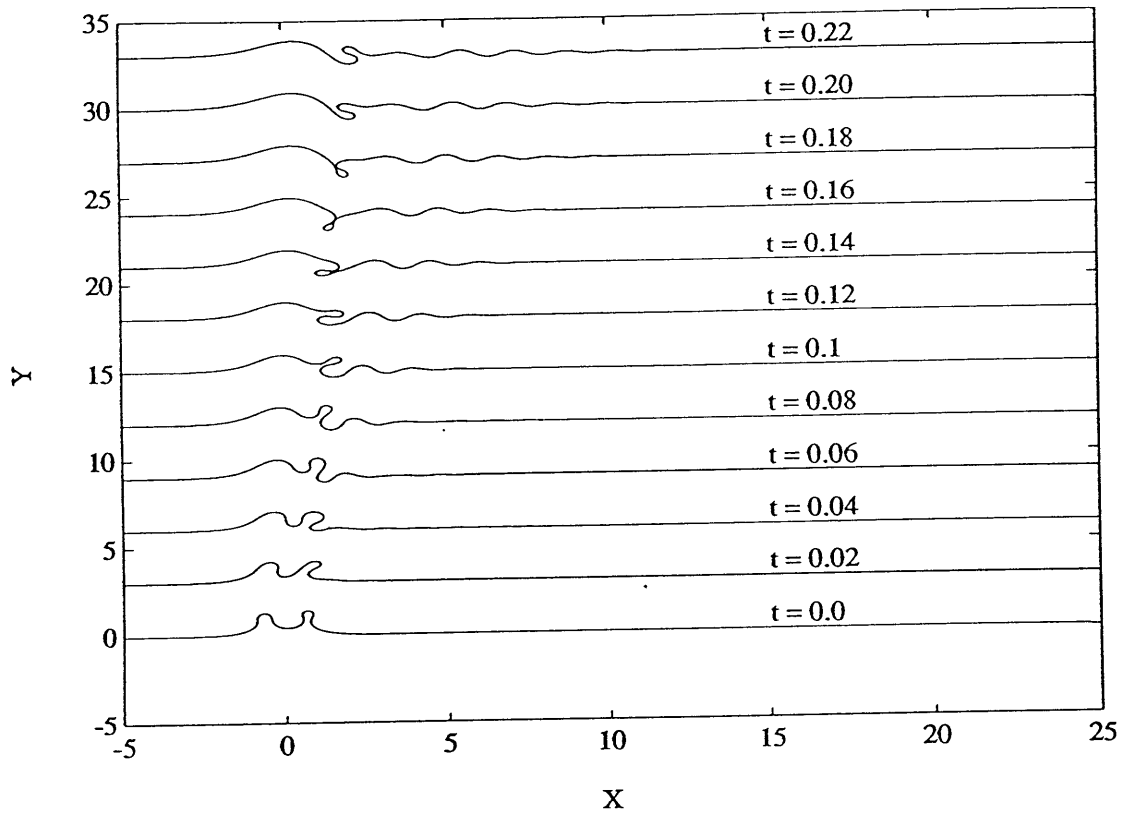


Figure 3-17: Numerical evolution for the two lobe structure, with same signs. Note the pinch off at  $t = 0.16$ .



# Chapter 4

## Conclusions

In this thesis we are concerned with predicting whether an initial meander will form a ring at some later time. In order to examine this problem we use a simple physical model to understand the physical mechanisms involved in the formation of a ring. The model used in the thesis is a  $1\frac{1}{2}$  layer thin jet model on the beta plane.

By assuming that the jet is thin, we are assuming that cross stream scales are much smaller than along stream scales. This limits the model to meanders which are much larger than a deformation radius. By making this approximation, the meandering motion of the front can be separated from the detailed structure of the jet. The Gulf Stream, and other meandering jets, have meanders with a wide variety of length scales so this model can only be used as a guide in understanding the mechanism of ring-formation due to long wavelength processes, and not as an accurate predictor of pinch-off events. Since we have assumed that  $\tilde{\beta} = O(1)$ , the thin jet assumption also implies that Rossby waves are unable to radiate away from the meandering jet.

By reducing the stratification to  $1\frac{1}{2}$  layers, a baroclinic current can be studied using a simple physical model. However, Meacham (1990) has recently shown that the absence of the barotropic mode causes order 1 differences in the finite amplitude solutions to initial value problems. With the barotropic mode, large-scale interactions (on the order of the barotropic deformation radius) between the jet and the

far field take place (Flierl and Robinson 1984). Thus the barotropic mode of the meanders must be matched to surrounding barotropic eddy field. If the barotropic mode is removed, as it was in section 1.2, then the interaction is reduced to a region within a deformation radius. Because of the smaller deformation radius, the  $1\frac{1}{2}$  layer meanders are much slower than barotropic ones. The motion of the jet is determined by the local shape of the path, and can be expressed as a differential equation (equation 1.30). Although the  $1\frac{1}{2}$  layer path equation lacks a barotropic mode, the dispersion relation calculated for long wavelength meanders by Kontoyiannis and Watts (1990) is surprisingly close to the dispersion relation found in Pratt (1988).

The  $1\frac{1}{2}$  layer assumption is inherent in this thesis. Because the time scale is slow, soliton structures are possible in the model. By transforming the path equation to the MKdV equation, these breathers can be found using the inverse scattering transform. Using the inverse scattering method, an initial value problem for this nonlinear partial differential equation reduces to a linear integral equation where the time appears only implicitly. The full inverse scattering transform allows an exact solution to an initial value problem, which consists of a train of small amplitude dispersive waves and perhaps some solitary waves. The dispersive waves appear unable to form closed loops by themselves, based on the numerical solutions to the full path equation. However, they may play a role in ring-formation by interacting with breathers that are not quite able to pinch off by themselves (Figures 2.14, 3.20). By solving the linear eigenvalue problem (Equation 2.8), the shape, size and speed of the final breather can be found, based only on the shape of the initial condition.

The MKdV equation admits two kinds of solitary waves. A loop soliton corresponds to a single eigenvalue lying on the imaginary axis. Because of the integral constraints on the curvature distribution, a single loop soliton can not evolve from a non-intersecting zonal path. The breather corresponds to the pair of complex eigenvalues  $\alpha(\pm 1 + i\lambda)$ . We can see from Equation that the overall size and time scale of the breather is determined by  $\alpha$ , while the shape, or steepness is determined only by  $\lambda$ . As the breather gets steeper the speed at which it propagates lessens due to the retarding effect of vortex induction. When  $\lambda \geq 1$ , then at some time within

an oscillation period, a closed path is possible. When the path intersects itself we assume that other physical processes are dominant which will aid ring-formation. Thus we use  $\lambda \geq 1$  as a criterion for pinch off.

There are an infinite number of conservation integrals associated with equations that can be solved using the inverse scattering method. Because of these integral constraints, the time evolution must be very restricted. Two of these integral constraints were briefly discussed in chapter 3. If the initial meander is isolated along an infinite path then  $\frac{\partial}{\partial t} \int \kappa ds = 0$ , and  $\frac{\partial}{\partial t} \int \kappa^2 ds = 0$ . These integral constraints hinder ring formation in initial conditions with a single spike of curvature, such as the thin lobes of chapter 3 (which have a large center spike, and two long side flanks, with small curvature). Pratt(1988) found two other integral constraints on the shape of the path:  $\frac{\partial}{\partial t} \int Y dX = 0$ , and  $\frac{\partial}{\partial t} \int Y^2 dX = 0$ . For the initial steps of chapter 2,  $\int Y dX = \infty$ , while a breather has some finite value of  $\int Y dX$ . The step must shed an infinite number of dispersive waves in order to erode its jump in latitude. These dispersive waves are readily apparent in the numerical integrations of chapter 2.

It would be interesting to use the inverse scattering transform on meander shapes taken from satellite images of the Gulf Stream. In order to see if the method was able to predict ring-formation, it would be necessary to find a time sequence of images showing a meander at some initial time evolving into a closed ring. The initial meander should be isolated along the path, so that other meanders from downstream do not overtake, and change, the meander of interest. In practice, this would be difficult to try because of the problems in obtaining a sequence of cloud-free images with enough spatial coverage. A more practical test of this model is to calculate the spectrum associated with some meander, at two different times, and see if the discrete eigenvalues associated with the meander remain the same.

Instead of applying the method to meander shapes obtained from a jet like the Gulf Stream, the inverse scattering transform was used to predict ring-formation for simple shapes, in order to find criteria for ring-formation that may be applied to more realistic paths. Breathers were found for piecewise constant curvature meanders, and

smooth meanders with similar shapes. The scattering problem for the smooth shapes must be solved numerically, and there are numerical errors if the domain is not large enough to contain the meander. The piecewise constant curvature predictions agree well with the predictions for the more complicated smooth paths on the number, shape and size of the breathers. Because of the iterative formula (Equations 2.19, 2.20) the piecewise constant curvature scattering problem is easily solved, allowing a thorough examination of how variations in the shapes effect ring formation.

Steplike initial conditions were approximated as two piecewise constant curvature regions of the opposite sign. Chapter 2 discusses the evolution of these S-shaped meanders. Typically steps form one breather, with the size and shape determined by the size and angle of the initial step. Secondary breathers can form from a step if the path contains a long region of low curvature. These breathers are always single-valued and unable to form rings.

Because the symmetric,  $l_2 = 0$ , is so simple, we can analytically find that symmetric steps with no elongation form breathers when  $\Theta_0 \geq \frac{\pi}{\sqrt{2}}$ . As the step angle increases the breather formed is steeper, with a larger  $\lambda$ . When  $\Theta_0 \geq 4.1$  then a closed path is possible.

If the step is elongated so that the folds of the step are separated by a straight line segment, then the minimum angles for breather and ring-formation decrease to asymptotic values, which can be found analytically. We find that  $\Theta_0 \geq \frac{\pi}{2}$  for a breather to form. Thus, all single-valued steps must disperse away; the step must be curved back on itself before non-linear steepening and breather formation can occur. If  $\Theta_0 \geq 2.7$  then the step can form a ring.

Several smooth steps were also considered. The minimum angle for ring formation is 4.3, which is slightly greater than the critical angle for the piecewise constant curvature step ( $\Theta_0 = 4.1$ ). However, the folds in these smooth steps are closer together than the piecewise constant curvature steps, so this increase in the critical angles is consistent with the piecewise constant curvature results.

Chapter 2 also discusses piecewise constant curvature and smooth asymmetric steps. We find that as the step becomes more asymmetric, the size of the breather

decreases. Both the smooth and piecewise constant curvature steps double the size of  $\alpha$  (halving the size of the breather) as the small radius of curvature becomes one-fifth the size of the larger. The asymmetry does not seem to change the critical angles for breather and ring formation until the symmetry is quite small, i.e. where the small radius of curvature is one-tenth that of the larger. If the step is made more asymmetric, then the critical angles for breather and ring formation converge to  $\pi$ .

The numerical integrations of several smooth steps shows the presence of the expected breather and a dispersive wavetrain. As mentioned earlier, because of the integral constraints of Pratt (1988), an infinite amount of  $\int Y dX$  must be released in the form of dispersive waves as the latitudinal jump is eroded. These dispersive waves are not steep and do not ever become multi-valued. They may aid ring-formation in some initial conditions whose breathers are not quite ring-forming (Figure 2.14).

Chapter 3 discusses lobes, or  $\Omega$  shaped meanders that return to their initial latitude. Lobes were approximated as three regions of uniform curvature with alternating signs. The piecewise constant curvature results indicate that it is difficult for a single lobe to pinch off as a ring, unless the neck width is so narrow that other smaller scale processes are probably dominant. A single lobe has a sharp maximum of curvature in its peak. As the lobe evolves, this curvature is dispersed, and in the process the lobe is widened (Figure 3.9).

Pratt and Stern (1986) also found that single lobes resisted ring formation. Using contour dynamics, they found that tall, thin lobes formed rings more readily than shorter, squatter lobes, although the initial lobe must be very narrow. This result is consistent with the parameter plane (Figure 3.2) for the piecewise constant curvature lobes. The squat lobes, with short side flanks (small  $l_1$ ), are self-intersecting at angles smaller than the angle at which ring-formation is possible.

Two numerical solutions in Chapter 3 are compared with the breather expected by inverse scattering by examining time series of the maximum curvature and amplitude  $|Y|$ . Although the numerical oscillations in curvature and  $|Y|$  appear to be

modulated by some other process due to the interaction of the primary breather with the rest of the full solution, the dominant period and amplitude for the breather and the numerical solution are very similar. These comparisons show that the lobe does not undergo any type of instability as it evolves.

A single lobe can become ring forming if its neck width is made wider by the presence of a straight center section. In this case, the only lobes that are ring-forming are those for which the center section is the same size as the side flanks of the lobe. Then the two sides of the step act independently and two rings are formed, at the same critical angle as the single step. At smaller angles two breathers may form. One of the breathers will be large and steep, while the other is smaller and single-valued. The smaller breather is faster than the steep breather, so it quickly propagates away from the large breather (Figure 3.14).

Chapter 3 indicates that it is difficult for a ring to form from a single lobe, but there are some suggestions that modifications to the single lobe may enhance ring formation. If the initial lobe were asymmetric, then the path could pinch off when the evolving breather becomes symmetric. There is also the suggestion in section 3.5 that dispersive waves, or other, faster breathers, may overtake a slow, steep breather. It is possible that the interaction between two breathers may produce a closed path, although the interactions between the two breathers of Figures 3.16, and 3.17 do not force a pinch off.

# Appendix A

## The Inverse Scattering Transform

The inverse scattering transform is a non-linear extension of Fourier analysis which can be used to solve nonlinear partial differential equations which have soliton solutions. The method was first developed by Gardner, Greene, Kruskal and Miura (1968) for the Korteweg-deVries equation. It was later extended to the nonlinear Schrodinger equation by Zakharov and Shabat (1974) in a paper that opened the way for solutions to many other nonlinear evolution equations such as the modified Korteweg-deVries equation and sine-Gordon equation. Rather than directly solving the nonlinear equation, the inverse scattering method allows us to find the evolution of a given initial state by solving the problem in three linear steps : i) the scattering problem, ii) the time evolution of the scattering coefficients and iii) the determination of the final state by inverse scattering. This appendix outlines these three steps, as described by Ablowitz, Kaup, Newell and Segur (1974).

### A.1 The Scattering Problem

As in the main text, we consider the following eigenvalue problem

$$L \phi = \xi^2 \phi \tag{A.1}$$

where

$$L = \begin{bmatrix} -\frac{\partial}{\partial x} & 0 \\ 0 & \frac{\partial}{\partial x} \end{bmatrix} + \begin{bmatrix} 0 & u \\ u & 0 \end{bmatrix} \quad (\text{A.2})$$

with boundary conditions

$$\begin{bmatrix} \phi_1 \\ \phi_2 \end{bmatrix} \sim \begin{bmatrix} e^{-i\xi x} \\ 0 \end{bmatrix}, \quad x \rightarrow -\infty \quad (\text{A.3})$$

$$\begin{bmatrix} \phi_1 \\ \phi_2 \end{bmatrix} \sim \begin{bmatrix} Ae^{-i\xi x} \\ Be^{i\xi x} \end{bmatrix}, \quad x \rightarrow +\infty.$$

If we consider the wave,  $\psi = \phi_1 + i\phi_2$ , then Equation A.1 may be rewritten as the Schrodinger equation, Equation 2.8.

$$\psi_{xx} + [\xi^2 + (u^2(x,0) + iu_x(x,0))]\psi = 0 \quad (\text{A.4})$$

$$\begin{aligned} \psi(x) &\sim e^{-i\xi x}, & x &\rightarrow -\infty \\ \psi(x) &\sim iB(\xi)e^{i\xi x} + A(\xi)e^{-i\xi x}, & x &\rightarrow +\infty \end{aligned}$$

This describes the scattering of an initial wave with amplitude  $A(\xi)$  from  $+\infty$ , from the complex potential  $u^2 + iu_x$ , which is determined by the shape of the initial condition. A wave with unit amplitude is transmitted through the potential, and one of amplitude  $B(\xi)$  is reflected back to  $+\infty$ . Scattering problems like the Schrodinger equation are known to have two distinct types of solutions. The oscillatory states are the states which oscillate in the limit  $x \rightarrow \pm\infty$ . The spectrum of the eigenvalues  $\xi$  corresponding to these states lie along the real axis in a continuous distribution. A bound state occurs when there is a pole in the transmission coefficient, which is defined as the amplitude of the transmitted wave normalized by the amplitude of the incident wave, or  $\frac{1}{A(\xi)}$ . Thus, a bound state is a localized, or trapped, wave with complex wavenumber  $\xi$ . The bound states occur at a finite number of discrete wavenumbers which are determined by the potential. In the scattering step we map

the initial condition into a continuous spectrum, a discrete spectrum of eigenvalues and the amplitude coefficients for  $\phi$  as  $x \rightarrow \pm\infty$ . We will call this information:  $\{\xi_n, A(\xi, t), B(\xi, t)\}$ , the “scattering data”.

## A.2 Spectral Evolution

Given the “scattering data” in spectral space, we can determine how it evolves with time, if we know that  $u$  evolves according to the MKdV equation (Equation 2.6). We will assume that the eigenfunctions evolve linearly according to

$$\mathbf{A}\phi = \phi_t \tag{A.5}$$

where  $\mathbf{A}$  is some linear differential operator to be determined. Differentiating A.1 with respect to time, we find

$$L_t\phi + L\phi_t = \xi_t^2\phi + \xi^2\phi_t. \tag{A.6}$$

Then using equation A.5,

$$L_t\phi + L\mathbf{A}\phi = \xi_t^2\phi + \mathbf{A}(\xi^2\phi), \tag{A.7}$$

which can be rewritten as the operator equation,

$$L_t - \mathbf{A}L + L\mathbf{A} = \xi_t^2 \tag{A.8}$$

With the proper choice of  $\mathbf{A}$ ,  $\xi$  will be a constant. In addition, if  $\mathbf{A}$  is further restricted, then we will find an expression  $L_t - \mathbf{A}L + L\mathbf{A} = \mathbf{0}$  that is not an operator equation, but rather a differential equation that contains only  $u$  and its

derivatives with respect to  $x$  and  $t$ . For example, if we choose

$$\mathbf{A} = a \begin{bmatrix} -\frac{\partial}{\partial x} & 0 \\ 0 & \frac{\partial}{\partial x} \end{bmatrix} \quad (\text{A.9})$$

then  $\xi$  will be a constant, provided that

$$u_t - au_x = 0 \quad (\text{A.10})$$

so any potential of the form  $u(x + at)$  will have the same bound states.

We are interested in the evolution operator  $\mathbf{A}$  which gives us the MKdV equation when we evaluate  $L_t - \mathbf{A}L + LA = \mathbf{0}$ . The evolution is then governed by

$$\mathbf{A} = \begin{bmatrix} 2i\xi(u^2 - 2\xi^2) & 4\xi^2u + 2i\xi u_x - 2u^3 - u_{xx} \\ -4\xi^2u + 2i\xi u_x + 2u^3 + u_{xx} & -2i\xi(u^2 - 2\xi^2) \end{bmatrix} \quad (\text{A.11})$$

We now have an equation for the evolution of the eigenfunctions as  $u$  evolves according to the MKdV equation. The evolution of  $\phi$  itself is determined by  $u$  and its spatial derivatives; however, as  $x \rightarrow \pm\infty$ ,  $u$  and its derivatives vanish, so

$$\phi_t = \begin{bmatrix} -4i\xi^3 \\ 4i\xi^3 \end{bmatrix} \phi, \quad x \rightarrow \pm\infty. \quad (\text{A.12})$$

As  $x \rightarrow -\infty$ , we find the time dependence of  $\phi$  to be  $\phi = \phi_0 e^{-4i\xi^3 t}$ . As  $x$  approaches  $+\infty$ , then

$$\phi = \phi_0 e^{-4i\xi^3 t} \begin{bmatrix} A_0(\xi, t) e^{-i\xi x} \\ B_0(\xi, t) e^{i\xi x} \end{bmatrix} \quad (\text{A.13})$$

taking the derivative of this expression with respect to time, we find

$$\phi_t = \begin{bmatrix} -4i\xi^3 \\ -4i\xi^3 \end{bmatrix} \phi + \begin{bmatrix} A_t \\ B_t \end{bmatrix} = \begin{bmatrix} -4i\xi^3 \\ 4i\xi^3 \end{bmatrix} \phi \quad (\text{A.14})$$

or  $A_t = 0$  and  $B_t = 8i\xi^3$ . Thus, if  $u$  vanishes as  $x \rightarrow \pm\infty$ , then the time evolution

has become a simple linear problem in spectral space.

### A.3 Inverse Scattering

Now we know the scattering data at some later time, but we don't know the  $u(x, t)$  that caused this scattering data. The determination of  $u(x, t)$  from the scattering data is an inverse problem like those in quantum mechanics or seismology. Waves are reflected and transmitted by layers of rock, and knowledge of the incoming and outgoing waves give us information about the scatterer by an inverse scattering problem. In our case we need to invert the scattering problem A.1, to find the structure of  $u(x, t)$ .

This inverse problem is solved using Fourier transforms and the solution is given by the coupled pair of Marchenko equations

$$B_2(x, y) + \int_x^\infty dx' B_1(x, x') \Omega(x' + y) = 0 \quad (\text{A.15})$$

$$-B_1(x, y) + \Omega(x + y) + \int_x^\infty dx' B_2(x, x') \Omega(x' + y) = 0$$

where

$$\Omega(z) = \int_{-\infty}^\infty \frac{d\xi}{2\pi} e^{i\xi z} \left( \frac{B(\xi, t)}{A(\xi, t)} \right) + i \sum \frac{B(\xi_n, t)}{A_\xi(\xi_n, t)} e^{i\xi z} \quad (\text{A.16})$$

and the solution  $u(x, t)$  is given by

$$u(x) = 2B_1(x, x) \quad \text{or} \quad u^2(x) = 2\frac{\partial}{\partial x} B_2(x, x) \quad (\text{A.17})$$

Now the problem is reduced to solving these linear integral equations. If  $u(x, 0)$  has no continuous spectrum associated with it, then the integral equations may be solved exactly, with solutions given by Lamb(1980),

$$u = 2\frac{d}{dx} \tan^{-1} \left[ \frac{\text{Imdet}(M)}{\text{Redet}(M)} \right] \quad (\text{A.18})$$

where if  $N$  is the number of discrete eigenvalues, then  $M$  is an  $N \times N$  matrix with elements,

$$M_{i,j} = \delta_{i,j} - i \frac{B(\xi_j, t)}{A_\xi(\xi_j, 0)(\xi_i + \xi_j)} e^{-i(\xi_i + \xi_j)x} \quad (\text{A.19})$$

When  $N = 1$ , and  $\xi = i\eta$ , then this reduces to the expression for the single soliton (equation 2.5)

$$u(x, t) = \pm 2\eta \operatorname{sech}(2\eta x - 8\eta^3 t + \Delta) \quad (\text{A.20})$$

where the phase is

$$\Delta = \ln \left( \left| \frac{B(\xi, 0)}{A_\xi(\xi, 0)} \right| \frac{1}{2\eta} \right) \quad (\text{A.21})$$

If  $N = 2$ , and the eigenvalues occur in the pair  $\alpha(\pm 1 + i\lambda)$ , then the solution is the breather

$$u = -2 \frac{\partial}{\partial x} \tan^{-1} [\lambda \sin(2\alpha(x + c_p t) - \theta_p) \operatorname{sech}(2\lambda\alpha(x + c_e t) + \theta_e)] \quad (\text{A.22})$$

where the phases  $\theta_p$  and  $\theta_e$  are

$$e^{i\theta_p} = \frac{B(\xi)/A_\xi(\xi)}{|B(\xi)/A_\xi(\xi)|} \quad e^\psi = \frac{1}{\alpha\lambda} |B(\xi)/A_\xi| (1 + \lambda^2)^{-\frac{1}{2}} \quad (\text{A.23})$$

These are the individual solitary wave solutions. The full solution may be found from the Marchenko integral equations (A.15) in principle, but in practice, these equations would have to be solved numerically. Segur (1973) shows that the general solution to an initial value problem can be approximated by the solitons as  $t \rightarrow \infty$  because the oscillatory solution decays with time. While this approximation may not be strictly valid at finite times, the numerical solutions suggest that only the solitary waves are steep enough to form rings.

## A.4 Summary

The inverse scattering transform may be used to find the evolution of isolated disturbances, governed by certain nonlinear partial differential equations. The method

allows the solution to be found by solving three linear problems: i) a linear eigenvalue problem, ii) a linear evolution equation, and iii) a linear integral equation for the inversion.

The key to this approach is that the eigenvalues  $\xi_n$  remain constant in time, if the “potential”  $u(x, t)$  evolves according to one of these evolution equations, such as the MKdV equation. The number and shape of the solitons that will emerge from the initial condition is determined by the number and location of the discrete eigenvalues. These solitons are the asymptotic solution to the initial value problem. The time-dependence in spectral space is linear, and not dependent on the shape of  $u(x)$ . Thus the final solution, determined by a linear integral equation, only has an implicit time dependence.



# Bibliography

M. J. Ablowitz, D. J. Kaup, A. C. Newall, and H. Segur. The inverse scattering transform - Fourier analysis for nonlinear problems. *Stud. Appl. Math.*, 53:249–315, 1974.

B. Cushman-Roisin, L.J. Pratt, and E.A. Ralph. A general theory for equivalent barotropic thin jets. in prep. 1991.

R.P. Feynmann. *The Feynmann Lectures on Physics*. Addison-Wesley, London, 1965.

G. R. Flierl and A. R. Robinson. On the time dependent meandering of a thin jet. *J. Phys. Oceanogr.*, 14:412–443, 1984.

F.C. Fuglister and L.V. Worthington. Some results of a multiple ship survey of the Gulf Stream. *Tellus*, 3:1–14, 1951.

C.S. Gardner, J.M. Greene, M.D. Kruskal, and R.M. Miura. Method for solving the Korteweg-deVries equation. *Phys. Rev. Lett.*, 19:1095–1097, 1968.

D. Halkin and T. Rossby. The Structure and Transport of the Gulf Stream at 73° W. *J. Phys. Oceanogr.*, 15:1439–1452, 1985.

M. Hall and N. Fofonoff. Downstream Deviation of the Gulf Stream from 68° W to 55° W. *J. Phys. Oceanogr.*, submitted 1991.

D.V. Hansen. Gulf Stream meanders between Cape Hatteras and the Grand Banks. *Deep-Sea Research*, 17:495–511, 1970.

- C. O'D. Iselin. A study of the circulation of the western North Atlantic. *Papers in Physical Oceanography and Meteorology*, 4:4–101, 1936.
- H. Kontoyiannis and D.R. Watts. Observations of Gulf Stream Path Variability between  $74^{\circ} W$  and  $70^{\circ} W$ : Meanders, Standing Mode, and Upstream Propagation. *The Synoptician*, 1:1,3, 1990.
- G. L. Lamb. *Elements of Soliton Theory*. Wiley, New York, 1980.
- S.P. Meacham. Meander evolution on quasigeostrophic jets. 1990, to be submitted.
- L. J. Pratt and M.E. Stern. Dynamics of potential vorticity fronts and eddy detachment. *J. Phys. Oceanogr.*, 16:1101–1120, 1986.
- L.J. Pratt. Meandering and eddy detachment according to a simple (looking) path equation. *J. Phys. Oceanogr.*, 18:1627–1640, 1988.
- W.H. Press. *Numerical Recipes*. Cambridge University Press, New York, 1986.
- L.G. Redekopp. On the theory of solitary Rossby waves. *J. Fluid Mech.*, 82:725–745, 1977.
- L.G. Redekopp and P.D. Weidman. Solitary Rossby Waves in Zonal Shear Flows and Their Interactions. *J. Atmos. Sci.*, 35:790–804, 1978.
- A. R. Robinson, J.R. Lutyen, and G.R. Flierl. On the theory of thin rotating jets: A quasi-geostrophic time dependent model. *Geophys. Fluid Dyn.*, 6:211–244, 1975.
- A. R. Robinson and P.P. Niiler. The theory of free inertial currents, I : Path and structure. *Tellus*, 19:269–291, 1967.
- A.C. Scott. *Active and nonlinear wave propagation in electronics*. Wiley, New York, 1970.

H. Segur. The Korteweg-deVries equation and water waves. Solutions of the equation. Part 1. *J. Fluid Mech.*, 59:721–736, 1973.

S. Torven. Modified Korteweg-de Vries equation for propagating double layers in plasmas. *Phys. Rev. Lett.*, 47:1053–1056, 1981.

K.L. Tracey and D.R. Watts. On the Gulf Stream meander characteristics near Cape Hatteras. *J. Geophys. Res.*, 91:7587–7602, 1986.

J. Vasques and D.R. Watts. Observations on the propagation, growth, and predictability of Gulf Stream meanders. *J. Geophys. Res.*, 90:7143–7151, 1985.

B. A. Warren. Topographic influences on the path of the Gulf Stream. *Tellus*, 15:167–183, 1963.

V.E. Zakharov and A.B. Shabat. A scheme for integrating the nonlinear equations of mathematical physics by the method of the inverse scattering problem, I. *Funct. Anal. Appl.*, 8:226–235, 1974.